RESONANT-INFRARED LASER ABLATION OF POLYMERS: MECHANISMS AND APPLICATIONS

By

Stephen L. Johnson

Dissertation

Submitted to the Faculty of the

Graduate School of Vanderbilt University

in partial fulfillment of the requirements

for the degree of

DOCTOR OF PHILOSOPHY

in

Physics

December, 2008

Nashville, Tennessee

Approved:

Professor Richard F. Haglund, Jr.

Professor M. Shane Hutson

Professor Eva Harth

Professor Kenneth E. Schriver

Professor Ronald D. Schrimpf

To my wife, Erin,
and my grandfather, Walter.

ACKNOWLEDGMENTS

This dissertation was made possible through the direct and indirect help of many people over the course of my graduate studies. To all of the people mentioned in the following, as well as to many not mentioned, I offer my most sincere gratitude and appreciation for contributing to what has been four of my most accomplished and productive years.

First and foremost, I thank my advisor, Richard Haglund, for his guidance and mentorship. The trust and confidence that he placed in me always inspired a good work ethic and a strong desire to achieve. I believe that my growth as a a scientist is due much in part to him, and I hope that his level of professionalism will continue to influence me for years to come.

Many people have been instrumental in helping either physically in the lab, or through frequent discussions. Ken Schriver helped to recruit me into the Haglund research group and to get me started in my work. I am very appreciative of this, as well the fact that he has had seemingly endless patience for me coming into his office unannounced and asking questions. I am also grateful for the help of Professor Danny Bubb at Rutgers Camden in all of the work we have done during our collaborations together. I am indebted to several members of the FEL staff - Rick Grant and Dick Ardrey for the countless hours they have spent operating the laser for me, and John Kozub who seemed to know the answer to practically any question that I could ask. I thank Nicole Dygert for being, in some sense, a partner in this research effort and for always entertaining my questions about chemistry, however ignorant that may have been. I owe much of my practical laboratory skills to René Lopez, Kevin Tetz, and Jonathon Jarvis, who were always more than willing to take time out of their day to help set up an experiment or teach me how to write MATLAB or LabVIEW programs. Other people who have helped in my research and to whom I am very thankful are Michael Papantonakis, Eugene Donev, Andrej Halabica, Hee Park, Kannatessen Appavoo (Krishen), Borislav Ivanov, and Ricardo Torres. This is by no means a complete list of contributors, but I have tried to acknowledge those who were most instrumental in helping with my dissertation research, many of whom I also consider to be dear friends.

I also thank my Ph.D. committee for their discussions and advice, and for the role they have had in shaping this dissertation. Their suggestions were especially constructive after my qualifying examination when they helped me to focus on the specific research topic which has become the central theme of my thesis.

Outside of research, there have been many people whose love and friendship has made my passage through graduate school a more memorable experience. I am forever grateful for the support of my wife, Erin, who was able to balance a busy life in medical school with first a fiancé, and now husband in graduate school. I am also thankful for the presence of my family - most importantly that of my parents and grandparents who instilled in me the values of hard work. And to the many friends who made life in the lab and the office a bit more enjoyable (and even fun at times) - Chris Goodin, Davon Ferrara, Jed Ziegler, Charlie Adams, Hugo Valle, and Jared Crochet, just to

name a few, I say thanks.

It is very important to acknowledge the funding support I have received, because without it this research would not have been possible. Early on, I was supported through a research grant funded by the Naval Research Lab. The primary funding for the remainder of my graduate studies was generously provided by AppliFlex LLC, and I specifically thank Dr. Hee Park for this support. I am also grateful to the Graduate School at Vanderbilt for awarding me a dissertation enhancement grant in my final year of graduate study, and for providing travel funding to attend several conferences.

All of these people and entities were instrumental in one way or another in achieving the goal that I set out to accomplish four years ago, and I am extremely thankful to have such a core group of colleagues, family, and friends.

TABLE OF CONTENTS

LIST OF TABLES

LIST OF FIGURES

CHAPTER I

INTRODUCTION AND BACKGROUND

1.1 Introduction and Motivation

The construction of the ruby laser in 1960 [1] opened many new doors to the field of materials processing. Laser ablation, the process of material removal using an intense laser beam, was one of the many applications that researchers soon found in the 1960s [2]. In 1965, Smith and Turner were the first to use laser ablation for vacuum deposition of thin-films [3]. Since then, and especially since the first report of pused-laser deposition (PLD) of high T_c superconductors in the late 1980s [4], laser deposition has become a preferred method of thin-film growth in solid-state physics and materials science.

Laser ablation and deposition of polymers in particular have been studied now for several decades. From a fundamental science point of view, polymer ablation is a rich and complex phenomenon that presents many challenges, both theoretical and experimental. From an applied science point of view, PLD of polymers offers a novel way to grow polymer thin films that have become increasingly important in the electronics, pharmaceutical, and microsensing industries, just to name a few [5]. However, the ability to grow intact polymer thin-films by conventional PLD techniques is currently limited, and new variations of PLD are needed in order to make it a viable option for polymer film growth.

1.2 Specific Aims

The aim of this dissertation is to present research related to a new type of polymer ablation, namely, resonant-infrared (RIR) ablation using high-repitition-rate picosecond laser pulses. The work contained in the following chapters can be divided into two distinct, but related, categories - mechanisms, and applications of RIR ablation. The mechanistic chapters (II and III) are presented first and study two model polymer systems to gain insight into the physics of RIR ablation. For the first time, a consistent explanation of the RIR ablation process from beginning to end is presented. The proposed ablation mechanism combines two separate components: one thermal, and one hydrodynamic in nature. We have identified spinodal decomposition as the initial thermal mechanism for RIR laser ablation, which begins after the density of absorbed laser energy is sufficient to drive the polymer surface region into thermodynamic instability. Following spinodal decomposition, recoil-induced ejection of liquid dominates as the operative ablative mechanism as liquid material is expelled *via* the recoil force of the expanding vapor plume. As will be shown through static and time-resolved measurements and further supported through thermal calculations, this set of proposed ablation mechanisms accounts for the data and observations that are presented in chapters II and III.

The applications chapters (IV and V) make use of the proposed RIR ablation mechanisms to explain properties of laser-deposited thin films, while simultaneously demonstrating new technologies that have been developed regarding polymer film deposition. The applications involve novel techniques that solve various problems

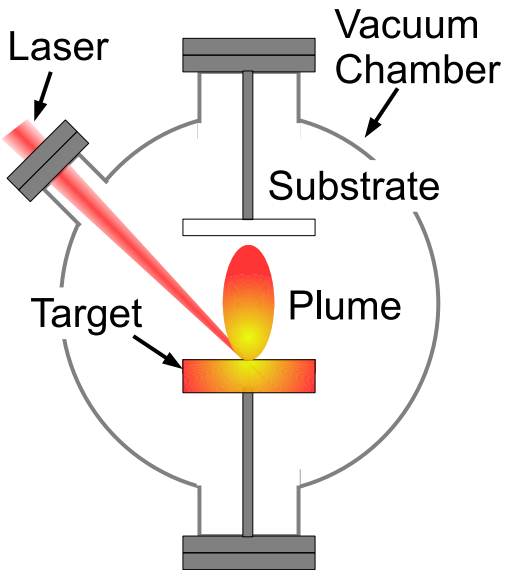

Figure 1.1: Schematic illustration of pulsed-laser deposition.

associated with polymer film deposition. For example, using RIR laser light, films of electronic and optoelectronic polymers were grown, and polymer light-emitting devices (PLEDs) were successfully fabricated in a clean vacuum environment. These applications are relevant to the greater organic electronics community, among others, as they offer novel routes to polymer thin-film growth that could compliment existing techniques.

1.3 Laser ablation and deposition of polymers

Pulsed Laser Deposition (PLD) is the process by which a laser (typically ultraviolet) ablates a target and the generated plume of material is collected on a nearby substrate, as shown schematically in figure 1.1. Some of the advantages to this process are that it is typically done in high to ultrahigh vacuum and is therefore clean, deposition rates can be high (on the order of nm/sec), multilayer depositions can be

done by use of a multi-target carousel, and films can be patterned through shadow masks. PLD is best known for its success in depositing films of metal and ceramic oxides and high-temperature superconductors, but has recently become popular for the deposition of polymer films [6].

1.3.1 UV laser ablation

The first work on polymer ablation was done in 1982 by Srinivasan using a UV laser [7], and independently by Kawamura [8] in the same year. Since then, researchers have expanded work in this field to include the ablation of many different polymers by different UV laser wavelengths (although most commonly 248 and 193 nm). An inherent problem in UV-PLD of polymers is that the resulting film often contains many photofragmented products that result from the high energy of the laser photon [9, 5]. Typical bond energies in organic compounds are $\sim$ 3.5 eV, whereas the energy a 248 nm KrF excimer laser photon, for example, is 5 eV. It is obvious that these photons have sufficient energy to break chemical bonds between atoms and cause photofragmentation, as outlined in the first paper concerning ablative photochemical decomposition [10]. The mechanism of photon absorption in this energy regime is electronic, *i.e.* the promotion of ground state electrons to their excited state, and these excited electrons may take pathways back to the ground state that involve ionization or decomposition. An analysis of the ablation products produced by ultraviolet lasers typically reveal monomer or even smaller molecular or gaseous species [11].

1.3.2 MAPLE

In 1999, a group at the Naval Research Lab (NRL) developed a technique dubbed MAPLE - Matrix Assisted Pulsed Laser Evaporation - which was designed to eject polymers into a gaseous phase using a laser, but in a "gentler" way [12]. The protocol calls for the target polymer to be dissolved in a volatile matrix at a concentration between 1-5% by weight, frozen in liquid nitrogen, and then placed inside of the deposition chamber. The difference in this technique is that the solvent matrix, which comprises 95-99% of the total target, has the role of absorbing most of the laser energy and shielding the polymer from direct electronic excitation. The absorption of the laser pulse causes a rapid heating and evaporation of the solvent, and the imbedded polymer comes out with the evaporated matrix molecules. The volatile solvent is then ideally pumped away by the vacuum system while the heavier polymer continues on a linear trajectory until it reaches the collection substrate. This process, in theory, reduces the amount of energy the polymer absorbs and thus reduces the amount of photochemical and fragmented species that are produced.

The technique is, in general, more successful than PLD of bulk polymer targets but is highly dependent on the matrix used. For example, when the UV light is energetic enough to disassociate matrix molecules such as chloroform ($CHCl_3$), reactions such as

$$CHCl_3 \xrightarrow{h\nu} CHCl_2 + Cl$$

followed by

$$CHCl_2 \xrightarrow{h\nu} CCl + HCl$$

can occur [13]. Due to the high reactivity of Cl and HCl, they may become attached to polymers in the plume and create new species. So while the UV-MAPLE technique in theory is a gentle ablation process, it often generates unwanted compounds in the film, the origin of which may ultimately be traced back to the energetics of the UV laser photons. Another problem that plagues UV-MAPLE is the poor surface quality of deposited films. Scanning-electron micrograph images of films depict "deflated-ballon" structures apparently caused by solvent wicking effects, indicating that the solvent is deposted along with the polymer [14].

1.3.3 RIR laser ablation

The polymer photochemistry that is likely to occur when using UV as an ablation source is generally undesirable. Moreover, the competition of potential photochemical and photothermal phenomena make it difficult to generalize and understand the ablation mechanism. In 2001, the first experiments involving RIR ablation and deposition of polymers were done by Bubb using a mid-IR free-electron laser (FEL) [15]. The motivation to use the FEL was that the mid-IR single-photon energies ($\sim$ 0.25 eV) were much less than covalent bond energies, making the probability for photochemistry practically negligible (for example, 12 photons at 0.25 eV must be simultaneously absorbed to directly break a 3 eV covalent bond). Moreover, the topic of resonant vibrational excitation of polymers by such an intense light source had never been studied before and therefore offered a new area of fundamental research.

One important difference between IR and UV excitation is the way in which the photons couple their energy into a material. UV photons are absorbed by exciting

delocalized electronic transitions in the valence bands of a material. IR photons, on the other hand, deposit their energy into anharmonic, localized vibrational modes of the material which then couple to the lattice on the time scale of hundreds of fs to ps. Given that the FEL laser pulses used in these ablation experiments are 4 μs long (the FEL is described in section 1.4), the energy deposited into the localized vibrational modes is thermalized immediately and the laser effectively serves to heat the material. Thus, from general considerations one would expect that RIR ablation would be a photothermal rather than a photochemical process, which is discussed in the following section.

The key to RIR ablation is that the excitation is *resonant* with a vibrational mode of the polymer target. Typical optical penetration depths of resonant IR light are much larger than penetration depths at UV wavelengths (tens vs. fractions of μm, respectively), and the corresponding volumetric energy density is much less. It turns out that for optical penetration depths much larger than tens of μm, as is the case with non-resonant IR wavelengths, it is difficult to achieve a volumetric energy density that is high enough to induce ablation. The criterion of resonant excitation, then, is necessary in order to achieve successful material ablation.

Obviously, all polymers do not have the same absorption structure in the infrared, so one fixed-wavelength laser can not be resonant with every polymer. In fact, every polymer has its own unique infrared absorption spectrum that serves as its "molecular fingerprint". The ability to access many mid-IR wavelengths in this molecular fingerprint region is therefore necessary in order to resonantly excite different polymers. Mid-IR FELs offer continuous wavelength tunability from 2-10 μm, making them

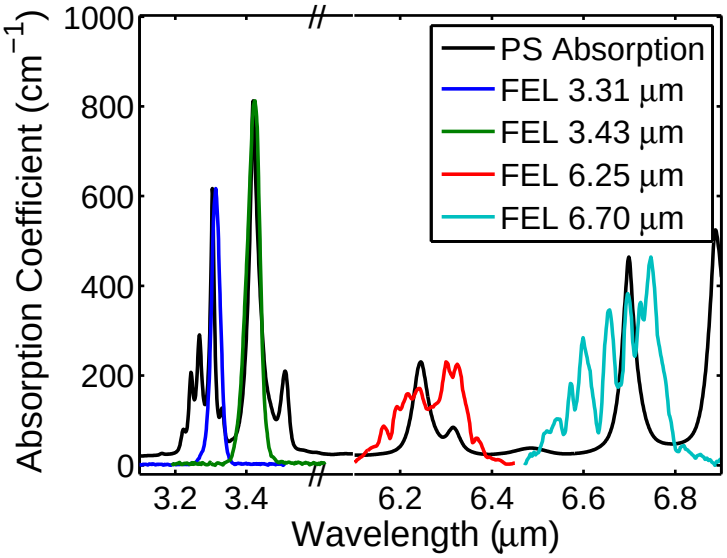

Figure 1.2: Illustration of resonant IR excitation of polystyrene (PS) at different FEL wavelengths.

ideal lasers for RIR ablation research. With such a versatile laser one can examine an infrared absorption spectrum of a polymer and then choose a laser wavelength that overlaps with a resonant absorption. Figure 1.2 demonstrates this by showing an infrared spectrum of polystyrene (PS) along with different laser spectra which lead to resonant excitation.

MAPLE using resonant IR laser light (RIR-MAPLE) offers the same potential benefits of UV-MAPLE, but with a smaller chance of photochemistry occurring in the matrix. The process of RIR-MAPLE is the same as UV-MAPLE, except the IR laser light is tuned to a vibrational resonance of the matrix. This is especially beneficial when the matrix and the polymer have non-overlapping vibrational bands so that the matrix can be selectively excited independently of the polymer. This way, one can ensure that all of the energy is deposited into the solvent, thereby reducing the possibility of damage to the polymer. Chapters IV and V deal with the deposition

of electronically active polymers using the RIR-MAPLE technique.

1.3.4 Ablation mechanisms

The mechanisms of polymer ablation have been debated since the first experiments done by Srinivasan. The two most common classes of polymer ablation mechanisms discussed in the literature are either photochemical or photothermal in nature [16]. Photochemical models suggest that ablation proceeds *via* the direct breaking of chemical bonds following photoexcitation [10]. This is most likely to occur in UV ablation, since the absorbed photon energies typically exceed the energy required to break chemical bonds. A photothermal model essentially describes ablation as a localized pyrolisis event following the thermalization of photoexcited electrons (which occurs on a fs-ps time scale). The work presented in this dissertation reveals that a photothermal mechanism (namely, spinodal decomposition) is responsible for the early stages of RIR polymer ablation. Photochemical mechanisms are not discussed in depth here and more attention is given to mechanisms which are photothermal in nature. Specifically, we discuss here the concepts of normal boiling and phase explosion in the context of polymer ablation. The discussion generally follows sections in reference [17] dealing with mechanisms of tissue ablation.

Thermal processes inherently involve phase transitions, so it is instructive to examine a pressure-temperature phase diagram such as that shown in figure 1.3. In laser ablation, the starting point is a solid target which during/after laser irradiation is vaporized to some extent. Before vaporizing, obviously, the target first melts under the influence of the laser and liquefies. Then, depending on the laser intensity and the

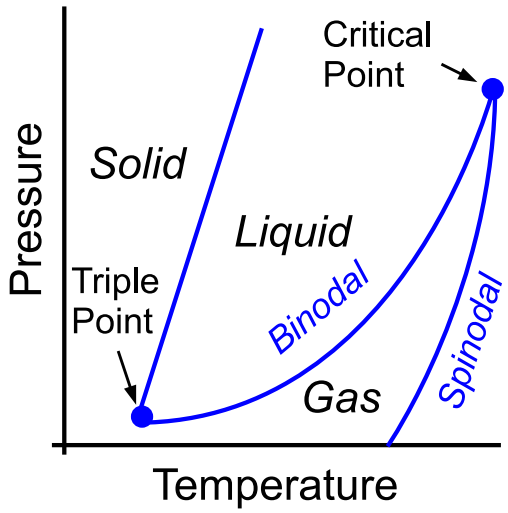

Figure 1.3: A generic pressure-temperature phase diagram demonstrating the location of the binodal and spinodal in p-T space.

rate of heating, one of two things may happen: the liquid could vaporize by normal boiling, or it could explode into a mixture of gas and liquid droplets through spinodal decomposition.

1.3.4.1 Normal boiling

Normal boiling occurs at any point along the binodal in figure 1.3, the set of points at which liquid and vapor are in equilibrium. Normal boiling relies on the growth of predissolved cavities of gas located heterogeneously within the liquid that catalyze the vaporization process. For laser heating rates which are sub-μs, heterogeneous bubble nuclei cannot grow and propagate to the surface rapidly enough for the liquid to remain in equilibrium with the vapor, leaving spinodal decomposition as the only possible thermal mechanism for ablation [18]. Moreover, for polymers, normal boiling is not even a valid physical concept. Most polymers do not have a defined boiling

point since they decompose at temperatures far below those that would be required to liberate entire polymer chains into the gas phase. In fact, the upper mass limit on polymers that can be evaporated as intact chains is found to be $\sim$ 1000 amu, both theoretically and experimentally [19] (see appendix A for fundamentals of polymer systems). Thus, for a polymer target, the only way for material to evolve along the binodal is if slow heating causes chain framentation and the generated species are small enough to liberate themselves into the gas phase. In this sense, "Gas" as it is labeled in figure 1.3 is somewhat misleading because the gas formed may or may not have the same chemical structure as the solid and liquid material. Therefore, normal boiling does not really exist for polymer systems and some other thermal mechanism must account for how material is removed during ablation.

1.3.4.2 Spinodal decomposition

If a liquid is heated rapidly enough such that rate of energy deposition exceeds the rate of energy released by homogeneous bubble growth, it may pass beyond the binodal in figure 1.3 into a metastable state between the binodal and the spinodal. The liquid may remain stable until the spinodal temperature is reached, at which point it instantaneously relaxes by exploding into a mixture of gas and liquid droplets. This process is commonly called "spinodal decomposition" or "phase explosion". The spinodal represents the set of points in p-T space at which the liquid is thermodynamically unstable and beyond which one distinct physical phase can not be maintained. Since normal boiling of a polymer melt is not a physical concept, spinodal decomposition is the only thermal process which can put a polymer melt into a gaseous phase. In

the context of polymers, however, "gas" is simply a vaporized form of decomposition products. High intensity, high repetition-rate laser pulses such as those described in section 1.4 drive an isobaric transition in a polymer from STP conditions to the spinodal on the phase diagram. Previous work with polystyrene (PS) and poly(ethylene glycol) (PEG), the polymers used in chapters II and III, found that the effective spinodal decomposition temperature is on the order of 1100 °C at atmospheric pressure [20, 21]. Laser-induced temperature rise calculations presented in these chapters reveal that the temperatures reached at the ablation threshold are indeed of this magnitude, thus making phase explosion the likely operative mechanism of ablation.

1.3.4.3 Recoil-induced ejection

If a laser-superheated liquid undergoes spinodal decomposition, the pressure immediately beneath the phase-exploded region will increase dramatically due to the recoil momentum of the expanding vapor plume. This pressure can impart enough force to the remaining liquid to expel it from the target. Essentially, the recoil momentum generated by the expanding vapor plume acts like a piston and compresses the laser-melted region of the target, causing the ejection of a hollow cylinder of liquid material that erupts from the target surface. This method of material removal is commonly called recoil-induced ejection and is known to occur in IR ablation of water and tissue [22, 23]. The concept is illustrated schematically in figure 1.4. Although it relies on a photothermal process to occur, recoil-induced ejection is not a type of photothermal mechanism, *per se*. Once the recoil force is provided by the expanding vapor plume, then the act of liquid removal is due to hydrodynamic effects, only.

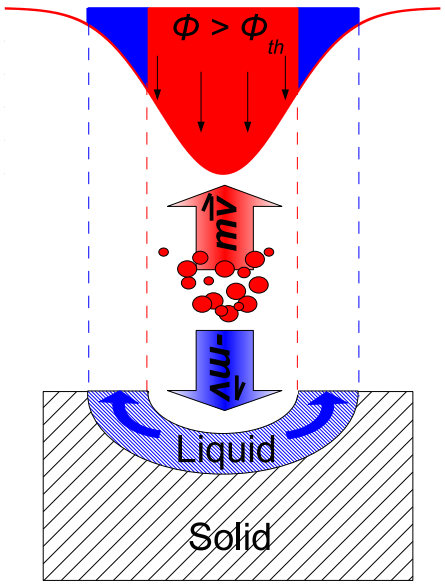

Figure 1.4: Schematic illustration of recoil-induced ejection (adapted from reference [24]).

We therefore consider it to be a hydrodynamic mechanism of ablation, rather than a thermal one, and refer to it as such throughout the dissertation.

1.3.5 Heuristic models

Several heuristic models have been developed to describe various experimental observations related to laser ablation such as laser-etching rate and plume shielding. While these models do not prescribe any specific mechanism to an ablation process, they do give insight as to what likely happens during the event.

1.3.5.1 Blow-off model

The blow-off model was originally developed to model etch depth vs. fluence data pertaining to excimer ablation of polymers [17]. Recall that excimer laser pulses

are typically tens of ns long, and thus one assumption of the blow-off model is that material removal does not begin until sometime after the end of the laser pulse. The essence of the model is that ablation requires some threshold volumetric energy density, E_{th}, to occur, and that the ablated depth per pulse is equal to the depth that has an energy density of at least E_{th}. Assuming Beer's law is valid for the absorption of laser light into the target, then the intensity distribution is

$$\Phi(z) = \Phi_0 e^{-\alpha z} \tag{1.1}$$

where $\Phi(z)$ is the laser fluence (energy per area) in the target as a function of z, Φ_0 is the full pulse laser fluence, and α is the optical absorption coefficient of the polymer. Solving for z as a function of Φ gives

$$z = \frac{1}{\alpha} ln \left(\frac{\Phi_0}{\Phi} \right) \tag{1.2}$$

Once a depth, $z = \delta$, reaches the ablation threshold fluence, Φ_{th}, then the all material down to that depth is removed:

$$\delta_{blow-off} = \frac{1}{\alpha} ln \left(\frac{\Phi_0}{\Phi_{th}} \right) \tag{1.3}$$

If a set of etch depth vs. fluence data exhibit a logarithmic trend, then it may be inferred that the above assumptions about the ablation process are true; namely that linear absorption holds, ablation does not begin until after the laser pulse, and that the ablation depth is proportional to some threshold energy density deposited by the

laser.

1.3.5.2 Steady state model

A steady state model is in essence the opposite of the blow-off model. While the blow-off model assumes that no material is removed until the laser pulse terminates, the steady state model assumes continuous removal of material throughout the duration of the laser pulse. This assumption is generally valid for laser pulses in the μs regime [17]. The energy leaving the system through the continuous ablation is balanced by the energy deposited by the laser so that the system is in an equilibrium (hence the term, steady state). If material removal begins immediately after laser irradiation with a fluence $\Phi_0 > \Phi_{th}$, then we expect a linear relationship between the etch depth, δ, and the fluence:

$$\delta_{steady-state} = \frac{\Phi_0 - \Phi_{th}}{\rho h_a} \tag{1.4}$$

where ρ is the material density, and h_a is the enthalpy (latent heat) of ablation.

1.3.5.3 Plume shielding model

Izatt developed a heuristic model which allows for an ablation plume to shield the incoming laser pulse during a steady state ablation process [25, 26]. Assuming ablation is a thermally activated process, the threshold fluence, Φ_{th}, is related to the ablation enthalpy by

$$\Phi_{th} = \frac{h_a}{\alpha} \tag{1.5}$$

which simply states that it requires a fluence of Φ_{th} to ablate one optical penetration depth. The amount of time, t_0, it takes for ablation to begin is related to the laser irradiance (fluence per time) at the target surface and the threshold fluence by

$$t_0 = \frac{\Phi_{th}}{I_0} \tag{1.6}$$

If ablation begins at time t_0 and the ablation front moves with a constant velocity, v, then we may write

$$v = \frac{dz}{dt} = \frac{I(z)}{h_a} \tag{1.7}$$

To allow for plume absorption, we assume that as the ablation front moves into the target, the plume attenuates the laser with an absorption coefficient α_p, so that the laser irradiance is modified by

$$I(z) = I_0 e^{-\alpha_p z} \tag{1.8}$$

To solve for the final crater depth, δ, we must rearrange equation 1.7 and integrate over the entire laser pulse and ablation depth:

$$\int_{t_0}^{t} \frac{dt'}{h_a} = \int_0^{\delta} \frac{dz}{I(z)} \tag{1.9}$$

Inserting equation 1.8 and integrating, we have

$$\frac{t - t_0}{h_a} = \frac{e^{\alpha_p \delta} - 1}{\alpha_p I_0} \tag{1.10}$$

After using equations 1.5 and 1.6 and solving for δ, we obtain

$$\delta = \frac{1}{\alpha_p} ln \left[\frac{\alpha_p}{\alpha} \left(\frac{\Phi_0}{\Phi_{th}} - 1 \right) + 1 \right] \tag{1.11}$$

It is convenient to define the parameter $\gamma = \alpha_p/\alpha$, which we will call the plume shielding coefficient since it describes the strength of plume absorption relative to the target absorption. Inserting this into equation 1.11 yields

$$\delta = \frac{1}{\alpha\gamma} ln \left[\gamma \left(\frac{\Phi_0}{\Phi_{th}} - 1 \right) + 1 \right] \tag{1.12}$$

Figure 1.5 compares a blow off model, steady state model, and plume shielding model for a given absorption coefficient. Several values of γ are shown for the plume shielding

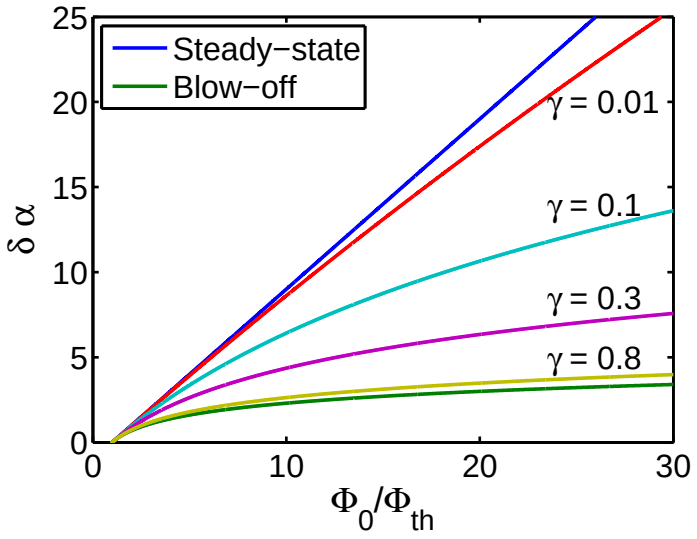

Figure 1.5: Calculated etch depths as a function of fluence for the plume shielding ablation model. The plot demonstrates how the factor γ in the plume shielding model determines the extent to which the data more nearly resembles the steady state or the blow-off model.

case. Notice that as $\gamma \rightarrow 0$, meaning that the plume does not shield the laser pulse, the plume shielding model converges with the steady state model, as it should. When there is heavy plume shielding, $\gamma \rightarrow 1$ and the plume shielding model converges toward the blow-off model. In this sense, the plume shielding model can also be thought of as an intermediate between a blow-off and a steady state model. In chapters II and III, it is shown that etch depth data of RIR polymer ablation is well fit by the plume shielding model with a γ factor of ~ 0.3, which indicates moderate plume shielding during a continuous ablation process.

1.3.6 Relevant time scales

In discussing laser ablation, there are several important time scales to consider. We consider here two of the most common ones in the context of RIR polymer ablation.

1.3.6.1 Thermal confinement time

In the absence of photoionization and phase changes, laser energy deposited into a polymer target is transformed into heat. RIR excitation of localized molecular vibrations couples to the phonon bath within hundreds of fs to ps and is thereby thermalized. The time it takes for this thermal energy to diffuse out of the focal volume is known as the thermal confinement time. Assuming that the laser spot size is much larger than the $1/\alpha$ absorption depth, we may effectively consider any thermal diffusion to take place in one dimension and thus write the thermal confinement time

as

$$\tau_{th} = \frac{c_p \rho}{\alpha^2 \kappa} \tag{1.13}$$

where c_p is the specific heat, ρ is the material density, α is the absorption coefficient, and κ is the thermal conductivity. For resonant IR excitation of a polymer, typical parameters would be $c_p \sim 1$ J/g/°K, $\rho \sim 1$ g/cm^2, $\kappa \sim 0.1$ W/m/°K, and $\alpha \sim 400$ cm^{-1}. Together, these parameters yield a thermal confinement time of ~ 6 ms, which is approximately 1000 times longer than the FEL pulse (discussed in section 1.4). Since this is the case, we may consider the FEL excitation pulse as being thermally confined, meaning that heat does not bleed out of the focal volume during the laser pulse. We will invoke this fact several times in the following chapters during discussions of ablation mechanisms.

1.3.6.2 Stress confinement time

When a solid is heated (by a laser or otherwise), it expands. If it is heated locally, then the localized expansion creates a mechanical disturbance that propagates at the speed of sound throughout the solid . If the locally applied heat is deposited faster than the time required for sound waves to travel from the area, then stress builds and the excitation is "stress confined". For laser excitation, the stress confinement time is defined as

$$\tau_s = \frac{1}{\alpha C_s} \tag{1.14}$$

where C_s is the speed of sound in the solid and α is the optical absorption coefficient (we have again used the one-dimensional approximation). The stress confinement

time represents the time it takes for a mechanical wave to propagate outside of the laser focal volume. It is important in laser ablation because pulses shorter than the stress confinement time can create large stress waves capable of mechanically spallating or fracturing a target [27]. This process is generally referred to as photomechanical ablation. A typical speed of sound for a polymer like polystyrene is 2300 m/s, so the stress confinement time is approximately 10 ns for RIR ablation. Since this is orders of magnitude shorter than the laser pulses generated by the FEL, there is no buildup of any mechanical wave and photomechanical processes are therefore not likely to influence the ablation.

1.4 The W.M. Keck free-electron laser

The W.M. Keck free-electron laser was the primary research tool used in all of the experiments described in this dissertation. Without this unique laser, the work presented in the following chapters would not have been possible. This section outlines the principles of its operation and several of its relevant properties.

1.4.1 FEL basics

A free-electron laser is indeed a laser in the true sense of the word - its output is generated by stimulated emission of radiation. Its emission properties are essentially the same as any other laser - spatial coherence, mono-chromaticity, *etc.*, but the method used to generate the laser output in a FEL is much different than in a conventional laser [28, 29]. In most lasers, light is generated when bound electrons that have been populated into an excited state decay into a lower energy states and emit

photons. In a FEL, photons are emitted as synchrotron radiation by electrons traveling at relativistic speeds that are forced to undergo a spatial undulation (*i.e.* they wiggle back and forth) by passing through a spatially varying magnetic field. The electrons are not bound to any atoms, hence the term *free-electron* laser. The undulation is induced by stationary magnets (a wiggler) of alternating polarity in a linear or helical structure that produce a sinusoidally varying magnetic field (in space). By tuning either the energy of the electron beam or the strength of the magnetic field, the laser wavelength can be tuned over a wide range. This tunability makes the FEL an attractive research tool, and in fact FELs have been built to operate from the deep UV regime, all the way down to terahertz frequencies. The output wavelength of the FEL is related to the wiggler spacing, $\lambda_{wiggler}$, by the following equation:

$$\lambda_{FEL} = \frac{\lambda_{wiggler}}{2\gamma^2}\left[1 + \kappa^2(B)\right] \tag{1.15}$$

where γ is the electron beam energy in terms of its rest mass, and κ is a term that is dependendent on the magnitude and orientation of the magnetic field, B [28, 30]. A schematic picture of the FEL is shown in figure 1.6.

1.4.2 FEL at Vanderbilt

The W.M. Keck free-electron laser at Vanderbilt uses an S-band klystron to power a ~ 3 m long radio-frequency (RF) linear accelerator that accelerates the electrons to roughly 43 MeV before they are injected into the wiggler [31]. The RF field extracts electrons from a thermionic cathode (U.S. Patent No. 4,641,103, John Madey et. al.,

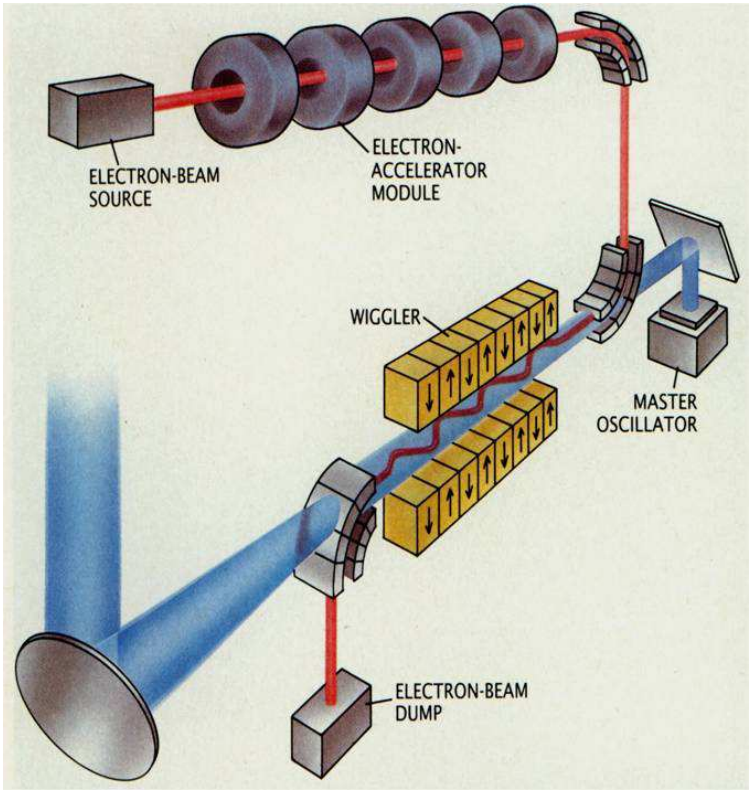

Figure 1.6: Schematic illustration of the FEL.

microwave electron gun) at a repetition rate of 30 Hz., with each RF pulse lasting approximately 8 μs. During the RF pulse, electrons are extracted from the cathode in discrete bunches at a rate of 2.86 GHz, corresponding to the frequency of the S-band. These electron bunches are then further compressed before being injected into the wiggler, and the end result is a $\sim$ 4 μs long "macropulse" which comprises some 10^4 "micropulses", each of which are 1 ps long and 350 ps apart (2.86 GHz^{-1} $\sim$ 350 ps). The pulse structure of the FEL is shown schematically in figure 1.7. It is important to note here that previous work on tissue ablation using the FEL concluded that the micropulse structure of the FEL did not significantly affect the dynamics of ablation, meaning that the pulse can be conceptualized as a continuous 4-6 μs long laser pulse

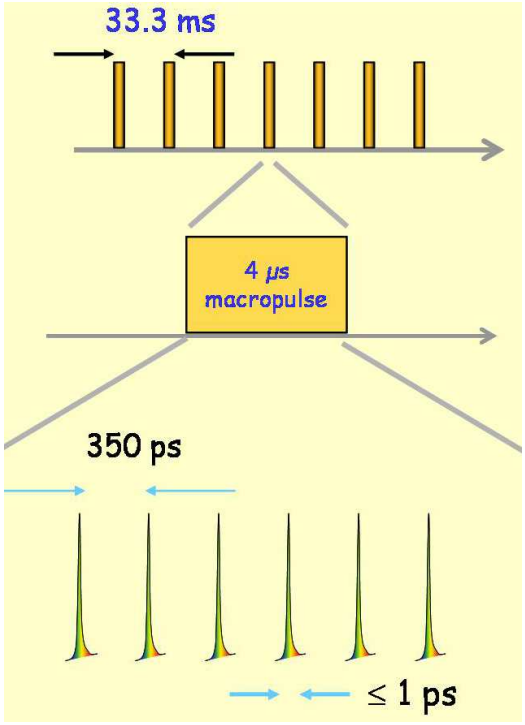

Figure 1.7: Pulse structure of the FEL

[32, 33]. We adopt this convention throughout the rest of the dissertation, and any reference to the FEL "laser pulse" is referring to the macropulse.

1.4.2.1 Spectral and temporal structure

The primary advantage of the FEL is its wavelength tunability. The VU FEL has the capability to tune continuously from 2-10 μm, accessing any wavelength in the so-called "molecular fingerprint" region of the electromagnetic spectrum. For polymer ablation experiments, this allows the user to tune the FEL to a molecular resonance of a polymer target or solvent matrix, and couple energy into resonant vibration modes. Figure 1.8 shows output spectra for various wavelength tunes of the FEL (left), along with the temporal structure of the macropulse (right). Notice that both the temporal

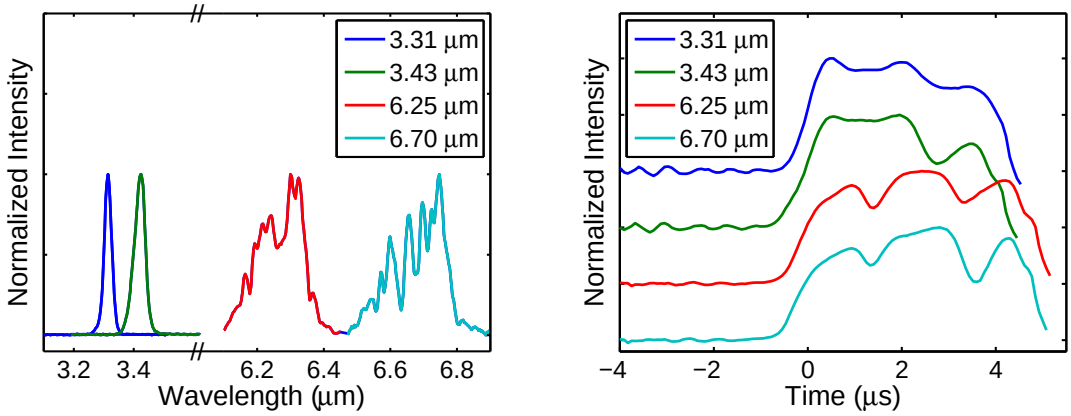

Figure 1.8: Intensity of various wavelengths of the FEL as a function of fluence (left) and the corresponding intensity of the macropulses as a function of fluence (right).

pulse width and the spectral bandwidth broaden at the longer wavelengths. This serves to decrease the intensity of the laser irradiation and to decrease the effective material absorption coefficients for narrow vibrational resonances (the vibrational resonances are typically more narrow than the FEL bandwidth - see sections 2.1.1 and A.2 for more details).

Previous theoretical work regarding the effects of laser repetition rate on ablation suggested that high pulse repetition frequencies (PRF) and modest pulse energies would more readily produce a molecular vapor than low PRF, high energy pulses [34]. Although the FEL micropulses have these qualities, this is not the case with resonant IR ablation of polymers, as we will se in later chapters.

1.4.2.2 Spatial properties

The transverse electromagnetic mode (TEM) of the FEL output is of the lowest order, TEM_{00}, and the spatial shape of the beam is therefore Gaussian. Mathemati-

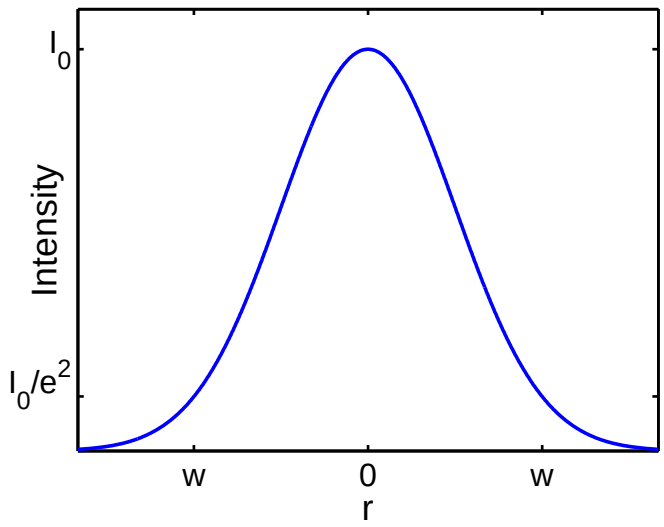

Figure 1.9: Schematic representation of a Gaussian laser pulse showing intensity as a function of the radial coordinate, r.

cally, the spatial profile can be written as

$$I(r) = I_0 e^{-\frac{2r^2}{w^2}} \tag{1.16}$$

where $I(r)$ is the beam intensity as a function of the radial coordinate, r, I_0 is the intensity at the center of the beam, and w is the beam spot size. The laser spot size is an important parameter in ablation experiments, as it determines the fluence at the target surface. The conventional definition for the spot size (radius) of a Gaussian laser beam is the point at which the intensity falls to $1/e^2$ of its peak value, as it is defined in equation 1.16. Figure 1.9 shows a schematic spatial profile of a Gaussian laser pulse with the spot size, peak intensity, and $1/e^2$ points labeled.

To measure the spot size of a Gaussian beam, one typically uses the "knife-edge" method. A razorblade is passed in front of the beam to block it while the transmitted

intensity is recorded as a function of the razor's position. The result is a plot of cumulative intensity as a function of position, which is the integral of the beam profile. Since the integral of a Gaussian is an error function ($erf(r)$), the data points taken using the knife-edge method may be fit to an error function, and the proper spot size parameter can be extracted. Laser beam spot sizes quoted in the rest of this dissertation were measured this way and were accurate to within 10% (an upper bound on the error function fits).

1.5 Summary

For the past several decades, laser ablation of polymers has been an active area of research offering many scientific challenges and technological potential. The background presented in this chapter is by no means a complete summary of work done in the field, but it is intended to introduce the concepts and experimental aspects most relevant to the work presented in the following chapters on resonant infrared laser ablation.

Given that resonant IR photons excite localized molecular vibrations in a polymer which couple to the phonon bath on relatively short timescales, it is expected that RIR ablation should proceed by some photothermal mechanism, as opposed to a photochemical one. Normal boiling is not a valid physical concept for polymer melts, and therefore the only plausible thermal mechanism for laser material removal is spinodal decomposition. It will be shown in chapters II and III that this mechanism is indeed responsible for RIR laser ablation of model polymer systems.

Heuristic ablation models mathematically describe experimental observations such

as laser etching rates and plume shielding, and give some physical insight into the ablation process. For instance, it will be shown using etch depth vs. fluence data in the following chapters that RIR ablation of polystyrene and poly(ethylene glycol) is best described by a plume shielding ablation model with a γ factor of ~ 0.3. Time resolved shadowgraph images of the ablation plumes help to confirm these predictions, as visible material removal and plume formation is evident throughout the timeframe of the laser pulse.

An analysis of the thermal and stress confinement times almost always accompanies discussions on laser ablation, as these time scales determine the rates of mechanical and thermal energy diffusion. We will generally ignore the stress confinement time in the remaining chapters since it is orders of magnitude shorter than the FEL macropulse, but we will make frequent use of the thermal confinement time to justify approximations which simplify the time-dependent heat diffusion equation.

The FEL is a unique laser whose wavelength tunability makes it an ideal tool to study RIR polymer ablation. By tuning to different resonant absorption modes of a polymer, for instance, we may investigate the effects of the absorption coefficient on the dynamics of ablation, as we do in the next two chapters, or how it affects the properties of deposited polymer thin-films, as discussed in chapters IV and V.

CHAPTER II

MODEL MATERIAL I: POLYSTYRENE

As discussed in chapter I, resonant-infrared pulsed laser deposition (RIR-PLD) has attracted considerable interest since its discovery in 2001 due to its success in depositing polymer thin-films [35, 15, 36]. As will be shown in chapters IV and V, the RIR-PLD process has been applied to include the deposition of a conducting polymer [37, 38], and functional polymer light emitting diodes (PLEDs) have been fabricated by RIR-PLD [39]. Despite the widespread success of RIR-PLD, however, the fundamental mechanisms that govern the process of resonant IR polymer ablation and deposition remain unknown. Having a better understanding of these mechanisms would allow for better process control, as issues such as film roughness and resonant wavelength selection can currently be addressed only through a matter of trial and error.

What is known about the IR ablation process is that when IR light is used as an ablation source instead of UV, the possibility of photochemistry is practically negligible and the potential for intact polymer deposition is promising. It is uncertain, however, the extent to which thermal damage caused by a laser-induced temperature rise degrades the quality and performance of deposited polymer films. In this chapter, we describe both static and time-resolved experiments aimed at addressing this issue. We investigate the fundamental mechanisms of resonant-infrared laser ablation of polymers using polystyrene as a model material. Time-resolved plume shadowgra-

phy coupled with laser-induced temperature-rise calculations indicate that spinodal decomposition of a superheated surface layer is the primary mechanism for the initial stages of material removal. The majority of the ablated material is then released by way of recoil-induced ejection of liquid which proceeds for some tens of microseconds following a ~ 5 μs laser pulse excitation. The proposed ablation mechanism helps to explain previously observed properties of laser-deposited thin films, such as high surface roughness and film molecular weight distribution.

2.1 PS overview

Polystyrene (PS) was chosen as a representative model polymer system for our ablation studies for several reasons, perhaps the most important of which is the widespread use of PS as a standard in matrix-assisted laser desorption and ionization (MALDI) [40] and gel-permeation chromatography [3]. Thus, it is very well characterized and its properties are well known. Moreover, since it is used as a standard in mass analysis, measuring the molecular weight of laser-ablated material is straightforward.

The chemical structure of PS is shown in figure 2.1. The structure of the polymer is simple: C-H bonds along the backbone with a pendant benzene ring at every other site. All of the polystyrene used in this work was atactic, that is to say that the position of the benzene rings along the chain were located randomly (not necessarily on one side of the chain or the other), and the bulk polymer was therefore amorphous. Also labeled in figure 2.1 are two C-H stretching modes. The longer wavelength mode, 3.43 μm, corresponds to the aliphatic C-H stretch, while the shorter one corresponds the aromatic C-H stretch.

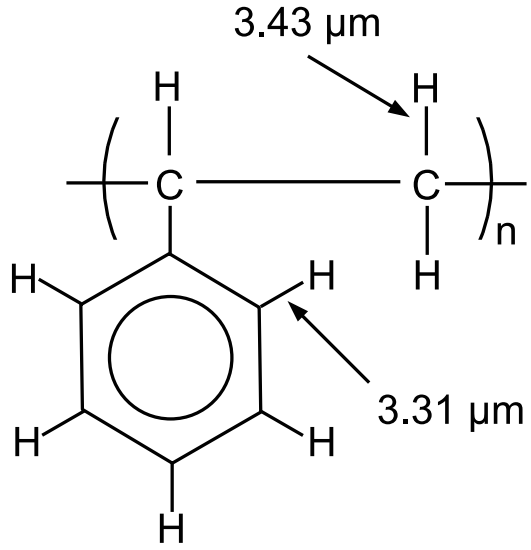

Figure 2.1: Chemical structure of polystyrene with two C-H stretching modes labeled.

2.1.1 Vibrational spectrum and FEL mode-overlap

Figure 2.2 shows an FTIR spectrum of polystyrene in the 2-7 μm region. Also shown in the figure are four different "tunes" of the FEL (described in section 1.4) that correspond to resonant vibrational excitation. The FEL spectra are shown to demonstrate the overlap of the FEL bandwidth with the PS vibrational resonances. At longer wavelengths, the FEL bandwidth is broader, and the distortion of the spectral shape comes from the atmospheric absorption of water vapor in the mid-IR (the spectra are taken in air). Since the FEL typically travels through 1-3 meters of air before arriving at the target surface (see appendix C for pictures of the FEL beam path), this is indeed the spectrum that the polymer sees during irradiation.

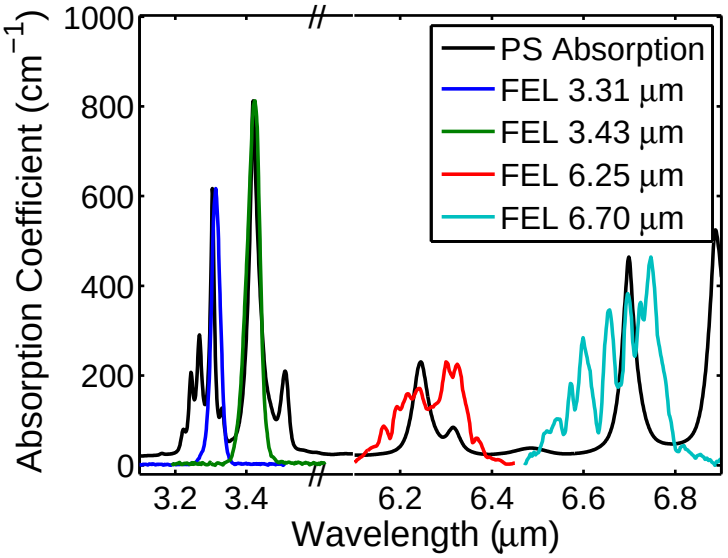

Figure 2.2: FTIR spectrum of polystyrene showing the absorption coefficient as a function of wavelength along with resonant FEL excitation spectra.

2.1.2 Measurement of effective absorption coefficients

It is obvious from figure 2.2 that the bandwidth of the FEL serves to *decrease* the effective absorption coefficient of PS for a given FEL targeted wavelength. This is most pronounced in the two longer-wavelength spectra at 6.25 and 6.70 μm where much of the FEL output goes into non-resonant modes of the PS. Therefore, one must measure the *effective* absorption coefficient of PS when using the FEL, by using the FEL itself rather than a spectrometer. For each of the FEL center wavelengths shown in figure 2.2, the effective absorption coefficient was measured by recording the transmission of the unfocused FEL beam through a 38 μm thick freestanding film of PS (a NIST FTIR calibration sample) for a number of beam energies. The linear absorption coefficient was then calculated from Beer's Law as:

$$\alpha = \frac{-\ln \frac{I}{I_0}}{x} = \frac{-\ln T}{x} \tag{2.1}$$

Table II.1: Effective absorption coefficients of polystyrene for various FEL wavelengths. The effective $1/\alpha_{eff}$ penetration depth, μ_{eff}, is also shown.

Wavelength (μm)	**Assignment**	α_{eff} **(cm^{-1})**	μ_{eff} **(μm)**
3.31	Aromatic C-H Stretch	354 ± 54	28.2 ± 4.3
3.43	Backbone C-H Stretch	551 ± 36	18.1 ± 1.2
4.75	Non-resonant	55.4 ± 8.2	180.4 ± 26.6
6.25	C=C-C Stretch	197 ± 3.4	50.1 ± 0.9
6.70	C=C-C Stretch	234 ± 17	42.5 ± 3.1

where x = the film thickness and T is the transmittance. The results are displayed in table II.1. The error given is the standard deviation of a total of 16 measurements.

2.2 Experimental Details

2.2.1 Laser source

The ablation experiments were performed at the W. M. Keck Free-electron Laser Center [31]. The FEL has already been discussed in detail in section 1.4 and therefore is not described here. The wavelengths used in these experiments were those shown in table II.1.

2.2.2 Target preparation

Polystyrene targets were made by melting commercially purchased polystyrene beads (M_w = 224 kDa, polydispersity = 1.8) into custom fabricated aluminum target wells 3 mm deep. To ensure similar surface conditions between laser shots, the polystyrene targets were cooled, extracted from the target well, and flipped to expose

the surface that melted against the bottom face of the polished aluminum target well. Satisfying this criterion is essential in order to accurately measure crater etch depths and obtain consistent plume shadowgraph images.

2.2.3 Bright-field plume imaging

Time-resolved plume shadowgraphs were recorded using the setup displayed in figure 2.3. A nitrogen-pumped dye laser running parallel to the target surface illuminated an area several millimeters above the target surface; a telephoto lens then imaged the silhouette of the target surface onto a color CCD. Time resolution was limited by the excited-state lifetime of the fluorescent dye and was determined to be roughly 50 ns by measuring the the temporal profile of the pulse with a fast Si photodiode. An electronic delay generator (Stanford Research Systems DG535) was used to vary the time delay between the pump and probe pulse.

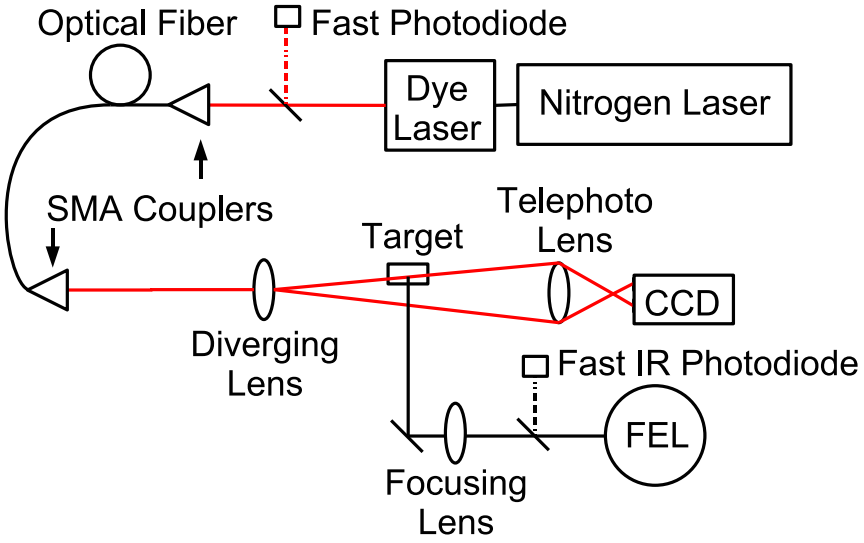

Figure 2.3: Schematic diagram of the bright-field plume imaging apparatus.

2.2.4 Etch-depth measurements

Etch depths from single FEL pulses were measured using a stylus profilometer (Veeco Dektak 150). For a given fluence, five shots were delivered to fresh areas of the polystyrene target surface. The etch depth was then measured for each individual shot and the five measurements were averaged to obtain a single value. Note that the etch depth value is an average of five independent measurements, rather than one measurement of five pulses.

2.3 Results and Discussion

2.3.1 Crater analysis

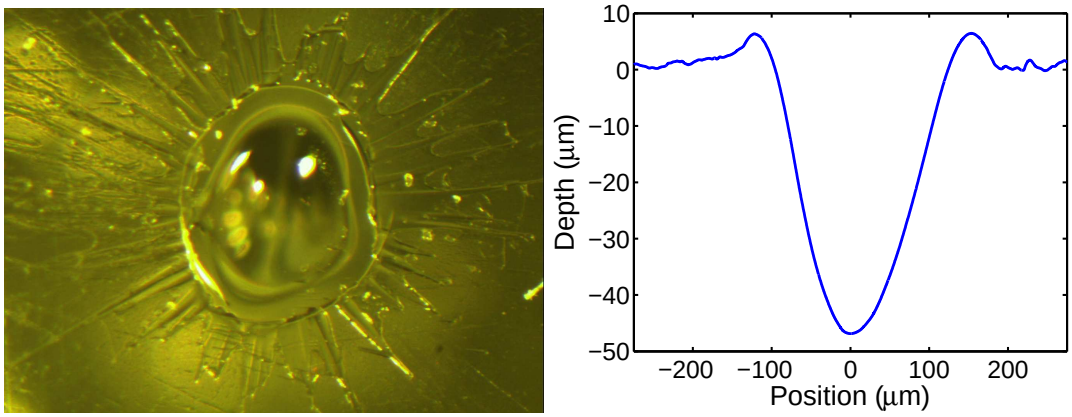

Figure 2.4: Optical micrograph of a typical ablation crater and the corresponding profilometer scan.

Figure 2.4 shows a typical optical image of an ablation crater, as well as a typical Dektak profilometer scan. The figure exhibits three main features: gross material

removal in and around the center of the crater, a raised "lip" of material at the periphery of the crater, and radially-oriented strands of material deposited outside the lip of the crater. The shape of the crater roughly parallels that of the gaussian laser beam, but with a slightly reduced radius (typical $1/e^2$ spot radii used for ablation were 150-200 μm). Ablation is a threshold-activated process which requires a certain volumetric energy density to occur, and away from the center of the laser beam the energy density is not high enough to initiate ablation. Rather than ablate material, the outer portions of the laser pulse can deposit only enough energy to heat and expand the target which then freezes sometime after the pulse terminates. The result of the process is a region of rarefied material residing at the edge of the crater boundary as is seen in figure 2.4.

Another feature of figure 2.4 is the presence of redeposited strands of material around the lip of the ablation crater. The distribution of the recast material suggests that the plume had a significant velocity component parallel to the target surface. One mechanism that accounts for a non-normal plume velocity is that of recoil-induced ejection [22]. However, recoil-induced ejection explains the presence of the recast material but not its orientation. The material has frozen into strands rather than a continuous ring uniformly distributed. According to shadowgraph images presented in section 2.3.3, the recoil-induced liquid emerges from the target as a continuous cylinder of liquid, but apparently breaks apart at some later time according to figure 2.4. This is a well-known phenomenon and is the result of Plateau-Rayleigh instabilities of the expanding fluid. Much in the same way that a liquid jet breaks into smaller droplets in order to reduce its surface tension while moving through a less

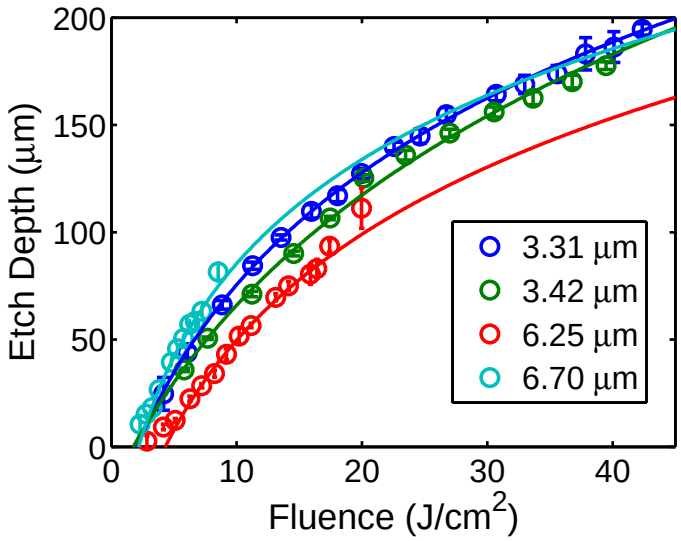

.

Figure 2.5: Etch depth as a function of fluence for various excitation wavelengths of polystyrene. The curves are a fit to equation 2.2

dense fluid, the three-dimensional cylinder of fluid ejected by recoil force breaks into smaller jets as it falls to the target surface.

2.3.2 Etch depth measurements and comparison to heuristic models

Etch depth vs. fluence data are shown in figure 2.5 for ablation of polystyrene at various resonant wavelengths. Each data point represents the average of five single-shot measurements, and the error bars are the standard deviation of the five trials. The curves all seem to have the same general shape, and the lines are fits to the heuristic plume shielding model discussed in chapter I:

$$\delta = \frac{1}{\alpha\gamma} ln \left[\gamma \left(\frac{\Phi_0}{\Phi_{th}} - 1 \right) + 1 \right] \tag{2.2}$$

where δ is the etch depth, α is the absorption coefficient, γ is the plume shielding factor, Φ_0 is the laser fluence, and Φ_{th} is the threshold fluence for ablation. Recall that this model assumes a steady state ablation process and allows for the ablation plume to attenuate the laser beam. If $\gamma \to 0$, then there is no laser plume shielding and a steady-state ablation model is recovered, and if $\gamma \to 1$ then there is complete plume shielding and a "blow-off" model is recovered. The values of γ for the fits in figure 2.5 are on the order of ~ 0.25, which suggest a weak to moderate plume shielding. This is in agreement with the shadowgraph images shown later in section 2.3.3 which indicate that plume generation begins well within the time frame of the laser pulse and likely shields the target from absorbing all of the laser light.

According to equation 2.2, the etch rate should be inversely proportional to the absorption coefficient. For the data shown in figure 2.5, this is true except for the 6.25 μm data, which has a lower ablation rate than any other mode despite it having the smallest absorption coefficient. Given that the FEL bandwidth in this wavelength region is much wider than the spectral width of the vibrational modes, it is difficult to compare the ablation rates at longer wavelengths with the shorter ones around 3 μm since so much laser energy is only coupled weakly into non-resonant modes of the target.

2.3.3 Plume dynamics

Time-resolved shadowgraph images were taken from time $t = 0$ (the beginning of the FEL pulse), until several hundred μs after the FEL pulse was over and are presented in figure 2.6 for a wavelength of 3.43 μm and fluence of $\Phi = 9.2$ J/cm^2.

These laser conditions are typical for thin-film deposition. The progression of the images shows material removal beginning at around 2 μs after the beginning of the FEL pulse, and lasting for approximately 30-40 μs until the ablation ceases and the plume expands into the ambient. Analyzing the images in figure 2.6, we can identify three regimes that encompass the event from beginning to end: 1) the initial expansion of a thin layer of gaseous material which drives a shockwave normal to the surface (2-5 μs), 2) the removal of relatively large amounts of liquid material (4-30 μs), and 3) the expansion of the plume into the ambient ($t > 30$ μs). Since regimes 1) and 2) involve material removal, it is instructive to focus the discussion in these areas in order to gain better insight into ablation mechanisms.

The first stage of the ablation is characterized by the expansion of a gaseous plume of material. Given that the target is a polymer of relatively high molecular weight (224 kDa), the only way that it can get into the gas phase is by undergoing decomposition. Work on thermal degradation of polymers along with theoretical calculations has shown that an upper mass limit for producing polymers in the gas phase is $\sim$ 1000 Da [19]. For chains longer than this, it is energetically more favorable to decompose into smaller subunits before liberating themselves from the intermolecular forces that bind them to other polymer chains. Thus, the evidence of an initial gaseous plume implies that some portion of the target has been decomposed. Moreover, temperature-rise calculations presented in section 2.3.4 show that the surface temperature induced by the absorption of a resonant-IR laser pulse is indeed high enough to drive the polystyrene into thermal instability and decompose the surface region of the target. Previous work also showed that the molecular weight of IR laser-deposited PS films

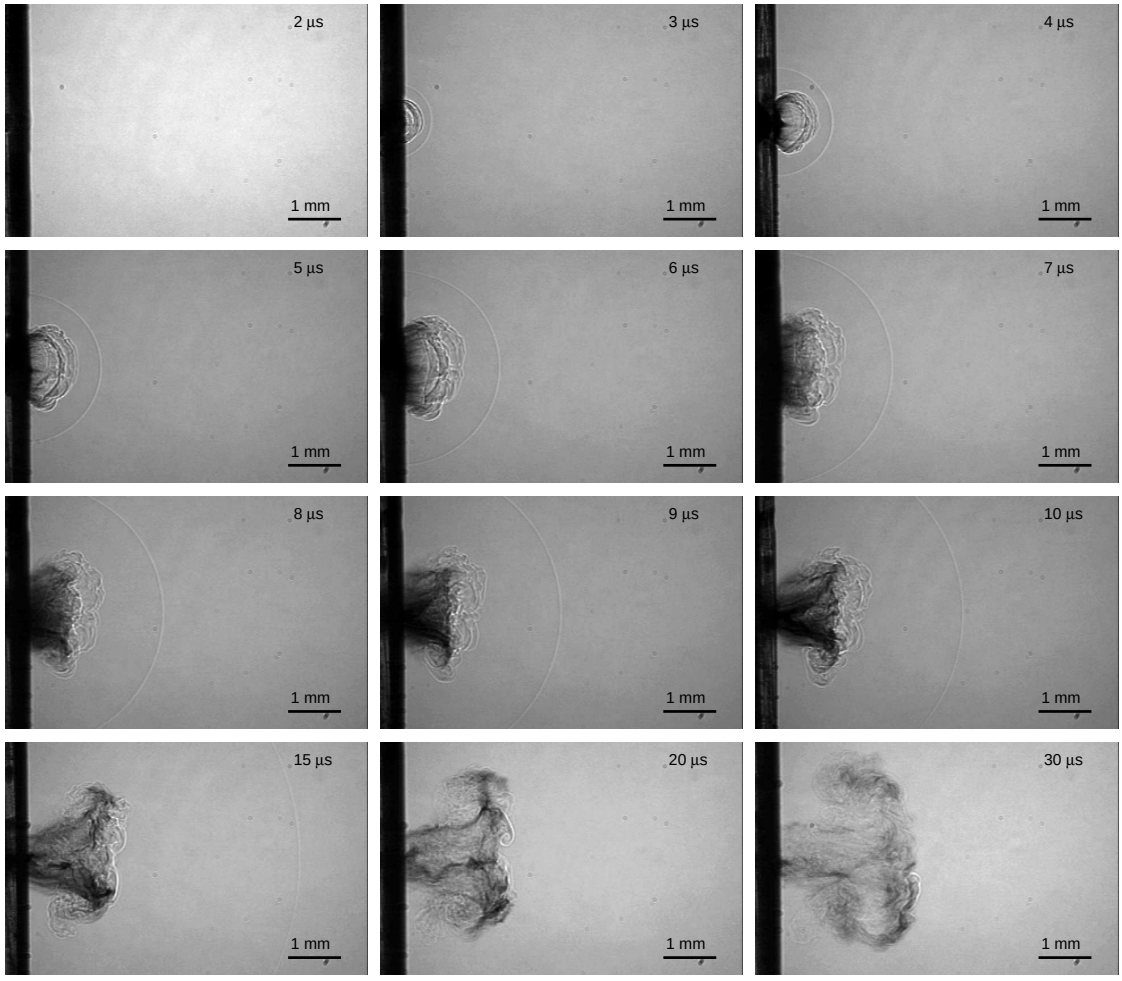

Figure 2.6: Shadowgraphs of polystyrene ablation at 3.43 μm, $\Phi = 9.2$ J/cm^2.

was somewhat reduced with respect to that of the starting material [36].

The images shown in figure 2.6 are similar to those previously observed during resonant IR ablation of water [22, 23], where phase explosion followed by the recoil-induced ejection of liquid were determined to be the dominant ablation mechanisms. These concepts were explained in section 1.3.4, but are briefly summarized here:

The laser superheats the surface region of the target to the spinodal point, driving it into thermodynamic instabilty. The superheated region then undergoes a phase

explosion (spinodal decomposition) and instantaneously decomposes into a mixture of gas and liquid droplets. The recoil momentum imparted to the target as the gaseous plume expands outward acts like a piston that compresses a laser-melted region of the target. The compression drives the liquid polymer from the periphery of the target at a characteristic non-normal angle (evident in figure 2.6 at 6 μs), producing a cylindrical liquid film. Given the similarity between the images in figure 2.6 and images of recoil-induced ejection that exist in the literature [22, 23] of water and tissue, we believe that the same mechansisms are responsible for material removal in the case of IR ablation of polymers. Moreover, laser-induced temperature rise calculations to be presented in section 2.3.4 also support this idea.

At times longer than 15 μs the cylindrical liquid film begins to become significantly less dense as it expands and vortices form at the plume front due to Rayleigh-Taylor instabilities. These instabilities occur when a heavy fluid is accelerated into a stagnant, lighter fluid [17, 41]. Perturbations of the fluid interface grow exponentially with time at a rate proportional to $e^{\eta t}$, where η is defined as

$$\eta^2 = kaA \tag{2.3}$$

where k is the wavevector of the perturbation, a is the accelleration, dv/dt, of the plume, and A is the Atwood number:

$$A = \frac{\rho_p - \rho_b}{\rho_p + \rho_b} \tag{2.4}$$

Here, ρ_p and ρ_b are the densities of the plume and background gas, respectively [42, 43]. The interface between the plume and background is stable when $\rho_p > \rho_b$, but becomes unstable if $\rho_p < \rho_b$ creating turbulence such as that observed in figure 2.6 at 15 μs. The turbulence occurs after the plume expands and becomes less dense than the background air. In vacuum, it is expected that vortex fomation in the plume would not occur since the density of the background gas is less than the plume density. Previous attempts have been made to image the ablation plume in vacuum, but were unsuccessful. Since the plume is not impeded by atmospheric pressure, it expands rapidly and is never dense enough to strongly attenuate and scatter light from the probe beam, which causes the captured images to be faint, at best. At lower laser fluences, the shadowgraph images appear different. Figure 2.7 shows shadowgraph images for 3.43 μm excitation, the same wavelength as above, but with fluences of 9.2, 5.2, and 2.3 J/cm^2, at 3, 8, and 15 μs. The differences in the plume progression is a result of the smaller ablation area, rather than a difference in ablation mechanism. For instance, a lower fluence is capable of producing ablation only in the most intense portion of the Gaussian beam. Therefore, the radii of both the phase exploded and melted regions are smaller when a lower fluence is used. Material that is expelled as liquid *via* a recoil force behaves more like a continuous jet rather than a hollow cylinder of fluid as the fluence is decreased due to the decreased radius of the vaporized core. This concept is easily visualized by referring back to figure 1.4 and explains why jet-like behavior of the plume is more pronounced at low fluences. Unfortunately, the plume size generated at low fluences approaches the resolution limit of our shadowgraphy system, and resolving its details in order to further compare

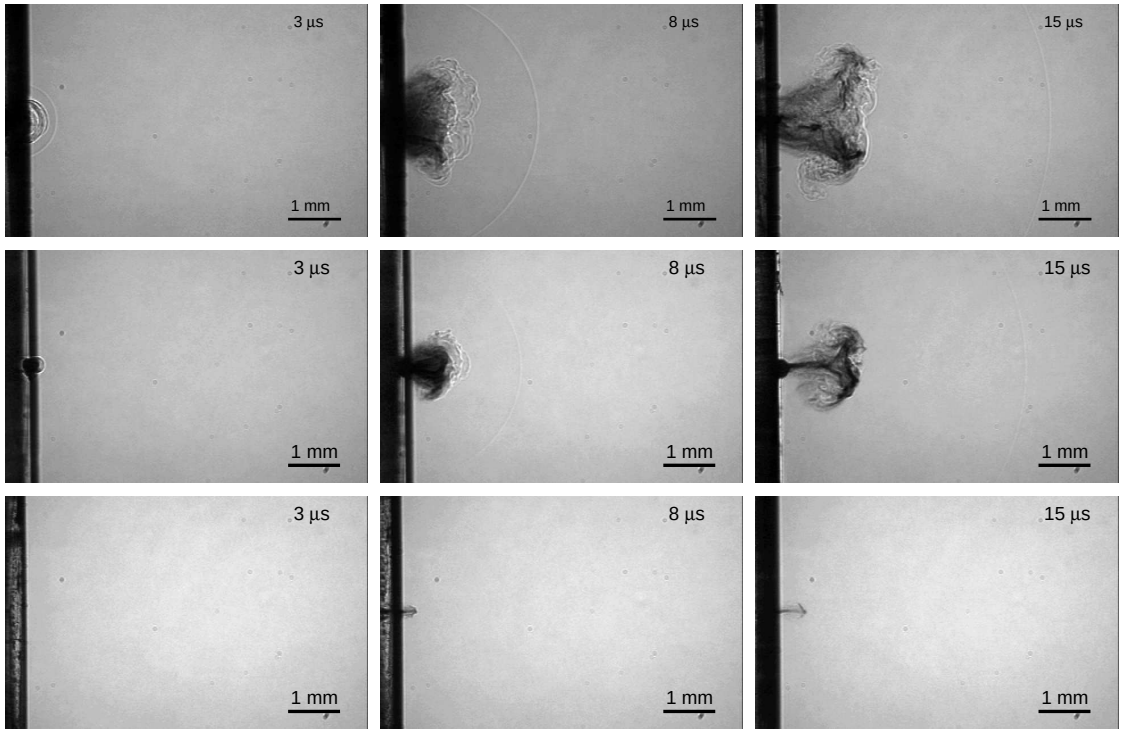

Figure 2.7: Shadowgraphs of polystyrene ablation at 3.43 μm. Top row: $\Phi = 9.2$ J/cm^2, second row: $\Phi = 5.2$ J/cm^2, bottom row: $\Phi = 2.3$ J/cm^2.

it to higher fluence ablation is therefore difficult.

Another important feature of figure 2.7 is that as the fluence decreases, the time at which visible ablation occurs is delayed. Since ablation requires a certain threshold energy density to occur, the ablation onset time should be inversely proportional to the fluence (*e.g.* doubling the fluence should halve the time for ablation to begin). The ablation onset time was recorded as a function of fluence by examining shadowgraph images, and is displayed in figure 2.8. The error bars were assigned as $\pm$ 500 ns for each data point based on the estimated precision from shot to shot (slight variations in the target angle with respect to the camera can produce delays up to 500 ns).

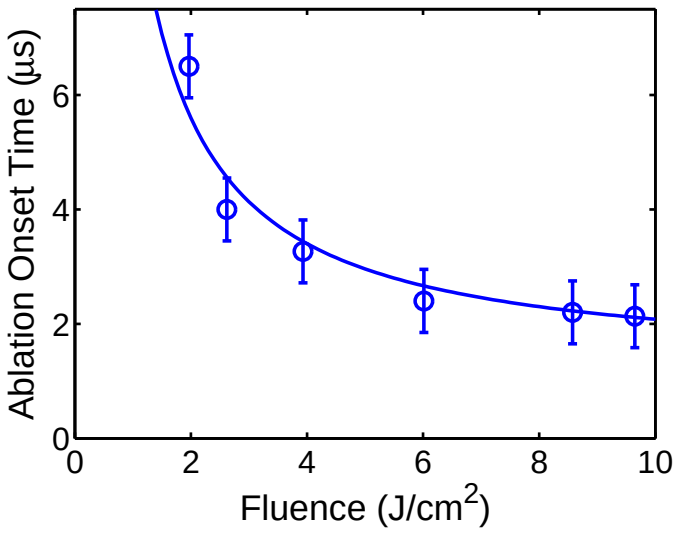

Figure 2.8: Ablation onset time as a function of fluence for PS ablated at 3.43 μm. The line is a fit proportional to $1/\Phi$.

The line is a fit proportional to $1/\Phi$. This further supports the idea that a thermal process such as spinodal decomposition is responsible for the initial stages of material removal.

2.3.4 Thermal calculations

In order to determine whether spinodal decomposition followed by recoil-induced ejection of material could indeed be responsible for ablation, finite-element calculations were performed to estimate the temperatures reached in the polymer target after laser irradiation. To accurately model the temperature rise, one must solve the time-dependent heat diffusion equation:

$$\rho c_p \frac{\partial T}{\partial t} = Q + \kappa \nabla^2 T \tag{2.5}$$

where ρ is the material density, c_p is the specific heat, Q is the laser source (heating) term, and κ is the thermal conductivity. We can reduce this equation to one spatial dimension, however, since the laser spot size is much larger than the optical penetration depth and the heat effectively propagates in one dimension. Moreover, for a polymer with a low thermal conductivity, the equation may be simplified further by eliminating the diffusion term, $\kappa\nabla^2 T$. This action is easily justified by considering the thermal-diffusion time discussed in chapter I:

$$\tau_{th} = \frac{c_p \rho}{\alpha^2 \kappa} \tag{2.6}$$

which describes the amount of time it takes for laser energy deposited as heat to diffuse out from the focal volume . For polystyrene, $c_p = 1.3$ J/g/°K, $\rho = 1.05$ g/cm^2 $\kappa =$ 0.08 W/m/°K, and using the absorption coefficients used in table II.1, the thermal diffusion time is 5-50 ms. This timescale is approximately 1000 times longer than the duration of the laser pulse so that the energy is thermally confined during laser irradiation and we may neglect the diffusion term in equation 1.13. Note that if this criterion is satisfied in the z-dimension, it must also hold in the x and y-dimensions since the laser spot size is larger than the optical penetration depth, and the effect of thermal diffusions along these dimensions is even smaller. After eliminating the diffusion term, we may write

$$\frac{\partial T}{\partial t} = \frac{Q}{\rho c_p} \tag{2.7}$$

The heating source, Q, describes the energy density deposited by the laser which can be expressed as

$$Q = \frac{I}{\alpha} \tag{2.8}$$

where I is the laser irradiance (fluence per time). Inserting this into equation 2.7 and integrating to solve for T yields

$$\Delta T = \frac{\alpha I \Delta t}{\rho c_p} = \frac{\alpha \Phi}{\rho c_p} \tag{2.9}$$

for the average temperature increase in polystyrene after laser absorption, assuming that there is no time dependence of any of the variables. To estimate the temperature as accurately as possible, finite-element calculations were performed which assumed a spatially Gaussian laser beam in x and y and an exponential laser profile in the z-direction of the target (Beer's law). Including the spatial dependence of the laser intensity modifies equation 2.9 by a Gaussian and an exponential function, and an analytical expression for the temperature after laser absorption is:

$$T = T_i + \frac{2\alpha\Phi_0}{\rho c_p} \exp\left(-2\frac{x^2 + y^2}{w^2} - \alpha z\right) \tag{2.10}$$

Here the coordinate system origin is at the center of the laser beam on the surface of the target, and moving into the target corresponds to increasing z. The extra factor of 2 comes from normalization.

In order to calculate the temperature profile which induces ablation, we use equation 2.10 with a fluence of 2.0 J/cm^2, which corresponds to ablation right at threshold.

Performing the calculation for any fluence above the ablation threshold would not be meaningful since material removal begins within the time frame of the laser pulse as the fluence is increased above threshold. This means that the target would no longer be continuous or stationary, thermal confinement would not hold as the plume rapidly expanded and cooled, and the ablation plume would serve to shield the target surface from the laser pulse. Since these considerations would violoate the assumptions used to derive equation 2.10, temperature calculations must be done at or below the threshold fluence. Figure 2.9 shows a cross-sectional image of of the laser-induced temperature rise for a wavelength of 3.43 μm and a fluence of 2.0 J/cm^2. It is impor-

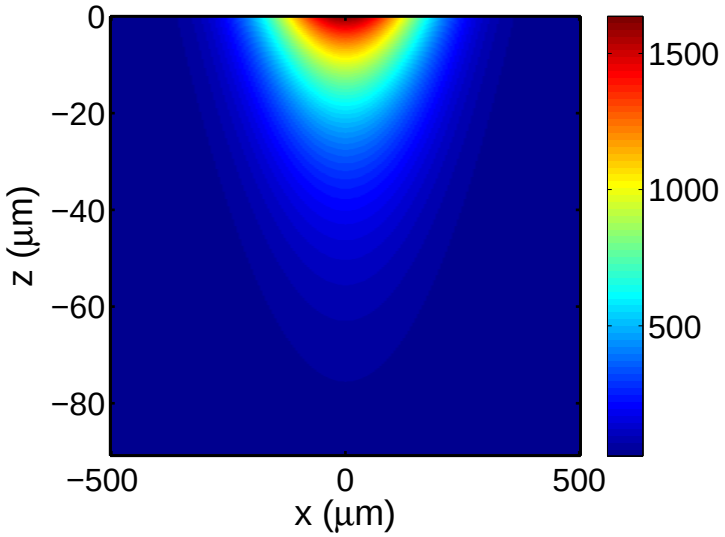

Figure 2.9: Calculated laser-induced temperature rise as a function of x and z in polystyrene using 3.43 μm excitation and $\Phi = 2.0$ J/cm^2. The calculation assumes a Gaussian laser beam and an exponential absorption profile in the target.

tant to point out that the temperature calculated in this case is a slight overestimate

because it doesn't take into account the enthalpies associated with any phase transitions. Given the magnitude of total energy deposited into the target, however, it is unlikely that this would be a significant correction.

Previous studies on the sudden "boiling-up" temperatures of polystyrene estimate a spontaneous boiling-up temperature in the range of 1000-1100 K, for a heating time of 110 μs [20, 21]. Such a phenomenon of spontaneous boiling-up of polymer melts can only be explained through a spinodal decomposition process, since classical boiling is not a valid physical concept. The calculation shown in figure 2.9 demonstrates that the PS target reaches 1000 °C down to a depth of $\sim$ 10 μm, indicating that spinodal decomposition is possible at and immediately below the surface of the target.

2.3.4.1 Temperature-dependent parameters

The laser-induced temperature rise calculations just presented assume that all variables are independent of temperature, which is not in fact the case. In reality, most thermodynamic variables are temperature dependent and in order to calculate an accurate temperature, the dependence should be accounted for. To that end, calculations were performed which took into account the temperature dependence of the specific heat of PS, as well as the IR absorbance. The specific heat data were taken from tabulated data existing in the literature [44], and the absorption data were taken by D. M. Bubb at Rutgers University-Camden as part of a collaborative effort. The data are shown in figure 2.10. The absorption data shown are those corresponding to 3.43 μm and are presented exclusively because the temperature dependence of all other modes is essentially the same. After reaching a maximum at

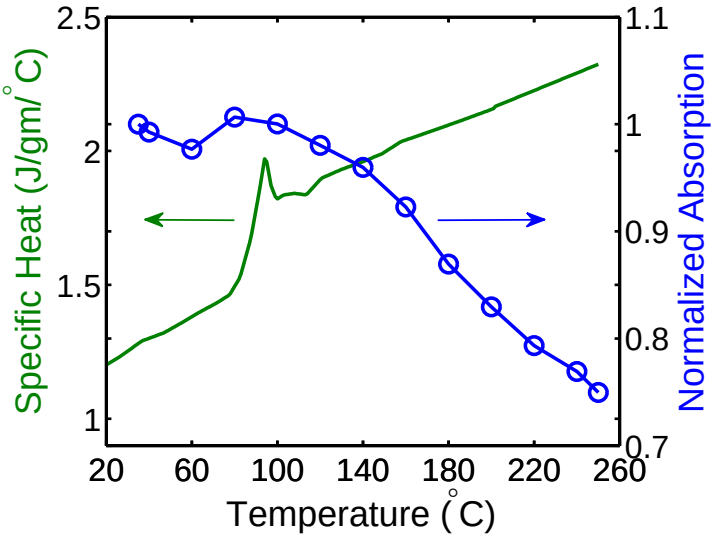

Figure 2.10: Specific heat and IR absorbance as a function of temperature for PS. Note the characteristic second order phase transition evident in c_p at $T_g \sim 95$ °C.

the glass transition temperature, the absorption decreases as the polymer heats up. This would lower the calculated temperatures shown in figure 2.9 since the absorption coefficient effectively decreases as the target is heated. Recall from equation 2.10 that $T \propto c_p^{-1}$, so the change in specific heat that PS exhibits as it is heated also serves to reduce the temperature calculated in figure 2.9.

To incorporate the time dependent variables, a finite element model using equation 2.10 was again employed, except the 4 μs long laser pulse was this time broken up into increments and the specific heat and absorption coefficient were allowed to change after each incremental absorption of energy. Thus, the equation now reads

$$T = T_i + \sum_n \frac{2\alpha(T)\Phi_n}{\rho c_p(T)} \exp\left(-2\frac{x^2+y^2}{w^2} - \alpha(T)z\right) \tag{2.11}$$

where n is the number of increments of the laser pulse. The temperature-dependent

data shown in figure 2.10 only go out to 250 °C, so a calculation similar to that in figure 2.9 can only be done up to a maximum surface temperature of 250 °C. After that point, the temperature dependence of the parameters is unknown. The maximum fluence that can be used before the temperature-dependent data cuts off is ~ 0.5 J/cm^2, which is significantly less than the ~ 2.0 J/cm^2 ablation threshold for PS. Figure 2.11 shows the calculated target surface temperature as a function of time for 3.43 μm excitation and a fluence of 0.5 J/cm^2 using both static and dynamic parameters. The two temperatures are essentially the same until around 0.8 μs when

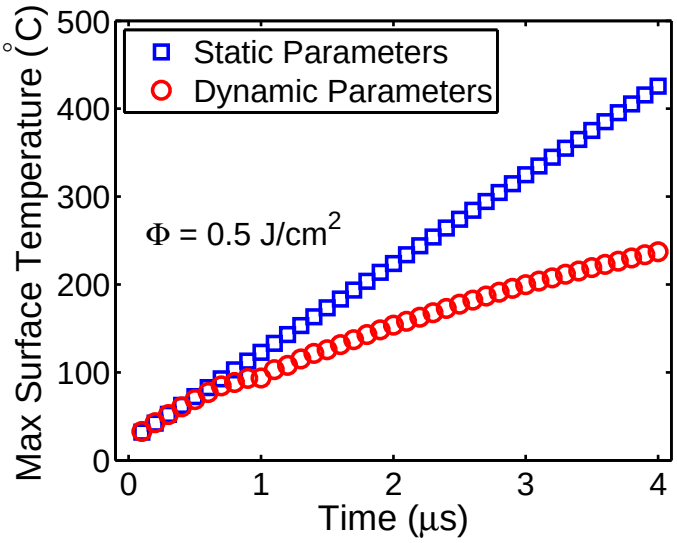

Figure 2.11: Calculated laser-induced surface temperature as a function of time near the ablation threshold using static and dynamic thermal properties. The model incorporates temperature-dependent specific heat and absorption as shown in figure 2.10.

the surface reaches the glass transition temperature ($T_g \approx 95$ °C). At that point, the specific heat and absorption coefficient change according to figure 2.10, and the

temperature increases at a lower rate than the static conditions case. At the end of the laser pulse (*i.e.* after all the laser energy has been absorbed), the calculation using static parameters yields 425 °C, while the dynamical calculation takes the surface temperature only up to the melting point, 250 °C. The temperature dependence of the thermal parameters is unknown past 250 °C, but assuming they do not change much past the melting point, the maximum surface temperature reached in figure 2.9 is reduced to approximately 1000 °C, which is in the temperature range required to induce spinodal decomposition [20, 21].

2.3.4.2 Thermal expansion

To demonstrate that the absorption of a sub-ablative fluence leads to the heating and expansion of a polystyrene target, non-resonant wavelengths were used in attempts at ablation. Off-resonance wavelengths deposit energy in a very large volume and thus create a density of excitation far below that required to initiate ablation. Figure 2.12 shows that instead of ablation craters, one measures "bumps" on the target surface where the laser was incident. The off-resonance wavelength used in these measurements was 4.75 μm. The height of the bumps increases as a function of laser fluence, indicating that the target has reached higher temperatures and expanded further. Beginning at a certain fluence, small-scale ablation does occur as the bumps "burp" before they are frozen, leaving an indentation in the apex of the bump and strands of material around the base. The linear thermal expansion coefficient is

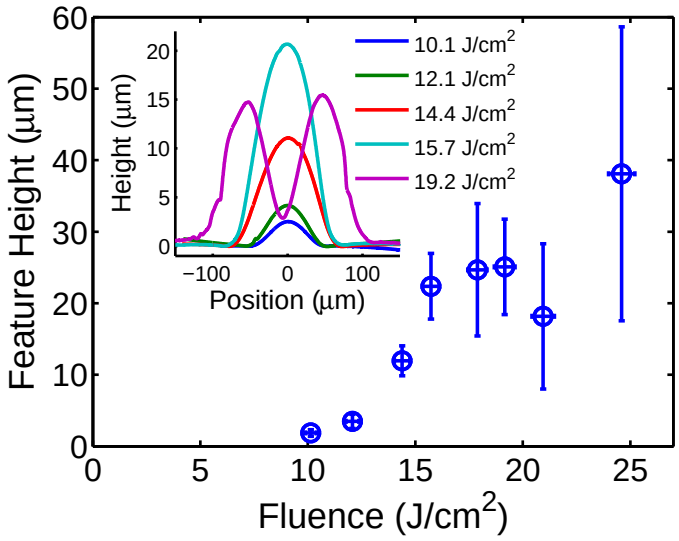

Figure 2.12: Feature height as a function of fluence created a on PS surface by 4.75 μm (non-resonant) irradiation. The inset shows representative profilometer scans of the features for selective laser fluences. Note that at higher fluences, some material is ejected from the apex of the feature.

defined as

$$\alpha_L = \frac{1}{L}(\frac{\partial L}{\partial T}) \tag{2.12}$$

and describes how the the volume of a material changes (along one dimension) as it is heated. We make use of the the linear expansion coefficient rather than the volumetric expansion coefficient since a laser-heated region of a polystyrene target is only free to expand in the dimension normal to the surface. If the absorption coefficient at a particular wavelength is known, then the height of a surface feature, h, created by a sub-ablative pulse can be calculated from equation 2.12:

$$h = \int \alpha_L \Delta T(L) dL \tag{2.13}$$

If the laser travels in the z-direction and we insert equation 2.10 for the temperature distribution into equation 2.13, then the bump height at the center of the laser spot (x=y=0) can be calculated from the following expression:

$$h = \frac{2\alpha\Phi}{\rho c_p}\alpha_L \int_0^\infty e^{-\alpha z} dz = \frac{2\Phi}{\rho c_p}\alpha_L \tag{2.14}$$

Using α_L = 8.6x10^{-5}/K [45], a fluence of 15 J/cm^2 should create a feature that is roughly 20 μm high, which is in good agreement with figure 2.12. The data in figure 2.12 display a sigmoidal dependence as a function of fluence until material is ejected from the target, while equation 2.14 predicts a linear scaling. Not considered in the derivation of the equation, however, were effects resulting from dynamic physical properties such as viscosity which affect material movement, and the fact that the thermal expansion in reality does not occur only entirely in one dimension. Note that equation 2.14 is also independent of the absorption coefficient, thus the same amount of thermal expansion should occur regardless of the wavelength used. This, however, is not exactly true since for resonant modes, anything above $\sim$ 2 J/cm^2 leads to ablation. Therefore, calculating sub-ablative expansion heights for resonant modes is difficult since the feature heights are so small.

2.4 Summary of ablation mechanisms

The mechanism that we propose to explain the data presented above can be broken into two parts, and are very similar to the mechanisms proposed in reference [22]. The initial phase of ablation (0-4 μs in figure 2.6) is caused by the spinodal decomposition

(or phase explosion) of a superheated surface layer. The laser-induced temperature that is generated in the surface region of the target is high enough to drive the polymer melt into a thermodynamically unstable state, which relaxes by exploding into a mixture of vapor and liquid. Accompanying this event is the simultaneous structural degradation of polymer chains as they must reduce their molecular weight in order to get into the gas phase. The presence of a gaseous plume in the early parts of figure 2.6, coupled with the temperature-rise calculations in the previous section strongly support this idea.

The second step of the event relies on the first, in that the recoil momentum generated by the expanding vapor plume drives the ejection of melted material. It is obvious in figure 2.6 that from 4-20 μs, liquid is expelled from the laser focal volume. Moreover, the shadowgraph images, as well as figure 2.4, illustrates that liquid material leaves the target at a non-normal angle, which is also a characteristic signature of recoil-induced ablation [22].

2.5 Conclusions

Understanding the mechanisms that govern resonant infrared ablation and that lead to the successful deposition polymeric material has remained elusive for several years. Simply analyzing the properties of thin-films deposited by RIR-PLD does not offer enough insight to the dynamics of the process in order for one to draw complete mechanistic conclusions. Through time-resolved plume imaging, etch depth vs. fluence measurements, and finite-element temperature-rise calculations presented in this chapter, we have identified a set of mechanisms that explains the data and

supports previous work involving the deposition of polymers by RIR-PLD.

CHAPTER III

MODEL MATERIAL II: POLY(ETHYLENE GLYCOL)

The previous chapter dealt with polystyrene, a material designated to be a simple model for RIR ablation studies. Another polymer that we treat in this way is poly(ethylene glycol) (PEG). This chapter focuses on RIR ablation and deposition of PEG in order to gain insight into ablation mechanisms. One unique benefit of PEG in comparison with PS is that it has a vibrational resonance whose lineshape is dependent upon molecular weight and temperature. Many of the experimental techniques used in chapter II were used here as well, and the results further indicate that spinodal decomposition of a surface layer followed by the recoil-induced expulsion of liquid are the primary mechanisms for material removal.

The chapter begins with an overview of PEG properties followed by the a description of the ablation experiments carried out using PEG as the ablation target. As with polystyrene, multiple laser excitation wavelengths were used in these studies in order to examine the effects of the absorption coefficient on ablation dynamics, and the effects associated with a specific vibrational resonance, if any. This chapter also discusses how molecular weight changes the ablation dynamics by influencing the effective absorption coefficients for different vibrational modes.

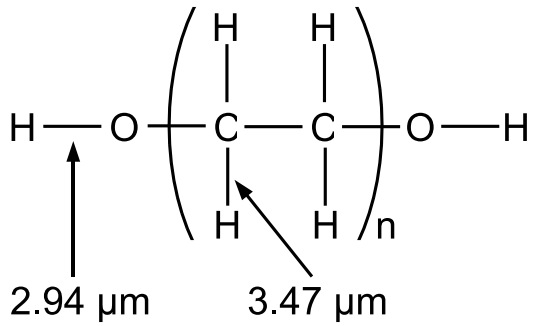

Figure 3.1: The chemical structure of PEG with two vibrational modes labeled.

3.1 PEG overview

Poly(ethylene glycol) (PEG) is a common polymer found in many commercial products. It is commonly used as a food additive and is also an ingredient in many household products such as skin creams, shampoos, and toothpaste. The O-H group at the ends of the polymer chain make it soluble in most alcohols and also in water, and thus it is easily processable.

The chemical structure of PEG is shown in figure 3.1. The structure is the same as that of simple polyethylene which consists only of C-H bonds, except in PEG the ends of the chains are capped with O-H groups. Two of the vibrational resonances are also labeled in figure 3.1, corresponding to the O-H and C-H stretching modes. Since the O-H groups only exist at the ends of the polymer chains, as the degree of polymerization increases the ratio of O-H to C-H bonds decreases, and the effective O-H absorption coefficient decreases. In other words, the O-H absorption coefficient is a function of molecular weight [46]. Therefore, one can effectively tune the O-H absorption coefficient by varying the molecular weight of the PEG.

3.1.1 Temperature-dependence of vibrational bands

A number of authors have pointed out that a temperature-dependent absorption coefficient strongly affects the dynamics of IR laser ablation [47, 48, 49, 17]. In light of this, we have measured the infrared spectrum of PEG (1000 g/mol) as a function of temperature. In figure 3.2, we show the spectral region that includes the O-H and C-H stretching bands at room temperature and 353 K, which is some 40 degrees above the melting temperature of PEG 1000. They are consistent with what has been previously

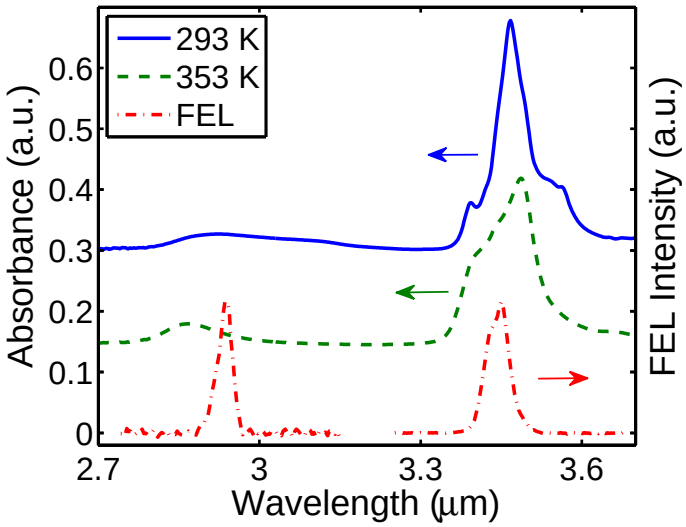

Figure 3.2: PEG absorbance as a function of wavelength in the spectral region that encompasses the C-H and O-H vibrational bands at room temperature and 60 °C. Also shown are the respective spectra of the FEL at wavelengths of 2.94 and 3.45 μm, illustrating the extent of the laser bandwidth overlap with the vibrational modes.

observed for PEG in the molten phase [50]. The O-H absorption band around 2.94 μm is strongly temperature dependent and it blueshifts and narrows as the polymer melts. In contrast, the absorption bands near 3.45 μm due to the C-H stretches

change intensity but not position. Thus, it is expected that as PEG is vaporized, it becomes transparent to the 2.94 μm laser excitation wavelength (also shown in figure 3.2). The infrared spectrum of ethylene glycol in the vapor phase shows a 300 cm^{-1} shift in the OH band in comparison with the liquid [51]. This arises due to the sensitivity of the O-H band to hydrogen bonding interactions. Generally, the higher the degree of association, the longer the wavelength at which the O-H band appears. So when PEG is vaporized, the O-H band shifts out of the bandwidth envelope of the laser and the laser radiation is not attenuated by the plume. In contrast, the C-H stretch will not appreciably change position when the polymer is vaporized and the plume is expected to strongly attenuate the laser when the C-H stretch is excited (3.45 μm).

3.2 Experimental Details

3.2.1 Laser source

The ablation laser used in these experiments was the Vanderbilt free-electron laser (FEL) [31]. For details regarding the FEL, the reader is referred to section 1.4. The wavelengths used for the ablation of PEG were 2.94 μm and 3.45 μm.

3.2.2 Target preparation

Melt-cast targets of PEG were prepared by heating various molecular weights of commercial-grade PEG powder supplied by Sigma-Aldrich in a 2.5-cm diameter stainless steel dies on a hot plate in air at 70 °C; the target well was 2 mm deep. No purification or special preparation of the sample material was undertaken. Each target

was melted and cooled three times in order to facilitate reproducibility. Previous work has shown that this cyclic heating and cooling serves to minimize the presence of air pockets in the target and helps to create a smooth surface that leads to more consistent rates of ablation [46].

3.2.3 Bright-field plume imaging

Time-resolved plume shadowgraphs were taken using the setup displayed in figure 2.3 described in chapter II. Briefly, a nitrogen-pumped dye laser running parallel to the target surface illuminated an area several millimeters above the target surface; a telephoto lens then imaged the silhouette of the target surface onto a color CCD. Time resolution was limited by the excited state lifetime of the fluorescent dye and was determined to be roughly 50 ns by measuring the the temporal profile of the pulse with a fast Si photodiode. An electronic delay generator (Stanford Research Systems DG535) was used to vary the time delay between the pump and probe pulse.

3.2.4 Quartz crystal microbalance

Quantitative measurements of ablation yield were made in vacuum using a quartz crystal microbalance (QCM) deposition-rate monitor (Inficon XTM/2). Fresh targets were conditioned before data acquisition by rastering the laser beam over the surface of the target until it was uniformly textured in order to produce a target surface that was similar for every trial. To measure average single-pulse ablation rates, the laser was scanned over the target for a time interval of 10 seconds and the QCM reading was divided by the number of FEL macropulses delivered in the 10 s interval. For

each laser fluence, this procedure was repeated three times for statistical analysis.

3.3 Experimental Results and Discussion

3.3.1 Plume dynamics

Shadowgraphs of the ablation plume and shockwave are shown for PEG 4000 at 8 and 164 μs after the initiation of the laser pulse for the C-H and O-H excitations in figure 3.3. The results indicate different behavior for ablation exciting the C-H

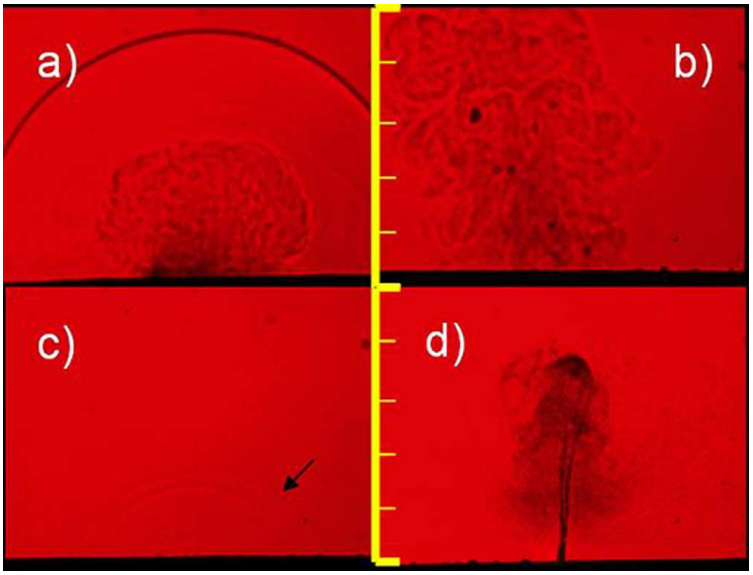

Figure 3.3: Shadowgraphs of PEG target for a) λ = 3.45 μm and 8 μs delay b) same wavelength and 64 μs delay c), d) same delays as above but λ= 2.94 μm. In c) a line is drawn to indicate the leading edge of the shockwave which is faint in the photograph. A 5mm scale is shown.

stretch in comparison with the O-H stretch. In particular, the shock wave moves more quickly for 3.45 μm excitation and the ejecta are distinctly different for the two wavelengths. The laser fluence in both cases was about 7.5 J/cm^2 as calculated by

measuring the laser energy and spot size at the target surface. The primary material ejection appears to be mostly vapor for the early stages of 3.45 μm excitation (figures 3.3a and 3.3b), while at 2.94 μm, a thin jet of polymer, approximately 50-100 μm in diameter, emerges from the target (figure 3.3d).

Exciting the C-H stretch produces an ablation plume that is similar in nature to the polystyrene ablation shown in figure 2.6 in chapter II. A gaseous plume is generated which drives a hemispherical shockwave outward from the target. While the absorption coefficient for the C-H mode of PEG was not measured as precisely as the PS coefficients presented in the previous chapter, we estimate that the penetration depth of this mode is roughly 15-30 μm (α = 666-333 cm^{-1}), making it comparable to the resonant absorption coefficients used for PS ablation. Thus a similar energy density is attained in PEG under excitation of the C-H stretching mode as was attained in the resonant ablation of PS. This explains the similarity of the shadowgraph images between the two materials, and also indicates that the same ablation mechanisms are likely responsible for both materials. More details concerning the ablation mechanisms are discussed below.

The plume generated when the O-H mode is excited (figure 3.3d) is similar to figure 2.7 in the previous chapter where a low fluence is used to ablate PS. These shadowgraphs indicate that a thin jet emerges from the target, and does so only after the laser pulse terminates. While the absorption coefficient for the O-H stretching mode of PEG is roughly 4-5 times lower than that of PS, the fluence used to obtain the shadowgraph in figure 3.3d is approximately four times that used in the low fluence PS ablation shadowgraphs that appear to be similar. Thus, the energy density attained in

each case is similar, hence the similar behavior of the plume. The smaller volumetric energy density causes a weaker jet-like plume since only a small cross section of the laser beam can effectively vaporize the target. The vaporized material is not dense enough to be detected by the imaging apparatus, and all that is seen is the liquid that emerges from recoil force.

To investigate how molecular weight affects plume dynamics, shadowgraphs were taken of different PEG targets of various molecular weights. At 2.94 μm, there was markedly similar behavior in the ejecta - namely a long thin jet was formed that eventually broke apart. As a liquid jet expands into a dense medium such as the liquid PEG expands into the atmosphere, it strives to reduce its surface tension and does so by breaking into smaller droplets. These Plateau-Rayleigh instabilities were also responsible for the appearance of liquid strings redeposited around the periphery of ablation craters in PS. Figure 3.4 shows images of PEG 1450, 4000, and 12,000 g/mol at a fixed time delay of 164 μs and at a laser wavelength of 2.94 μm. In figure 3.4d, a shadowgraph is shown for excitation of the C-H stretch at 3.45 μm and the results are quite different. The plume consists mostly of vapor and it is spread over a much wider area. In the lower portion of the photograph, a particulate is visible. Particulates are quite prominent at high fluence for 3.45 μm ablation and possibly arise from recoil-induced ejection of molten material just above the melting temperature that solidifies upon removal [17]. Since the melting temperature of PEG is some 200 °C lower than that of PS, condensation of the plume from gas or liquid to solid would occur more readily.

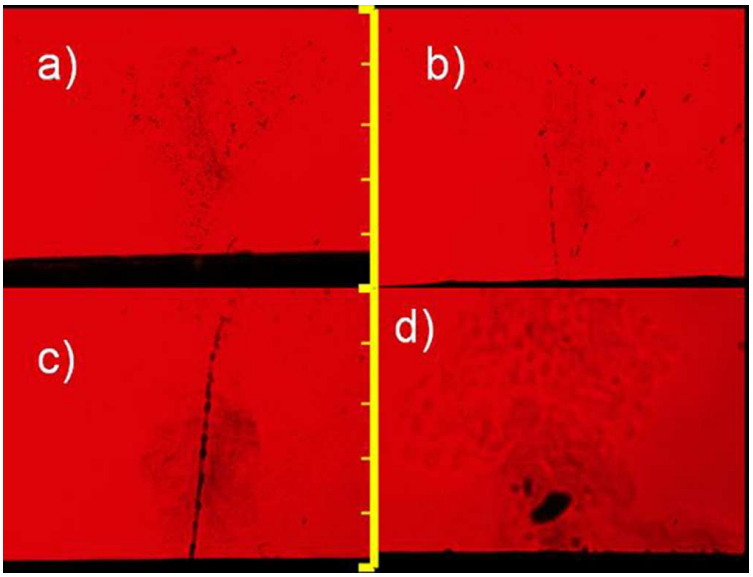

Figure 3.4: Shadowgraphs of PEG targets for a) $\lambda = 2.94$ μm and 164 μs delay (1450 g/mol) b) same wavelength and delay (12000 g/mol) c) same wavelength and delay (4000 g/mol) d) same delay as above but $\lambda = 3.45$ μm. A 5 mm scale is shown.

3.3.2 Shockwave trajectories

The trajectories of the shock waves are displayed in figure 3.5. For 2.94 μm excitation, the blast wave appears to be initially well fit by Taylor's model which predicts $t^{2/5}$ scaling of the radius of the shock wave [52, 53]. Taylor's model was developed to determine the energy released in atomic bombs, and assumes a localized point source explosion that generates a spherical blast wave into the surrounding medium. After 9-10 μs, when ejection of a large amount of material accelerates the shock wave, the scaling becomes linear in time, thus becoming consistent with Freiwald's approximation when large amounts of mass are removed [54].

The shockwave data are consistent with what is seen in the shadowgraphs - namely, that mass material removal begins very early in the laser pulse for 3.45 μm irradiation, and that there is approximately an 8 μs delay before ejection when using 2.94 μm

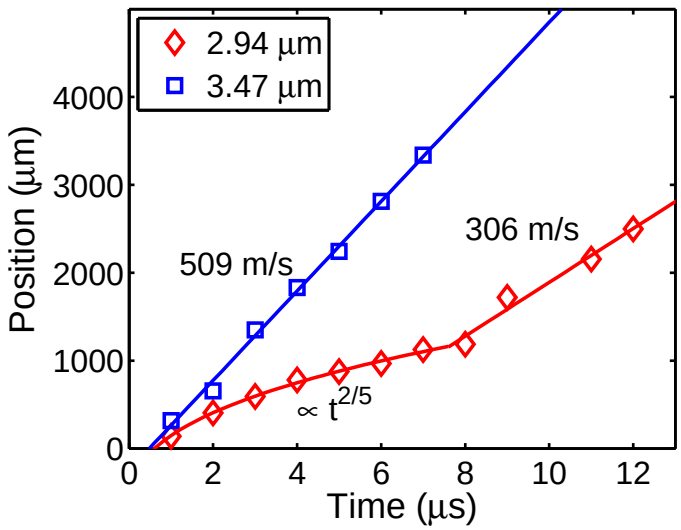

Figure 3.5: Shockwave front positions as a function of time for ablation of PEG 4000 at the O-H and C-H vibrational resonances.

irradiation. Assuming that resonant IR ablation is a thermally activated process, the smaller absorption coefficient for this mode means a smaller volumetric energy density and thus a longer time before some temperature is reached that is sufficient enough to induce material expulsion. Since the C-H mode has a larger absorption coefficient than the O-H mode, it reaches this activation temperature soon within the laser pulse and consequently material removal happens on the order of several microseconds.

3.3.3 Ablation rate measurements and comparison to heuristic models

The ablation rate was measured for PEG of molecular weights 1450, 10,000 and 35,000 g/mol. These molecular weights span the range for which the O-H absorption coefficient is moderate to weak (100-10 cm^{-1}). In contrast, the C-H absorption coefficient is not expected to change appreciably [55]. Interestingly, at room temperature the only thermodynamic parameter of PEG that changes appreciably in this molec-

ular weight range is the melting temperature, while the heat capacity, enthalpy of vaporization, and thermal conductivity all remain relatively constant [56, 46]. Therefore, we can simultaneously investigate the effect of increasing molecular weight for a constant wavelength (and absorption coefficient) and moving from resonant to effectively non-resonant ablation as well. The deposition rates for excitation at 3.45 μm are all similar, and appear to lie along a universal curve as shown in figure 3.6. The QCM was not calibrated for these experiments, hence the units are arbitrary. At

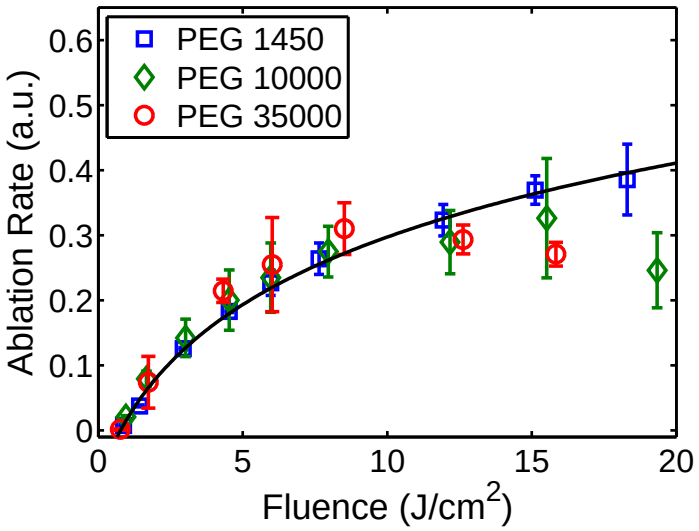

Figure 3.6: Ablation rate as a function of fluence for various molecular weights of PEG ablated at $\lambda = 3.45$ μm. The line is a fit of all data to equation 3.1.

higher fluences, the error bars (standard deviation of three measurements) become large and the deposition rate appears to fall with increasing fluence. We interpret this as a loss of sensitivity in the QCM rather than an actual decrease in the deposition rate; this loss occurs as solid particles are ejected at high fluence as in figure 3.3d.

These data are reasonably well fit by a heuristic ablation model described in chapter I [17]:

$$\delta = \frac{1}{\alpha\gamma} ln \left[\gamma \left(\frac{\Phi_0}{\Phi_{th}} - 1 \right) + 1 \right] \tag{3.1}$$

where δ is the ablation rate, α is the absorption coefficient, γ is the plume shielding factor, Φ_0 is the laser fluence, and Φ_{th} is the threshold fluence for ablation. Extracted values of γ from the fits are of order 0.3, which suggests that plume shielding is moderate to strong for ablation *via* the C-H mode. Given that the absorption profile at this wavelength does not shift out of resonance from the laser as it is heated, these values of γ are in agreement with the shadowgraph images which depict ablation at 3.45 μm beginning well within the time frame of the laser pulse and therefore undoubtedly shielding the remainder of the pulse.

The ablation rate data for $\lambda = 2.94$ μm, as shown in figure 3.7, are not well fit by this model. It should be noted that data at this wavelength were only collected for the lowest molecular weight PEG used in this study (PEG 1450) because of the small absorption coefficient at higher molecular weights that greatly limited the ablation rate. For the low molecular weight PEG though, instead of a logarithmic saturation of the ablation rate with increasing fluence, the data show an approximately linear increase with fluence up to around 12 J/cm^2, at which point the rate drastically increases. Interestingly enough, this same behavior was observed for ablation of PEG by a free-running Er:YAG laser operating at 2.94 μm with a pulse length of 350 μs [46]. Due to the long laser pulse used in that work, the data were described as conforming to a steady state model with a variable ablation enthalpy. Since material removal is

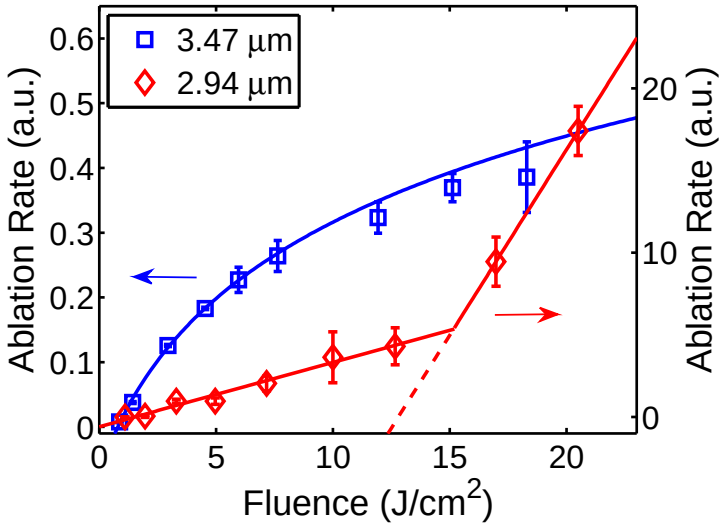

Figure 3.7: Ablation rate as a function of fluence for excitation of PEG 1450 at the C-H stretch (3.45 μm) and the O-H stretch (2.94 μm). The line through the C-H data points is a fit to equation 3.1, and the two linear fits drawn through the O-H data points serve to guide the eye and to estimate the apparent threshold of a second thermally-activated process.

not concurrent with the laser pulse for ablation at the O-H mode as evidenced by the shadowgraphs, it would be incorrect to designate the ablation as steady state. What is more likely is that a different mechanism is responsible for ablation at the lower fluences due to the small absorption coefficient for this mode. Temperature-rise calculations presented in section 3.4 show that the kink in figure 3.7 for the O-H mode ablation is located at a fluence where phase explosion is likely to become the dominant mechanism, helping to explain dramatic increase in deposition rate.

3.4 Temperature rise calculations

In accounting for the ejection of polymeric material from the target following resonant IR excitation, we again consider the thermal confinement time, given by

$$\tau_{th} = \frac{c_p \rho}{\alpha^2 \kappa} \tag{3.2}$$

For 3.45 μm excitation, $\tau_{th} \sim$ 1-10 ms, and for excitation via the O-H vibrational of PEG, $\tau_{th} \sim$ 0.1-10 s. This means that that both the 4 μs FEL pulse and a 350 μs long Er:YAG pulse (at 2.94 μm) as used in reference [46] are thermally confined. Thus, in estimating a temperature rise over the laser focal volume, thermal diffusion can be neglected and following the same line of reasoning from section 2.3.4, we may again write

$$T = T_i + \frac{2\alpha\Phi}{\rho c_p} \exp\left(-2\frac{x^2+y^2}{w^2} - \alpha z\right) \tag{3.3}$$

Using an approximate threshold fluence of $\Phi = 2$ J/cm^2, $c_p = 2.2$ J/g/^{o}C, $\rho = 1.2$ g/cm^3, and $\alpha_{3.45} \sim 350$ cm^{-1}, then the maximum surface temperature reached approaches 900 °C, as shown in figure 3.8. Previous work has measured the spontaneous "boiling-up" temperature for PEG to be on the order of 1000 °C similar to that of PS [20, 21]. As explained in chapter II, this is the effective spinodal decomposition temperature. Thus, at this temperature, polymer chains longer than some critical chain length (believed to be $\sim$ 1000 Da [19]), decompose and are then able to escape into the gas phase via homogeneous bubble nucleation. Referring back to figures 3.3 and 3.4, ablation at 3.45 μm produces what appears to be gaseous products, which

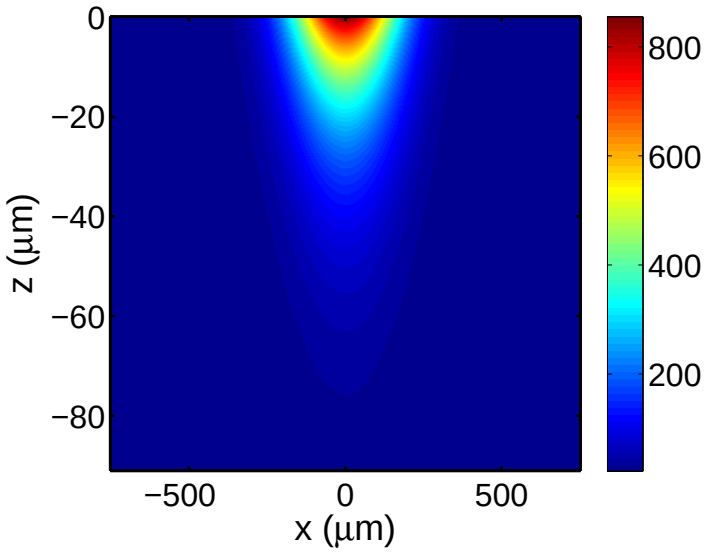

Figure 3.8: Laser-induced temperature rise as a function of x and y in PEG for excitation of the C-H stretching mode near the ablation threshold

is understandable through the calculated temperature rise.

Using the same parameters as above but with a lower absorption coefficient of $\alpha_{2.94} \sim 150$ cm^{-1}, the maximum laser-induced temperature at the surface of the target is only 250 °C. Thus, the entire focal volume is melted ($T_m = 60$ °C), but not hot enough to undergo spinodal decomposition. For such a weakly absorbing mode at low fluence then, some other hydrodynamic effect such as surface-tension-driven-flow must be responsible for material ejection [57]. Once the fluence is increased to 12 J/cm^2, the point at which ablation appears to be dominated by a second mechanism in figure 3.7, then the calculated temperature at the surface of the target is well over 1000 °C and the recoil pressure produced by spinodal decomposition of the surface dramatically increases the ablation rate.

Since the plume generated by 2.94 μm irradiation is transparent to the remainder

of the incident pulse, it is no surprise that the ablation rate data as shown in figure 3.7 are similar to those shown in reference [46] where a 350 μs-long Er:YAG pulse was used for ablation. Since both laser pulses are thermally confined, even though one is 100 times more intense than the other, the ablation mechanism is the same provided that the photon absorption is linear in both cases since a given fluence would induce the same temperature rise. Even if Er:YAG ablation exhibits a more steady-state character, the transparency of the plume means that the same amount of material would be removed for a given fluence as the FEL since the laser energy incident at and above the target surface is not absorbed by the plume.

3.5 Conclusions

Resonant-infrared laser ablation of PEG has been studied for two different wavelengths of excitation. For ablation at the C-H stretching mode ($\lambda = 3.45$ μm), time-resolved plume imaging shows that the ejecta are mostly gaseous products that begin to leave the surface fairly early within the time frame of the laser pulse. Since the absorption coefficient as a function of temperature does not change appreciably for this mode, the plume serves to effectively shield the incident laser pulse and decrease the energy absorbed into the target. Static temperature calculations show that the temperatures reached are on the order of 1000 K, which is enough to induce spinodal decomposition and is likely the primary mechanism for material ejection.

For ablation via absorption into the O-H terminal group of the polymer chains, material removal does not begin for some microseconds after the laser pulse is over and tends to be more hydrodynamic in nature. Due to the weaker absorption at

this mode, expected temperature rises are enough to melt the focal volume but not enough to vaporize the entire volume. It is likely that at approximately 12 J/cm^2, a thin surface layer that is hot enough to undergo spinodal decomposition and impart enough momentum to the molten layer to abet ejection and dramatically increase the ablation rate. It is important to note that this conclusion is consistent with previous work which showed that thermal decomposition is the primary mechanism for IR polymer ablation, and that a local temperature rise on the order of those calculated in this work are necessary to achieve ablation [58].

CHAPTER IV

RIR LASER ABLATION AND DEPOSITION OF PEDOT:PSS

Chapters II and III were focused on two model polymer systems that served to further our understanding of the fundamental mechanisms governing infrared laser ablation. The discussion of applications was limited, since neither of these polymers is particularly important to the technological community (although PEG does have drug-delivery applications within the biomedical field [59, 60]). That is not to say that they are in general unimportant; in fact they are ubiquitous in modern society and one probably encounters these polymers everyday. The previous two chapters were intended to elucidate the physics of the IR ablation process, while this chapter and the next deal more directly with applications of RIR-PLD relevant to the microelectronics and display industries.

In addition to dealing with more application-oriented experiments, the work contained in these next two chapters also offers the added dimension of preserving specific polymer functionality, while the previous two chapters did not. Since the materials to be discussed have specific properties (*e.g.* electroluminescence, electrical conductivity) whose functionality is inextricably linked to micro- and macroscopic structure, they require an extra degree of characterization following ablation and deposition that does give some insight into the physics of the ablation process.

In this chapter we report on the vacuum deposition of PEDOT:PSS, a commercially available conducting polymer. Due in part to the expense and in part to the

manufacturing process of the polymer, all depositions are done using a RIR-MAPLE technique where a frozen matrix of the material is ablated rather than bulk polymer melts or pressed targets. The complexity of the RIR-MAPLE process and the chemistry involved will become evident as we show that secondary co-matrices are required in order to grow conducting polymer films. We also examine the effect of laser wavelength and pulse structure on deposited film properties, and discuss the implications this has on the mechanisms of ablation.

This chapter was published in part in Applied Surface Science [37] and in two full-length conference proceedings [38, 61].

4.1 PEDOT:PSS Overview

Conducting polymers have many potential applications in electronics and optoelectronics [62]. For example, they can be incorporated into polymer thin-film transistors, polymer light-emitting diodes (PLEDs) [63], and products and manufacturing processes that benefit from the use of anti-static coatings. One conducting polymer that has recently become widely used is poly(3,4-ethylenedioxy-thiophene):poly(styrenesulfonate) (PEDOT:PSS). PEDOT, the conducting component of the blend, is polymerized with the counter ion PSS to yield a conductive, water-soluble polymer that is nearly transparent in thin film form [64] and can be spin-coated to make well-characterized thin films. The conductivity of the blend can be tuned from 10^{-5} to 600 S/cm making it attractive for many different applications (for perspective, the conducitivity of bulk Cu is 6×10^{7} S/cm) [65]. When deposited as a buffer layer between ITO and an organic light emitter, PEDOT:PSS

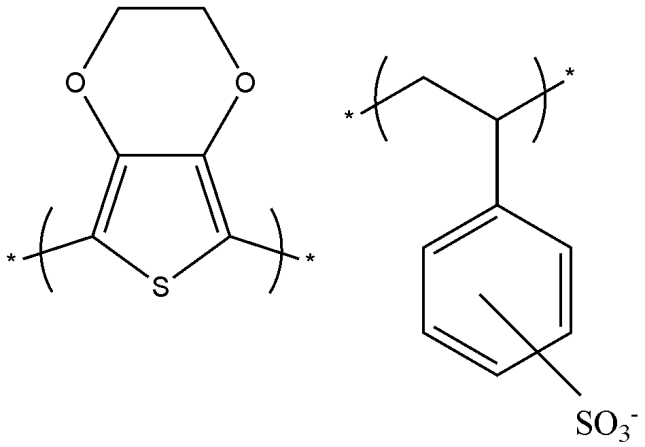

Figure 4.1: Chemical structure of PEDOT:PSS. The PEDOT monomer is shown on the left and the PSS monomer on the right (stars indicate the common bond shared between monomers along the polymer chain).

is an ideal hole-transport layer for PLEDs [66, 67, 68]. The chemical structure of PEDOT:PSS is shown in Figure 4.1. PEDOT:PSS is marketed under the trade name Baytron® by H. C. Starck, and has become one of the most commercially successful conducting polymers [64].

4.1.1 Technological importance

One important application for PEDOT:PSS is in antistatic coatings. Perhaps its most common use is in coating photographic film sheets to avoid electrical charge buildup and the subsequent electrical discharge, which causes a flash and exposes the film. A thin layer of PEDOT:PSS deposited onto the film sheets before they are spun onto reels ensures that no charge accretes. The PEDOT:PSS layer is thin enough such that it has an optical density of < 0.01, and thus the film can still be exposed by normal levels of light. The success of this process has led to the yearly

production of multi-ton batches of PEDOT:PSS, and it is estimated that more than 100 million square meters of photographic film are coated every year [64]. PEDOT is also commonly polymerized on the surface of cathode ray tubes used in television screens to prevent static buildup and dust attraction [69, 65].

Another important application of PEDOT:PSS is in the fabrication of organic small-molecule and polymer light emitting diodes (OLEDs and PLEDs). The typical PLED consists of a light-emitting polymer (LEP) that is sandwiched between a cathode and and anode. When PEDOT:PSS is deposited as a thin layer ($\sim$ 50 nm) between the LEP and the anode as shown in figure 4.2, it acts a buffer layer that facilitates hole transport into the emitting layer and increases device efficiency [66, 67, 68]. Due to the success of PEDOT:PSS as a hole-transport layer, it is now uncommon to see OLEDs or PLEDs fabricated without this essential layer in the device structure.

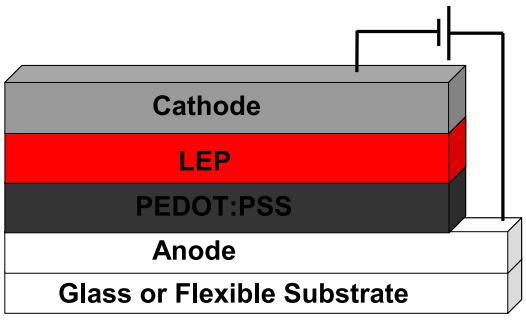

Figure 4.2: Schematic diagram of a PLED with PEDOT:PSS incorporated as a hole-transport layer.

4.1.2 Microscale structure

The microscale structure of PEDOT:PSS plays a central role in the conductive mechanisms of the material and thus warrants some description. As mentioned above, PEDOT is the conducting component of the blend, and it is polymerized with the counter ion PSS in order to render it water soluble. Otherwise, the only method of PEDOT film deposition would be *in-situ* polymerization on a planar surface, as PEDOT by itself is not soluble. In the bulk solution, PEDOT:PSS is a macromolecular salt held together by relatively strong ionic bonds [69, 70]. It has a granular structure with hydrophilic PSS surrounding the PEDOT chains [71, 72, 73]. Since PSS is an insulator, this micellular morphology decreases film conductivity because the conducting PEDOT grains are not in good electrical contact and electrical transport must take place by localized hopping between PEDOT grains. The advantage of being solution processable outweighs the decrease in conductivity, however, and this has therefore become the standard way of manufacturing a PEDOT-based product. The granular structure of the PEDOT:PSS complex will be important in a later section regarding the effects of laser ablation on the conductivity of deposited PEDOT:PSS films.

4.1.3 Current deposition techniques

As outlined above, PEDOT:PSS has numerous technological applications. In light of this, a description of the current deposition techniques is presented here with some key advantages and disadvantages associated with the various processes.

Since polymers are too labile to be thermally evaporated intact [19], most processing is done by liquid-phase techniques, such as spin coating or ink jet printing. Spin coating is attractive due to its simplicity, but is suitable for only the simplest devices, such as single-color PLEDs with one or two organic layers. Multicolor pixelated PLEDs generally require deposition of multiple layers on patterned substrates and this is not easily done using spin coating, although it has been reported using specially synthesized light emitting polymers with photoresist properties [74].

Ink-jet printing enables patterning of substrates, but also has a number of disadvantages. For example, it relies on the hydrofluidic motion of polymer solution through small nozzles; hence it is restricted to solutions of low viscosity [75]. Moreover, thermal ink-jet printing of PEDOT:PSS on ITO can take up to ten successive depositions in order to obtain a continuous film, resulting in uneven film morphologies with thicknesses of up to 800 nm [76], whereas the desirable thicknesses for PLEDs are closer to 50 nm. A vapor-phase deposition technique that would allow for efficient patterning of substrates and conformal coatings would be a useful tool that could be complimentary to existing deposition techniques.

As explained in chapter I, RIR-PLD has proved to be a useful method for polymer thin-film deposition. Given that the polymer is manufactured as a $\sim 1\%$ by weight solution in H_2O, it can easily be incorporated into an RIR-MAPLE deposition process.

4.2 RIR laser deposition of PEDOT:PSS thin-films

PEDOT:PSS thin-films were deposited using the RIR-MAPLE protocol discussed in section 1.3.2. Typical deposition times were 5-20 minutes and, depending on laser

fluence, yielded film thicknesses of 50-250 nm.

PEDOT:PSS from H. C. Starck (Baytron® P) was received as a 1.3% by weight dispersion in H_2O. Using this particular solution, we measured the conductivity of spin-coated films to be 0.1 Ω/cm^2, in close agreement with the manufacturer's specifications.

The native solvent of PEDOT:PSS is water, which has only one strong characteristic absorption in the mid-IR region corresponding to the O-H stretch at 3 μm. The resonant O-H mode frequency does have some temperature dependence, and tends to red-shift and increase in intensity as the temperature decreases and the water crystallizes [77, 78]. This particular resonance mode has a relatively broad linewidth (FWHM of ~ 0.5 μm) so that any excitation wavelength near 3 μm can be considered to be resonant excitation. Thus depositions were carried out by using a solid state erbium-doped yttrium aluminum garnet (Er:YAG) laser operating at 2.94 μm and a tunable FEL operating at 3.05 μm.

To enhance the electrical conductivity of the deposited films, and to increase the number of resonant vibrational modes available for RIR ablation, a secondary solvent was doped into the native PEDOT:PSS/water solution for some depositions. *N*-methyl-2-pyrrolidinone (NMP), a solvent with known conductivity-enhancing effects in PEDOT:PSS films [79], was doped into the PEDOT:PSS/water solution at concentrations up to 25% by weight before freezing. Figure 4.3 shows IR absorbance spectra of water and NMP with the resonant absorption modes labeled.

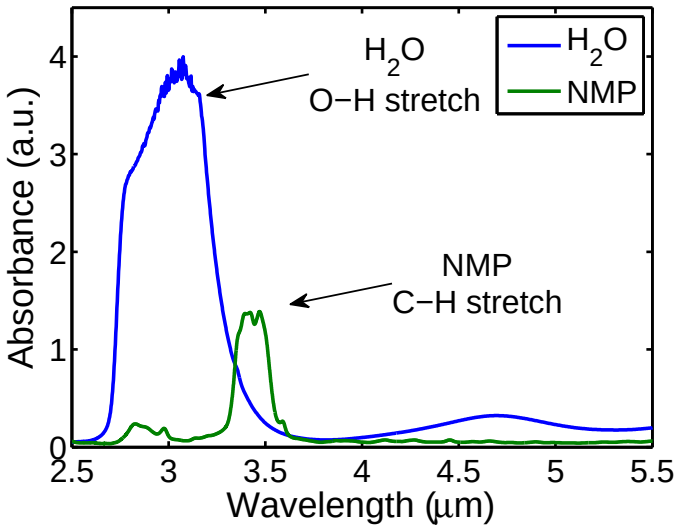

Figure 4.3: FTIR spectra of H_2O and NMP around 3 μm.

4.2.1 Light Sources

The primary laser source used in these experiments was a modified Mark III free-electron laser (FEL) located at Vanderbilt University [31]. The parameters of the FEL have been fully described in section 1.4, and thus will not be described here. In these experiments the FEL was tuned to 3.05 μm or 3.47 μm for the PEDOT:PSS depositions (O-H or C-H stretching modes of the matrix, respectively).

An Er:YAG laser operating at 2.94 μm was also used for PEDOT:PSS film deposition to investigate how laser pulse structure affects the deposited film. Given the width of the O-H absorption peak of water-ice (the primary matrix for the PEDOT:PSS depositions) at 3 μm, the Er:YAG's output wavelength of 2.94 μm is well within the vibrational resonance of the matrix. It is well known that the O-H vibrational mode is temperature dependent because the hydrogen atoms also participate

in hydrogen bonding [77, 78], but as water-ice is melted the 2.94 μm output of the Er:YAG remains resonant with this stretching mode. The laser was operated in a "free-running" mode, that is to say that it was not Q-switched and had a pulse width of $\sim$ 350 μs at a repetition rate of 2 Hz. Typical fluences used for a single macropulse were 5-10 J/cm^2.

4.2.2 Laser-deposited PEDOT:PSS film properties

Here we describe the results obtained from analyzing the relevant properties of the laser-deposited films. Fourier-transform infrared (FTIR) spectra were acquired with a Bruker IFS 66v FTIR spectrometer, and conductivity measurements were taken using a MMR technologies H-50 Van der Pauw four-point probe system [80].

As a first step in analyzing the laser-deposited PEDOT:PSS films, FTIR spectroscopy was performed. As shown in figure 4.4, the FTIR spectra of the deposited films are very similar in nature to the spectrum of a spin-coated film. This suggests that the covalent bonding structure that serves as the polymer's "molecular fingerprint" is not disrupted by the laser transfer process. As we will see momentarily, however, this is not necessarily an appropriate measure of the functionality of the polymer film. Properties such as molecular weight, chain configuration, and hydrogen and ionic bonding structure do not influence FTIR spectra but still have a role in determining the material properties.

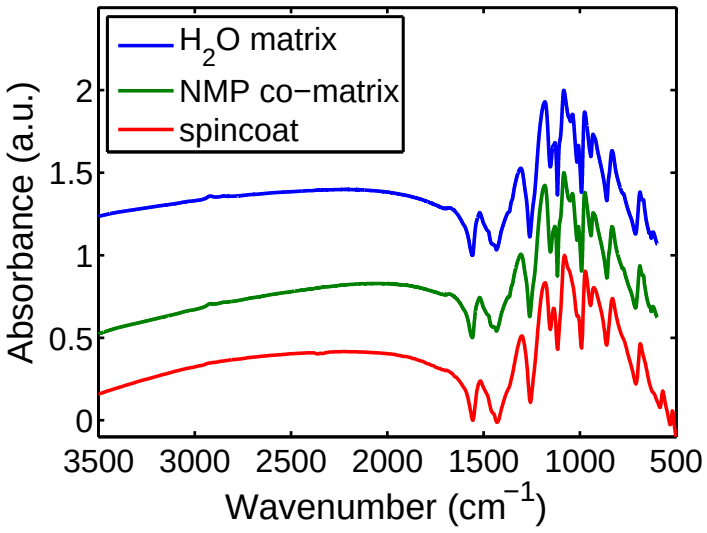

Figure 4.4: FTIR spectra of PEDOT:PSS films deposited under different conditions.

4.2.2.1 Wavelength and solvent effects

To examine the electronic structure of the PEDOT:PSS films, electrical conductivity was measured for films deposited with different excitation laser conditions. The results of the conductivity measurements are displayed in Table IV.1. Although PEDOT:PSS films deposited from a native water matrix at a laser wavelength of 3.05 μm have conductivities lower than the measurable limit of our four-point probe setup, adding even trace amounts of NMP to the solution prior to freezing results in the deposition of a conducting film, regardless of the wavelength used (3.05 or 3.47 μm).

The presence of conductivity only in films whose target matrices were doped with NMP is an interesting observation and is likely the result of chemical modifications of the PEDOT:PSS complex at the microscopic scale. The mechanism of PEDOT:PSS conductivity enhancement due to the addition of various organic solvents is known,

Table IV.1: Summary of PEDOT:PSS conductivities deposited from different co-matrices and with different wavelengths using the FEL.

Matrix Composition	**Excitation Wavelength (μm)**	**Conductivity (S/cm)**
100% H_2O	Spin Coat	0.08 ± 0.05
100% H_2O	3.05	0.0
10% NMP, 90% H_2O	3.05	0.03 ± 0.02
10% NMP, 90% H_2O	3.47	0.18 ± 0.02
50% NMP, 50% H_2O	3.05	0.12 ± 0.09
50% NMP, 50% H_2O	3.47	0.21 ± 0.09

but not well understood. It is believed, however, that the role of the NMP is to phase-separate the insulating PSS from the conducting PEDOT chains [71, 72, 73]. The microscale morphology of PEDOT:PSS consists of individual grains of PEDOT (typically 1-10 μm in size), the conducting component of the blend, surrounded by a thin shell of ionically bound PSS whose role is to stabilize the PEDOT and allow it to be suspended in water [81]. The PSS shell (on the order of several $\mathring{A}$ thick), while allowing the complex to be solution processed, hinders macroscopic film conductivity since electrons must hop from one PEDOT grain to another. Thus, removal of the PSS shell via the addition of an organic co-matrix can lead to orders of magnitude increases in film conductivity [79]. We believe that a similar mechanism is involved in the IR laser ablation process. With no NMP in the frozen solution, as polymer and solvent molecules are liberated by the incoming laser pulse, free PSS and PEDOT molecules may recombine in such a way so as to increase the thickness of the original PSS shell, resulting in a loss of electrical conductivity. If NMP is present in the target solution, however, the PSS is phase-separated from the beginning and is less likely to combine with PEDOT molecules in the plume on its way to the target.

Another possibility for the loss of conductivity when pure water is used as the matrix is thermal decomposition of the PEDOT and disruption of the π-conjugation responsible for electrical conductivity. Recall that laser-induced temperature calculations presented in chapters II and III exceeded 1000 °C at the target surface. The polymers used in those chapters had optical penetration depths of tens of μm, while the penetration depth of water-ice is only 400 nm [77, 78]. The smaller penetration depth means that the volumetric energy density is higher for a given fluence, and the

temperatures reached at the surface of the PEDOT:PSS targets may therefore reach temperatures high enough to fragment the PEDOT backbone when pure water is used as the ablation matrix. This would not necessarily be evident in FTIR spectra, but would destroy the π-conjugation that is responsible for electral conductivity.

Note that doping NMP into the solution effectively dilutes the amount of water in the target so that when the O-H mode is excited, it is with a smaller absorption coefficient. When the C-H stretch of the NMP is excited, the absorption coefficient is again smaller as is obvious from figure 4.3. In either case, the smaller absorption coefficient would mean less energy density in the target and a lower temperature for a given fluence. This could help explain why the conductivity survives when PEDOT:PSS is deposited under these conditions.

4.2.2.2 Pulse structure effects on surface roughness

The effect of laser pulse structure on film surface morphology was also investigated for different frozen solutions of PEDOT:PSS. Scanning-electron micrographs are displayed in figure 4.5 and show films deposited by excitation of the O-H stretching resonance of the water matrix (2.94 - 3.05 μm). The left column of images shows films deposited using the 4 μs pulse of the FEL, and the right column corresponds to ablation from the 350 μs long pulse of the Er:YAG (2.94 μm). NMP concentration increases from 0-25% from top to bottom. It is evident that, in general, the films deposited with the longer pulse length appear rougher than those deposited with the FEL.

As NMP concentration is increased the presence of white granular patches become

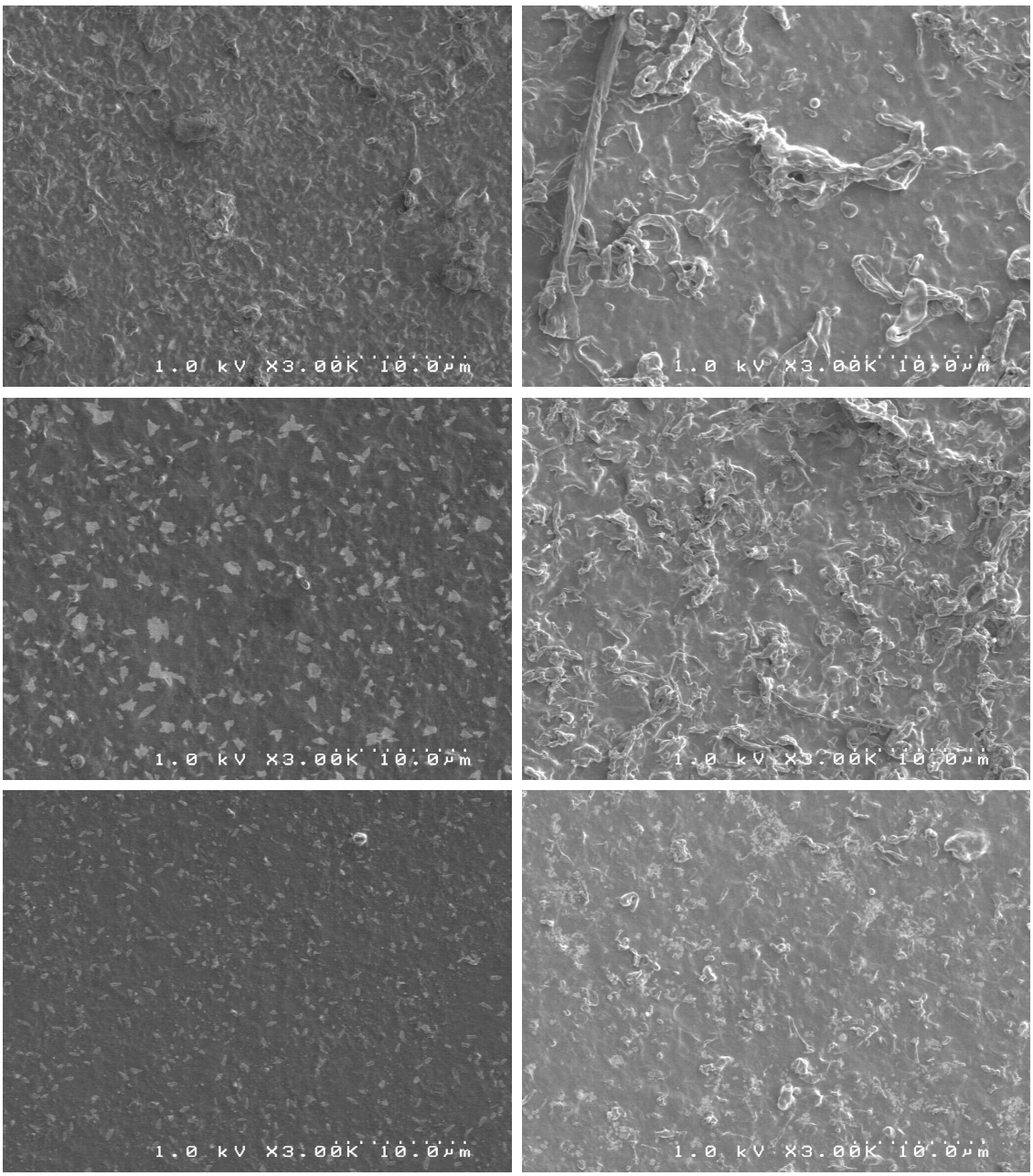

Figure 4.5: SEM images PEDOT:PSS films deposited by exciting the O-H stretching mode of water. Left column: FEL deposited, right column: Er:YAG deposited. From top to bottom, NMP concentration = 0%, 10%, and 25%. The scale bar for each reads 10 μm.

more visible in the SEM images. Consistent with the explanation above, it is likely that these white patches are actually regions of insulating PSS that have phase-segregated allowing for the conductive PEDOT networks to form. However, it is still unclear at this point how the increase of NMP serves to improve the roughness of the deposited film. Previous work with RIR-MAPLE of semiconducting polymers has indicated that solvent properties such as viscosity have a strong effect on film morphology, but in a non-trivial way [39]. It is possible that with NMP present in the solvent mixture prior to ablation, the physical and thermal properties of the target are more conducive to going into a molecular vapor phase during ablation rather than forming liquid jets or droplets (the viscosity of NMP at room temperature is 1.7 cp, compared to 1.0 for water). The mechanism responsible for solvent effects on surface roughness, however, remain as one of the puzzles of RIR-MAPLE. Figure 4.6 displays the roughness of each film as measured with a stylus profilometer (Veeco Dektak 150) and quantifies the increase in roughness with the longer pulse width and decreasing NMP concentration.

One difference between the FEL depositions and the Er:YAG depositions besides the pulse structure of the lasers was the focal spot sizes used in either case. The spot size of the FEL beam in these experiments was anywhere from 100-200 μm, while that of the Er:YAG was a much larger 1-2 mm due to the poor quality of the spatial mode of the beam. To investigate the dependence of film surface quality on spot size, RMS surface roughness was measured on PEDOT:PSS films ablated from a plain water matrix using the FEL at 3.05 μm for different focal spot sizes. The results are displayed in figure 4.7. The depositions were done by fixing the beam energy at 5,

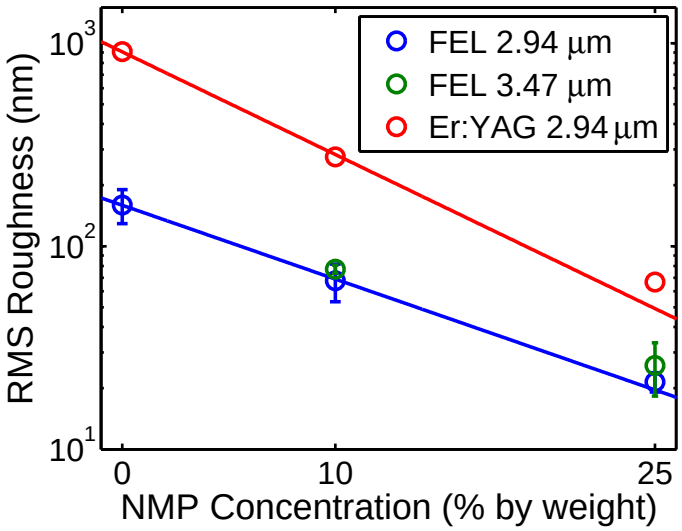

Figure 4.6: Surface roughness of PEDOT:PSS films as a function of NMP deposited using different matrix concentrations and laser parameters.

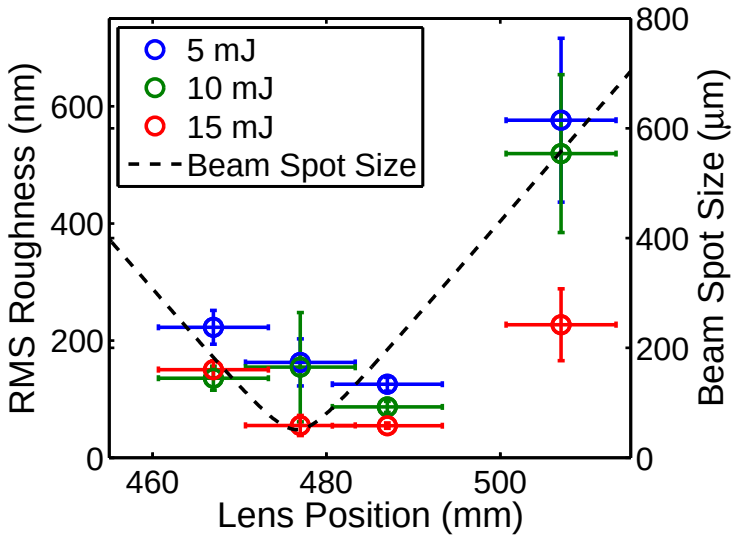

Figure 4.7: Surface roughness of PEDOT:PSS films as a function of laser focus deposited with the FEL ($\lambda = 3.05$ μm). The spot size curve for the 500 mm focal length lens corresponds to the right axis.

10, or 15 mJ, and varying the distance between the focal lens and the target surface (the large x-error bars come from the fact that the laser was continuously scanning across the target surface). The beam spot size (radius), which was measured by the knife-edge method at various lens-target distances, was fit to a theoretical gaussian beam propagation curve and is shown in the figure as the dashed line corresponding to the right axis. It is clear from the data that the film RMS roughness tracks the laser spot size and is inversely proportional to beam energy. Thus, a higher fluence yields a smoother film. Recall from chapter II that with higher fluences, ablation is initiated sooner. It is possible that since the plume is exposed to the laser for a longer period of time in this case, the laser absorption in the plume serves to further heat and disassociate liquid droplets into smaller ones. The maximum focal spot size used for film growth in figure 4.7 was 550 μm. Unfortunately, due to the amount of energy available in a single pulse of the FEL, the spot size could not be expanded further while still achieving ablation. However, if the data are extrapolated to spot sizes comparable with those used in the Er:YAG ablation, we would expect to see RMS roughness values on the order of 1000 nm, consistent with the results in figure 4.6 for Er:YAG ablation.

4.3 Discussion

When considering pulse structure effects, it is useful to again examine the thermal confinement time,

$$\tau_{th} = \frac{c_p \rho}{\alpha^2 \kappa} \tag{4.1}$$

Table IV.2 lists the relevant thermal properties of water in the solid and liquid states, along with the corresponding thermal diffusion times. Note that for water ablation, neither the FEL nor the Er:YAG pulses are thermally confined as they were for ablation of solid polymer targets in chapters II and III. Since neither laser pulse is thermally confined, it is unlikely that the difference in pulse length causes the dramatic differences in deposited film surfaces seen between the two lasers. It seems that instead, the spatial differences in the two beams causes the different film properties.

Theoretical work aimed at explaining the "deflated balloon" morphological structures of laser deposited MAPLE films such as those seen in figure 4.5 points toward spinodal decomposition as being the dominant mechanism of ablation, as well as the cause for the rough surface features [83, 84]. Moreover, previous studies on IR ablation of water showed that phase explosion followed by recoil-induced ejection of liquid were the dominant mechanisms of ablation [23, 22, 85]. Given that the native PEDOT:PSS solution is roughly 99 % water, the same mechanism likely applies in this case. In other work, shadowgraphy of RIR ablation of NMP even shows liquid jets erupting from the target surface after laser absorption [86]. Since the majority

Table IV.2: Thermal properties of H_2O in the solid and liquid states [82]. Solid-state data are for a temperature of 80 K and liquid-state data are for temperatures just above the freezing point.

	α^{-1} (μm) [77, 78]	c_p (J/(°K·g))	ρ (g/cm^3)	κ (W/(°K·cm))	$\boldsymbol{\tau_{th}}$ (s)
Solid	0.40	0.69	0.92	0.07	1.5x10^{-8}
Liquid	0.77	2.16	0.99	0.03	4.2x10^{-7}

of ablated material erupts from the target in liquid form, liquid instabilities such as those discussed in chapters II and III can cause jets and droplets to form in the plume. The Er:YAG's larger spot size would ablate a larger volume of liquid and thus implicate larger droplets and jets in the plume. The larger droplets lead to the deposition of larger surface features on the substrate which explains the SEM images in figure 4.5 and the surface roughness data in figure 4.6.

4.4 Conclusions

Thin films of PEDOT:PSS have been grown by RIR-MAPLE using lasers with different resonant wavelengths and temporal pulse structures. The addition of a co-matrix is needed in order to preserve the conductivity of the polymer film, and we attribute the success in this case to pre-ablative chemistry that occurs in the target. The laser-induced temperature-rise calculations presented in chapters II and III demonstrated that temperatures within the focal spot of the laser may reach values on the order of 1000 °C for resonant IR ablation, so it is certainly plausible that thermal effects may be responsible for the absence of electrical conductivity in films deposited without a co-matrix.

It appears that far beyond the thermal confinement regime, the laser pulse structure is not as important in determining film surface properties as is the laser focal spot size. Laser pulses that span into the microsecond regime likely heat the target surface under near equilibrium conditions and the hydrodynamic events that follow lead to the ejection of large droplets and jets whose size is proportional to the focal volume. This is consistent with the idea of recoil-induced ejection (powered by a

phase explosion) since most of the focal volume would be expelled as liquid, giving rise to rough surface features.

CHAPTER V

MEH-PPV DEPOSITION AND PLED FABRICATION

The previous chapter discussed the deposition of PEDOT:PSS, a popular hole-transport layer used in PLEDs, and thus helped to provide motivation and reason for this chapter which is focused on the IR laser fabrication of PLEDs. In 2004, RIR laser transfer of MEH-PPV was successfully demonstrated using the Vanderbilt FEL [87]. In that work, deposited films exhibited photoluminescence, demonstrating that the conjugation and the π-π^* bandgap was preserved (though possibly somewhat altered as indicated by a slight spectral shift) through deposition. However, whether or not the polymer film would *electroluminesce* when placed in a device structure was not tested. The remainder of this chapter presents original research involving RIR laser deposition of MEH-PPV and PLED device fabrication.

Conjugated polymers exhibit properties which are very sensitive to their chemical structure. Disrupting the π-bonding network that gives rise to their conducting and semi-conducting properties can change the functionality of the polymer that defines it. By measuring these properties before and after laser ablation and deposition, then, we can directly observe whether or not the delocalized π-bonded network remains intact.

This chapter was published in part in the Journal of Laser Micro/Nanoengineering [88] and in two full-length conference proceedings [39, 89].

5.1 Light-Emitting Polymers

Over the last several decades, the field of organic electronics has offered promise in fabricating efficient commercial devices [63]. In 1987, small molecules were the first to be incorporated into light emitting diodes and were deposited by vacuum evaporation [90]. Since the first report of light-emitting diodes using polymers instead of small organics in 1990 [91], conjugated light-emitting polymers (LEPs) have attracted a large amount of research interest. Given their relatively high quantum yields and low power consumption, they are ideal candidates for active elements in solid-state lighting applications, and flat-panel and flexible displays. LEPs are typically processed using liquid phase techniques which can be simpler and cheaper than the thermal evaporation required to deposit small molecules [92]. However, as the demand for better performance and more complex device structures increases, the disadvantages of liquid-phase processing become more evident. For example, special care must be taken in fabricating multi-layered thin films due to unwanted solvent interactions between adjacent layers.

5.1.1 Physics of OLEDs/PLEDs

Conjugated polymers are now being incorporated into optoelectronic devices for commercial use [63]. The two main types of these organic light emitting devices (OLEDs) are small-molecule OLEDs (sm-OLEDs), and polymer OLEDs (P-OLEDs, or PLEDs). Their basic method of operation is the same and relies upon the injection of electrons into the lowest unoccupied molecular orbital (LUMO, or π^* energy band)

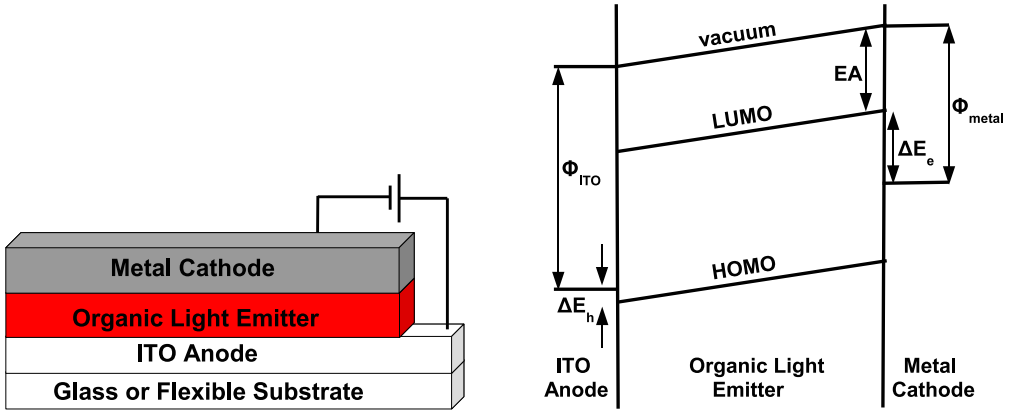

Figure 5.1: A schematic of the simplest OLED structure (left). A voltage applied between the cathode and the anode produces light in the organic region. Right: the accompanying energy diagram. Shown in the diagram are the respective work functions, Φ, of the anode and cathode, the barrier heights for carrier injection, ΔE, and the electron affinity (EA) of the organic.

and the injection of holes into the highest occupied molecular orbital (HOMO, or π band) of the organic light emitter. This is achieved by sandwiching the light emitter between two different electrodes and applying a voltage across them (figure 5.1). The applied voltage drives current through the device, and electrons and holes recombine across the LUMO-HOMO bandgap, emitting a photon in the process. For efficient electron injection, a low work function metal (e.g. Ca, Mg, or Al) is typically used as the cathode. For the anode, a high work function material is desired so that holes are easily injected into the HOMO. One of these electrodes must be optically transparent in order for the generated light to escape the device, therefore the anode is typically made from indium tin oxide (ITO). ITO can be deposited at room temperature [93], is approximately 90% transparent in thin film form [94], and has a relatively high work function of $\sim$4.5 eV [95]. The image on the right in figure 5.1 shows the energy diagram associated with a typical OLED.

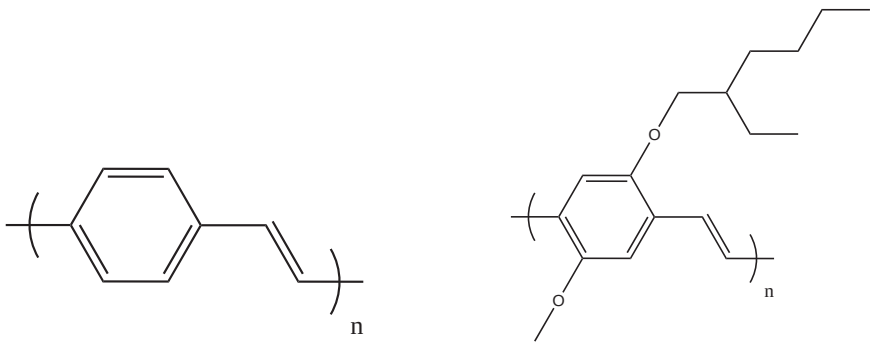

Figure 5.2: Chemical structure of PPV (left), and MEH-PPV (right). The side groups on the 2- and 5-positions of the MEH-PPV reduce the HOMO-LUMO gap from green to red, but render it soluble.

5.1.2 MEH-PPV Overview

Poly[2-methoxy-5-(2'-ethyl-hexyloxy)-1,4-phenylene vinylene] (MEH-PPV), is a member of the most well known class of conjugated light emitting polymers, poly(phenylenevinylenes) (PPVs). PPVs were first discovered by the Friend group at the University of Cambridge in 1990 [91], and sparked the development of what is now the huge field of PLED research. In its native form, PPV is a green emitter insoluble in any common solvent. Substitution of side groups on the benzene ring render the polymer soluble but they reduce the HOMO-LUMO gap from green to red (see figure 5.2)

5.1.3 Current deposition techniques

The ease of processing small organics has allowed small molecule OLEDs to become the first emerging organic optoelectronic technology. Films of small molecules can be grown by thermal evaporation, a clean process that is done in a vacuum environment and one that has been widely used for many years. Larger organics such as

polymers, however, are too large to be thermally evaporated intact and are therefore limited to a solution phase processing [19]. Liquid phase deposition techniques such as spin-coating and ink jet printing were discussed in section 4.1.3, and therefore will not be represented here. We simply note that the same conventional techniques used to deposit PEDOT:PSS in chapter IV also apply to the deposition of MEH-PPV.

5.2 RIR laser deposition of MEH-PPV films

The light-emitting polymer poly[2-methoxy-5-(2-ethylhexyloxy)-1,4-phenylene vinylene] (MEH-PPV), was chosen due to the large amount of existing literature regarding its properties. MEH-PPV (M_w = 40,000 - 70,000 Da) was obtained from Sigma Aldrich, and the PEDOT:PSS (Baytron® P) was obtained from H. C. Starck and used without further processing.

For ablation of the polymer layers, a RIR-MAPLE approach was used and the laser was tuned to a vibrational mode of the matrix. For the deposition of PEDOT:PSS, the native solution was mixed with 30% by weight of *N*-methyl-2-pyrrolidinone (NMP), following the protocol in section 4.2. The laser was tuned to 3.47 μm, a wavelength resonant with the C-H stretch of the NMP matrix. PEDOT:PSS films grown by this method typically had thickness of 120 $\pm$ 35 nm as measured by profilometry. The MEH-PPV deposition was carried out by irradiating a 1% by weight frozen solution of MEH-PPV in 1,2-dichlorobenzene (DCB) at either 3.26 μm or 6.87 μm, corresponding to the C-H stretching mode of the solvent, or the C-C=C ring mode, respectively. An infrared spectrum of DCB is shown in figure 5.3 showing the two absorption modes. Typical deposition rates were $\sim$ 20 nm per minute, giving film thicknesses of 200 $\pm$

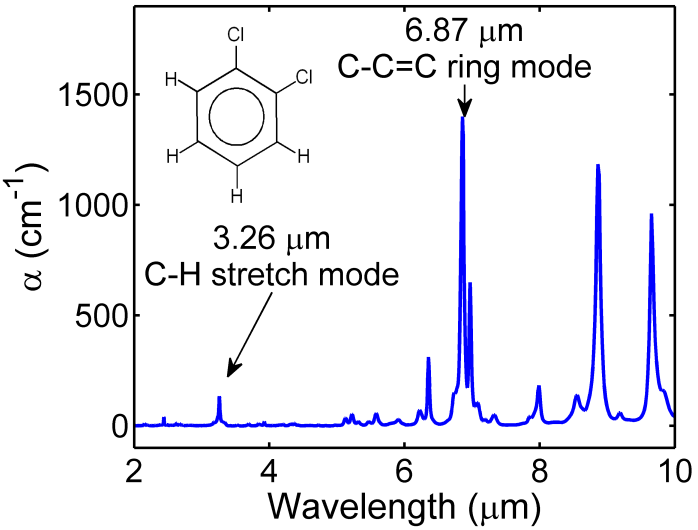

Figure 5.3: FTIR absorption spectrum of o-dichlorobenzene labeling the two modes targeted in these experiments. The absorption coefficient was measured using a liquid FTIR cell with known optical path lengths. The inset shows the molecular structure.

120 nm over a 10 minute deposition (the roughness of these films will be discussed later). Although the multi-layer depositions were done by breaking vacuum between depositions, the addition of a multi-target carousel into the chamber would allow for all depositions to be carried out in vacuum without venting to atmosphere.

The laser source used in these experiments was the W.M. Keck Free Electron Laser (FEL) [31]. The FEL has previously been described in section 1.4 and details about the laser are therefore omitted here. The macropulse energy as measured by a pyroelectric joulemeter was kept at approximately 10 mJ per macropulse, yielding a fluence of 1-2 J/cm^2 at the target surface. In these experiments the FEL was tuned to 3.47 μm for the PEDOT:PSS depositions (C-H stretching mode of the NMP solvent), or 3.26 μm and 6.87 μm (C-H and C-C=C modes of DCB, respectively) for

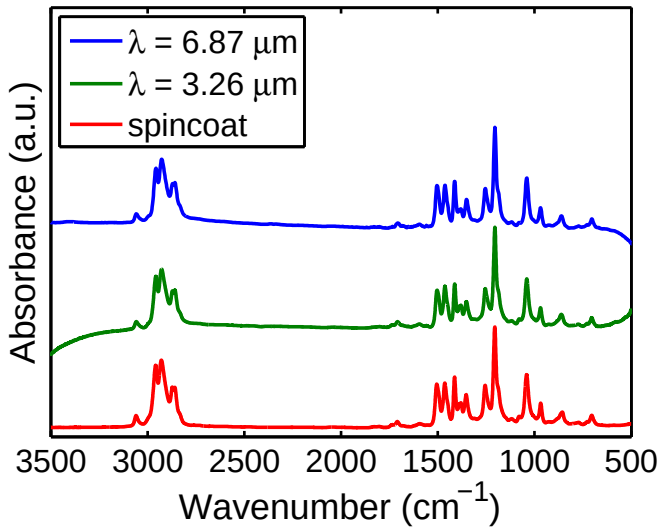

Figure 5.4: FTIR absorption spectra of laser-deposited MEH-PPV films.

the MEH-PPV depositions.

5.2.1 FTIR spectroscopy

As a first step in assessing the integrity of the deposited polymer layers, FTIR spectroscopy was employed to analyze the local bonding structure of the films. Spectra were taken under vacuum in a Bruker IFS 66v FTIR spectrometer with a 12 mm aperture. PEDOT:PSS films deposited under the conditions used in these experiments were discussed in chapter IV, and FTIR spectra confirm that the bonding structure is the same as spin-coated samples. The FTIR spectra for MEH-PPV films deposited at 3.26 μm and 6.87 μm are displayed in Figure 5.4, and again the spectra show no major deviations from a spin-coated spectrum.

5.2.2 Film morphology

To analyze the surface morphology of the laser-deposited films, optical microscopy (OM) was performed on the MEH-PPV layers and is shown in figure 5.5. The images

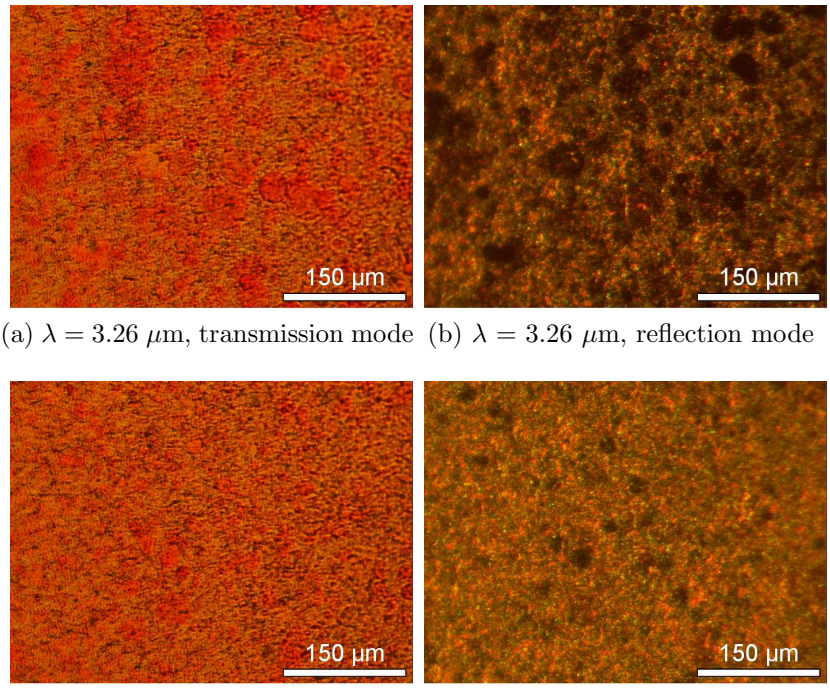

(a) $\lambda = 3.26$ μm, transmission mode (b) $\lambda = 3.26$ μm, reflection mode

(c) $\lambda = 6.87$ μm, transmission mode (d) $\lambda = 6.87$ μm, reflection mode

Figure 5.5: Optical micrographs of laser-deposited MEH-PPV films. The images for each wavelength are on the same spot of the film surface.

suggest differences in ablation at 3.26 μm, the morphology of which is characterized by the presence of $\sim$ 10 - 50 μm diameter droplets, and 6.87 μm, where the morphology demonstrates a more granular texture. The presence of droplets is more readily seen when viewed in transmission mode, as in Figures 5.5b and 5.5d. It is clear from the transmission images that there is a greater abundance of the droplets on the surface

of the film ablated with $\lambda = 3.26$ μm irradiation. In either case, it is evident that in order to compete in efficiency with spin coated films - whose roughness is typically a few nanometers at most - the surface quality of these films must improve.

Stylus profilometry confirms the roughness of the laser-deposited films. Figure 5.6 shows a 500 μm long scan (stylus radius = 12 μm, applied force = 6 mg) of typical laser-deposited films and a spin coated film for comparison. The RMS roughness in

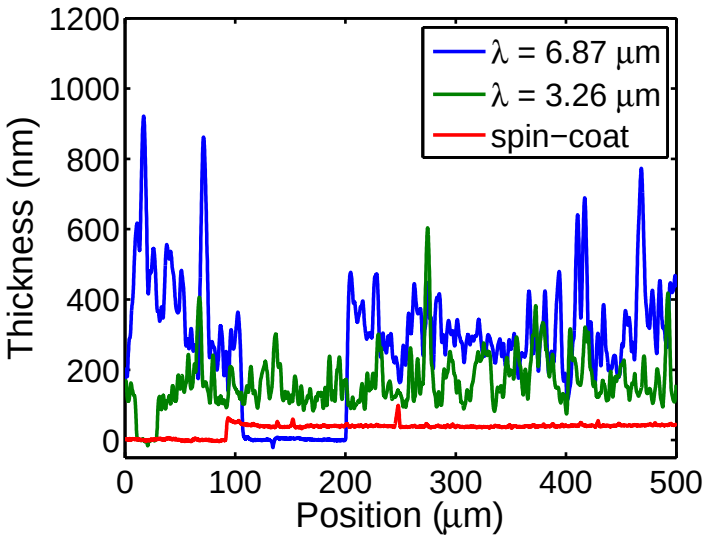

Figure 5.6: Profilometry scans of laser-deposited MEH-PPV films. The baseline reference points come from a razorblade scratch of the surface.

the laser-deposited case is at least an order of magnitude larger. The surface profiles indicate that for both ablation wavelengths, features are typically $\sim$ 10 microns in diameter and are anywhere from 50-500 nm high. Recall from section 4.2 in chapter IV that data with PEDOT:PSS showed that ablation from a larger focal spot size

gives rise to a larger surface roughness. Since this is the case, then depositing films with surface features smaller than the spot size of the laser beam (several microns, at best) may prove to be a challenge. Perhaps it is possible to dope other co-matrices into the target solution prior to freezing that induce some chemical changes in the polymer (similar to PEDOT:PSS depositions in reference [37]), but this has proved to be unsuccessful to date.

The same problem exists with MEH-PPV deposition as does with PEDOT:PSS depositions described in chapter IV - while the molecular structure of the polymer film seems to be intact as evidenced by the films' functionality, the poor surface quality of the films almost excludes them from being part of any successful electronic or optoelectronic device. While the thermal properties of DCB are not as known as well as those of water, we may estimate that the stress and thermal confinement times, τ_s and τ_{th}, are similar to those listed in table IV.2 for water. This means that the FEL macropulse is not thermally confined and laser energy deposited as heat begins to diffuse out of the focal volume before the laser pulse is over leading to a gradual temperature rise in the target. Since spinodal decomposition followed by the recoil-induced ejection of liquid is likely the dominant mechanism for ablation, then a rough film surface consisting of droplets may be expected since most of the ablated material is removed as liquid, instead of a vapor. In fact, recent papers regarding the fundamental mechanisms of MAPLE posit that it may be physically impossible to create smooth MAPLE films due to the ejection of polymer-rich droplets of solvent which are a byproduct of spinodal decomposition [84, 14].

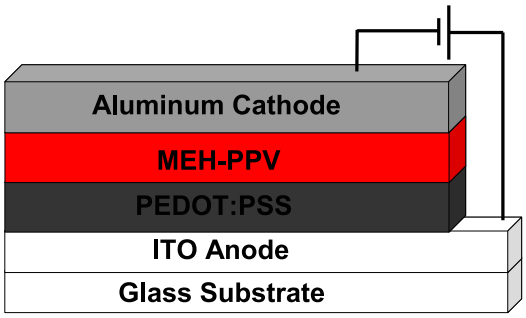

Figure 5.7: Schematic diagram of the PLEDs made by RIR-MAPLE.

5.3 Single and multi-layer device fabrication

PLEDs were fabricated with the structure shown in Figure 5.7. To investigate the role of the PEDOT:PSS, devices were made both with and without the hole-transport layer (refer to chapter IV for details on PEDOT:PSS).

For control device fabrication, spin-coating was used for polymer deposition since it is the most common method used in the literature. First, $\sim$ 15 nm thick indium tin oxide (ITO) coated glass substrates (Delta Technologies) were cleaned by sonication in acetone, methanol, and deionized water for 5 minutes each. The substrates were then exposed to UV-ozone for 10 minutes to remove any residual organic contaminants. For the spin-coated devices, PEDOT:PSS was used as received ($\sim$ 1.3% by weight in H_2O) and was spun onto the ITO at 4500 rpm. It was then baked at 100° C for 10 minutes to remove residual solvent, yielding a film with thickness of 64 $\pm$ 1 nm as measured by stylus profilometry (Veeco Dektak 150). The MEH-PPV was spun at 2000 rpm from a 1% by weight solution in (DCB). The film was baked at 65° C for 10 minutes to drive off residual DCB, and the resulting MEH-PPV film thicknesses were

45 ± 3 nm (± refers to RMS roughness). After polymer deposition was complete, ∼ 100 nm of aluminum was thermally evaporated through a shadow-mask for the device cathode. The shadow-mask produced an array of 500 μm diameter circular cathodes across the entire 25 mm substrate, yielding an active device area of 0.002 cm^2.

5.3.1 Electroluminescence spectroscopy

Electroluminescence (EL) spectra of both spin-coated devices and laser-fabricated devices were acquired with a fiber-coupled Acton SpectraPro 300i spectrometer and are shown in Figure 5.8. The spectra all exhibit the same peak wavelength to within a few nanometers, suggesting that the MEH-PPV suffers no significant reduction in chain length during the deposition process. It is known that decreasing the conjugation length (*i.e.* chain shortening) in organic light-emitters leads to band-gap increase [96]. Since we observe no persistent blue-shift in the emission spectra of laser-deposited films with respect to those of spin-coated films, we conclude that no appreciable chain shortening takes place during the deposition process. In general though, the laser-deposited spectra seem to be broader than spin-coated spectra, most likely due to inhomogeneous broadening caused by the differences in film morphology and thickness in a given device. The conformation of the polymer chains in the film affects the electrical and optical properties of the device, and is a function of processing conditions. It has been shown that changing the thickness of the light emitting layer from 70 nm to 30 nm (spin-coated) shifts the center emission wavelength of the device from 499 nm to 509 nm [97, 98]. Thus, the large thickness variations over the active area of our laser-deposited PLEDs likely leads to the spectral broadening

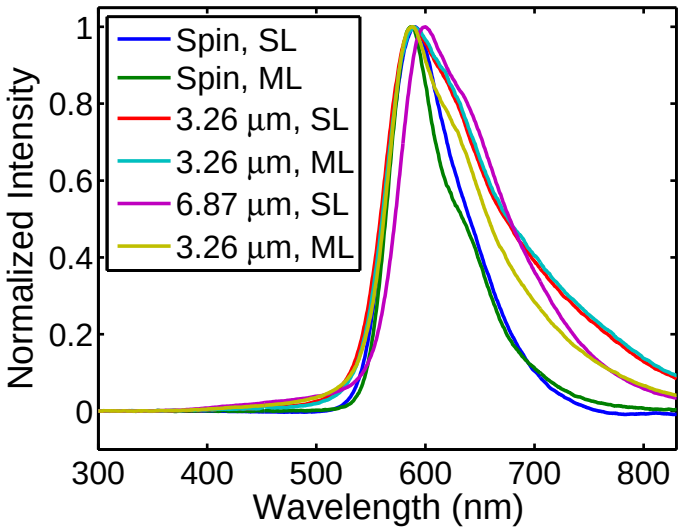

Figure 5.8: Electroluminescence spectra of laser-deposited PLEDs. ML and SL refer to multi-layer and single layer devices made with or without PEDOT:PSS, respectively.

observed in figure 5.8.

5.3.2 IV characteristics

To investigate the electrical behavior of the devices, I-V curves were measured (Keithley 236 Source Meter) and are displayed in Figure 5.9. The data are plotted on separate axes due to their differences in turn-on voltages and operating currents. Given the varying morphology of the different devices, it is no surprise that their I-V characteristics vary. For instance, it is well known that the point at which the device turns on is a function of electric field, rather than voltage [99]. Given the large surface roughness of the laser-deposited films (see Figure 5.6 for surface scans), the devices have a large range of electric field values and gradients across the polymer

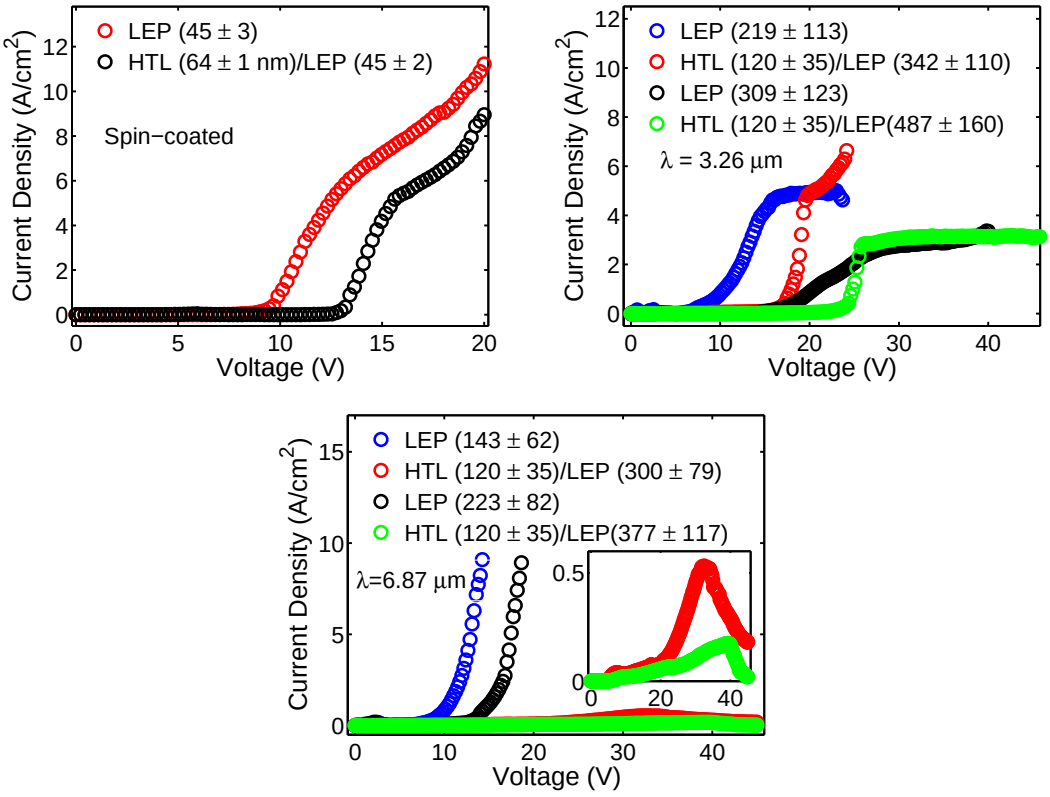

Figure 5.9: Current as a function of voltage for different laser-deposited devices. In each graph the film thicknesses of the light-emitting polymer (LEP) and the hole-transport layer (HTL) are indicated along with the RMS roughness values in nm. The inset in the bottom graph is a magnified scale of the two thicker MEH-PPV device curves to better show their structure.

layers, leading to non-uniform light-emitting and electrical characteristics. This is also evidenced by the fact that when electrically driven under a microscope so that inhomogeneities across the 500 μm cathode are magnified, the laser-deposited devices tend to emit light in a spatially non-uniform way across the device area, while spin coated devices display very uniform electroluminescence. In fact, we estimate based on the magnified device imaging that in some cases, as little as 30% of the laser-deposited devices are actually functional. The actual photon yield from any one laser-deposited device over an entire 25 mm substrate, however, varies due to the film surface roughness and some devices may emit over $\sim$ 80% of the total device area.

5.4 Conclusions

Multi-layered polymer light emitting diodes have been successfully fabricated in an all vacuum environment by resonant infrared pulsed laser deposition. The emission characteristics displayed by these devices were similar to those of spin-coated devices, suggesting that the light emitting polymer survives the deposition process and remains intact in the film. FTIR spectroscopy also confirmed this, as absorption spectra of spin-coated and laser-deposited films were nearly identical. The RMS roughness values must be decreased by at least an order of magnitude in order to compete with the current industrial standards of $\pm$ 1 nm over large-area substrates.

The facts that the RMS roughness of the laser-deposited films are so large, and that liquid droplets are deposited onto the substrate further support the idea of spinodal decomposition being the primary mechanism responsible for ablation. The superheated surface material decomposes into a mixture of gas and liquid and imparts

a force onto the pre-melted liquid layer below. The recoil force generated by the expanding superheated plume drives the liquid out of the laser focal volume which then travels to the substrate as droplets or liquid jets. The substrate is essentially spray-coated, leading to the creation of a rough film. This is likely exacerbated by the facts that DCB has a low melting temperature (-17 °C) so that it is quickly melted upon laser absorption, and that the laser pulse is not thermally confined so that the temperature of the target gradually increases over time.

CHAPTER VI

CONCLUSION

Laser ablation of polymers is a scientifically rich and complex phenomenon that has many potential technological applications. Since the first report of polymer ablation in 1982 [7], the exact mechanisms of polymer ablation by different lasers have been intensely studied. The growing abundance of high-powered lasers since the 1960s has not only increased the number of possibilities for new types of laser-polymer processing, but has also opened the door to the exploration of laser-materials interactions at high excitation densities that was not previously accessible.

Since its discovery in 2001, the physics governing RIR laser ablation process had not been well understood, and it was the partial aim of the work presented in this dissertation to better understand it. This aim has been completed through a series of experiments and calculations which evidenced that the ablation process consists of a thermal component followed by a hydrodynamical component. This combination of mechanisms allows for ablation and deposition of at least partially intact polymer films [36, 100], due to the fact that it is not entirely thermal. Phase explosion of a superheated surface layer is responsible for the initial stages of material removal, and constitutes the thermal component of the process. This is followed by the hydrodynamic event of recoil-induced liquid ejection, which is responsible for the bulk of the material removal in RIR ablation. These mechanisms are consistent with what has been published in the literature concerning tissue ablation [22, 23], but this was the

first comprehensive set of experiments which explained the mechanisms underlying the RIR ablation of polymers.

Work in this dissertation also investigated the the use of RIR polymer ablation in an applied capacity for the growth of electronic and opto-electronic polymer thin films. While it is not likely that this technology is revolutionary, the results presented in chapters IV and V suggest that with proper engineering and refinement, RIR-PLD and RIR-MAPLE could be useful in certain applications where a vapor-phase polymer deposition process is desirable. For instance, previous work has shown that heating the substrate to the melting temperature during MAPLE deposition can smooth out the resulting film [101]. Or perhaps combining spin coating and RIR-PLD by rapidly spinning the substrate during deposition may smooth out the films, since the polymer is likely deposited as liquid droplets. Or as was the case for PEDOT:PSS deposition discussed in chapter IV, appropriate co-matrices could be doped into the target solution prior to deposition to create smoother films. Whether or not this technology proves to be successful on an industrial level, however, remains to be seen.

APPENDIX A

RELEVANT PROPERTIES OF POLYMER SYSTEMS

This appendix outlines some of the general properties related to polymer systems. It is intended to provide the background necessary to understand the work presented in this dissertation, and therefore only discusses the most relevant topics.

A.1 Molecular weight distribution

Polymers are molecules whose molecular structure is based on the repetition of a fundamental monomer unit. They are typically described by their abbreviated chemical formula (*e.g.* $(CH_2\text{-}C_7H_6)_n$ for polystyrene, where n is the number of repeat units), and their total molecular weight. Polymer molecular weight is usually given in Daltons (Da) or kiloDaltons (kDa), where one Dalton is equivilant to one atomic mass unit (amu). The molecular weight of a bulk polymer is typically defined through the statistical ensemble of individual polymer chains, since most bulk polymer materials have a distribution of chain lengths. The number average molecular weight, M_n is the arithmetic mean of the weights of the individiual polymer chains:

$$M_w = \frac{\sum_i N_i M_i}{N_i} \tag{A.1}$$

An alternative way to express the molecular weight is through the weight average, M_w, which is the arithmetic mean weighted by the molecular weights:

$$M_w = \frac{\sum_i N_i M_i^2}{N_i M_i} \tag{A.2}$$

A measure of the width of the polymer molecular mass distribution is called the polydispersity index (PDI) and is defined as the ratio of M_w to M_n:

$$PDI = \frac{M_w}{M_n} \tag{A.3}$$

If $M_w = M_n$, then the PDI = 1 and the material is monodisperse, *i.e.* every polymer chain has the exact same molecular weight. In reality, however, most polymer systems are polydisperse. For instance, the polystyrene used in chapter II had a M_w of 224 kDa, and a PDI of 1.8.

A.2 FTIR spectra and vibrational properties

The collection of intramolecular covalent bonds which hold atoms together in a polymer give rise to a unique bonding structure. The requirement for direct photon absorption to occur into a localized covalent bond is that there be a net change in dipole moment as the atoms or functional groups oscillate about the bond center. To estimate the frequencies at which light would most readily be absorbed, we assume that a covalent bond acts as a spring of force constant k, holding two masses, m_1 and m_2 together. Solving the differential equations of motion for this coupled-mass

system yields harmonic motion with a resonant frequency of [102]

$$\nu = \frac{1}{2\pi c}\sqrt{\frac{k}{\mu}} \tag{A.4}$$

where c is the speed of light, and μ is the reducued mass,

$$\mu = \frac{m_1 m_2}{m_1 + m_2} \tag{A.5}$$

To get a rough estimate of the resonant absorption frequency of a C-H bond, we use a value of $k = 5{\times}10^{-5}$ dyne/cm, which is typical for a single covalent bond [102], and $19.8{\times}10^{-24}$ and $1.64{\times}10^{-24}$ g as the masses for the carbon and hydrogen atoms, respectively. Plugging these values into equation A.4 yeilds a resonant frequency of ~ 3041 cm^{-1}, which corresponds to a resonant wavelength of ~ 3.29 μm. The actual resonance wavelength for the C-H stretching bond in organic compounds is 3.3-3.4 μm, so the simple calculation outlined above comes close to estimating the correct value. A more precise calculation for the C-H resonance wavelength in a particular molecule or functional group, however, would need to include the effects specific to the bond's local environment.

APPENDIX B

FINITE-ELEMENT CODE

Presented here is the exact code used to calculate the laser-induced temperatures for polystyrene in section 2.3.4.

```
% Model to predict temp rise in a PS target during IR laser irradiation.


%%%%%%%%%%%%%%%%%%%%%%%%%%%%%%%%%%%
isdyn = 0; % dynamic calculation
iscalc=1; % actually do calculation
changeprops = 0; % whether or not to modify specific heat and abs. coefficient
isstat = 1; % static calculation
%%%%%%%%%%%%%%%%%%%%%%%%%%%%%%%%%%%

% Laser Parameters
%%%%%%%%%%%%%%%%%%%%%%%%%%%%%%%%%%%
F = 2; % Fluence in J/cm^2
wv = 3.42; % wavelength in um
t_p = 4.0; % pulse time in us.
w = 250; % laser spot radius in um
%%%%%%%%%%%%%%%%%%%%%%%%%%%%%%%%%%%

% Material Properties
%%%%%%%%%%%%%%%%%%%%%%%%%%%%%%%%%%%
abs_cof = 551; %absorption coefficient in cm^-1 @r.t.
T_i = 22; % initial temperature in C
T_m = 240; % melting temperature in C
C = 1.3; % specific heat of solid in J/g/degC
den = 1.05; % density in g/cm^3
k_s = 8e-04; % thermal conductivity of solid in W/cm/degC
v_s = 2.2e5; % speed of sound in solid in cm/s
%%%%%%%%%%%%%%%%%%%%%%%%%%%%%%%%%%%
mu = 10000/abs_cof; % 1/e penetration depth

% grid
%%%%%%%%%%%%%%%%%%%%%%
dx = w/50;
dz = mu/120; %120
dt = t_p/40;
x = [-3*w:dx:3*w]';
if isdyn
z = [0:-dz:-5*mu]'; % make z grid smaller to reduce calculation time
```

```
else
z = [0:-dz:-5*mu]';
end
t = [dt:dt:t_p]';
%%%%%%%%%%%%%%%%%%%

%%%%%%%%%%%%%%%%%%%%%%%%%%%%%%%%%%%%%%%%%%%%%%%%%%%%%%%%%%%%%%%%%%%%%%%%%%%
den_um = den/(1e4)^3; % density in g/um^3
F_um = F/(1e4)^2; % fluence in J/um^2
abs_cof_um = abs_cof/1e4; % absorption coefficient in um^-1
E = F*pi*(1e-04*w)^2; % beam energy in J
V = (length(x)*dx)^2*length(z)*dz; % total computation volume
dv = dx^2*dz; % grid volume element in cubic microns
m =den*dv; % mass in grams
abs_cof = abs_cof./1e4; % absorption coefficient in um^-1
h = 6.63e-34; % Planck's constant in J*s
c = 3e8; % speed of light in m/s
%%%%%%%%%%%%%%%%%%%%%%%%%%%%%%%%%%%%%%%%%%%%%%%%%%%%%%%%%%%%%%%%%%%%%%%%%%%


%%%%%%%%%%%%%%%%%%%%%%%%%%%%%%%%%%%%%%%%%%%%%%%%%%%%%%%%%%%%%%%%%%%%%%%%%%%
% STATIC CALCULATION
% Assume laser propagating in z-direction and that the beam is gaussian and
% symmetric in x and y.  Assume linear absorption by target.
%%%%%%%%%%%%%%%%%%%%%%%%%%%%%%%%%%%%%%%%%%%%%%%%%%%%%%%%%%%%%%%%%%%%%%%%%%%

if isstat

% Calculate Energy distribution after laser absorption
clear T;

E_z = exp(z/mu); % distribution in z
E_x = exp(-2.*x.^2/(w^2)); % distribution in x
E_x2 = repmat(E_x,1,length(z))';
E_z2 = repmat(E_z,1,length(x));
E_xz = 2*F_um*abs_cof_um*E_x2.*E_z2; % energy deposited in cell

a1 = sum(sum(E_xz));
for ii = 1:length(x)
    a(ii) = a1*E_x(ii);
end
E_tot = sum(a); % this should give back the total energy deposited

% Calculate temperature based on energy distribution using E = mc(Tf-Ti)
T = E_xz/(den_um*C)+T_i;

% plots
%%%%%%%%%%%%%%%%%%%%
isplot1 = 1; % temperature plot after laser absorption (static calculation)
%%%%%%%%%%%%%%%%%%%%

if isplot1
    figure(1),clf
    imagesc(x,z,T)
```

```
    set(gca,'ydir','normal')
    colorbar
    xlabel('x (\mum)'),ylabel('z (\mum)')
    figset2
    %figset_thesis
end
end

%%%%%%%%%%%%%%%%%%%%%%%%%%%%%%%%%%%%%%%%%%%%%%%%%%%%%%%%%%%%%%%%%%%%%%%%%%%%%%%%
% DYNAMIC CALCULATION
% Assume laser propogating in z-direction and that the beam is gaussian and
% symmetric in x and y.  Assume linear absorption by target with temp. dep.
% specific heat and absorption coefficient.  Assume flat-top laser pulse profile
% in time.
%%%%%%%%%%%%%%%%%%%%%%%%%%%%%%%%%%%%%%%%%%%%%%%%%%%%%%%%%%%%%%%%%%%%%%%%%%%%%%%%

if isdyn % let pulse come in in increments; modify props according to temp rise
if iscalc
    clear T;
    temp_abs = load('PS_tempdep_abs.txt'); % temp-dependent absorption data
    temp = temp_abs(:,1);
    wvs = [3.31 3.42 6.25 6.70];
    for iwv = 1:length(wvs)
        if wv == wvs(iwv)
            abs = temp_abs(:,iwv+1);
        end
    end
    temp2 = 35:1:250;
    abs2 = interp1(temp,abs,temp2); % interpolate temp dep abs
    cp_t = load('C_p _vs_T_Karasz_mod.txt'); % temperature dependent c_p data
    temp_c = cp_t(:,1);
    cp = cp_t(:,2);

    E_0x = 2*F*dx^2; % normilization factor
    E_x = exp(-2.*x.^2/(w^2)); % functional distribution in x
    E_x2 = repmat(E_x,1,length(z))';
    dE = E_0x/(t_p/dt); % break up into energy regions determined by time steps
    E_t = dE:dE:E_0x;
    T = T_i*ones(length(z),length(x)); % initialize initial temp. matrix
    % check for total energy:
    b1 = sum(E_0x*E_x);
    for ii = 1:length(x)
        b(ii) = b1*E_x(ii);
    end
    E_tot = sum(b); % should give back E
    e_xt = b1/(t_p/dt):b1/(t_p/dt):b1; % energy deposited per cell in x over time

    ac = abs_cof;
    Cp = C;

    e = zeros(length(z),length(x)); % initilize energy matrix with 0 energy
       % (excluding ambient temperature)
    for ie = 1:length(E_t)
        E_t = dE*E_x; % x distribution of energy in slice of pulse
```

```
    for ix = 1:length(E_x)
        for iz = 1:length(z)

            if changeprops
                %%%%%%%%%%%%%%%%%%%%%%%%%
                % modify absorption coefficient
                if T(iz,ix)>250
                    error('Temperature above 250 C');
                end
                if T(iz,ix)<35
                    f(iz,ix,ie) = 1;
                    ac = abs_cof; % no temp dep data below 35 C
                    abscof(iz,ix,ie) = ac;
                else
                    g(iz,ix,ie)=1;
                    tt(iz,ix,ie) = find(temp2==round(T(iz,ix)));
                    ac = abs_cof*abs2(tt(iz,ix,ie)); % new abs. coefficient
                    abscof(iz,ix,ie) = ac;
                end
                %%%%%%%%%%%%%%%%%%%%%%%%%%%%
                % modify specific heat
                tc(iz,ix,ie) = find(temp_c==round(T(iz,ix)));
                Cp = cp(tc(iz,ix,ie));
                cp_zt(iz,ix,ie) = Cp;
                %%%%%%%%%%%%%%%%%%%%%%%%%%%%
            end

            if iz==1
             % energy deposited by laser
                e_l(iz,ix,ie) = E_t(ix)*ac*dz;
            else
             % energy deposited by laser
                e_l(iz,ix,ie) = (E_t(ix)-sum(e_l(1:iz-1,ix)))*ac*dz;
            end

            e(iz,ix) = e(iz,ix)+e_l(iz,ix,ie); % final energy of cell
            e_xzt(iz,ix,ie) = e(iz,ix); % final energy of cell with time
            T(iz,ix) = e(iz,ix)/(m*Cp)+T_i; % final temperature of cell
            T_xzt(iz,ix,ie) = T(iz,ix); % final temp of target with time

        end
    end
end

if changeprops
    T_xzt_dyn = T_xzt;
    for ii = 1:length(t)
        T_max_dyn(ii)=max(T_xzt(1,:,ii));
    end
else
    T_xzt_stat = T_xzt;
    for ii = 1:length(t)
        T_max_stat(ii)=max(T_xzt(1,:,ii));
    end
```

```
    end
end


% plots
%%%%%%%%%%%%%%%%%%%%%%
isplot1 = 1; % plot 2D temp at end of laser pulse (dynamic)
isplot2 = 0; % plot max surf. temp. vs. time (dynamic)
isplot3 = 1; % plot max surf. temp. vs. time for static & dynamic
%%%%%%%%%%%%%%%%%%%%%%

if isplot1
    figure(1),clf
    imagesc(x,z,T)
    set(gca,'ydir','normal')
    colorbar
    xlabel('x (\mum)'),ylabel('z (\mum)')
    figset2
end

if isplot2
    figure(2),clf
    plot(t,T_max,'or')
    %t1 = text(2,200,['F = ',num2str(F),' J/cm^2']);
    set(gca,'xlim',[-0.1 4.1])
    xlabel('Time (\mus)'),ylabel('Max Surface Temperature (^oC)')
    figset
end

if isplot3
    figure(3),clf
    plot(t,T_max_dyn,'or',t,T_max_stat,'sb')
    set(gca,'xlim',[-0.1 4.1],'ylim',[0 500])
    xlabel('Time (\mus)'),ylabel('Max Surface Temperature (^{\circ}C)')
    legend('Static Parameters','Dynamic Parameters',2)
    figset
    t1 = text(2,200,['\Phi = ',num2str(F),' J/cm^2'],'fontname','arial',...
        'fontsize',18);
end
end
```

APPENDIX C

RIR-PLD SYSTEM

This appendix describes the RIR-PLD system that was used to deposit polymer thin films using the FEL. The system consists of three main parts: the vacuum chamber, system hardware, and system software. All polymer depositions described in this dissertation were done using this deposition system. All components in the system were designed, purchased, and custom-assembled in the summer and fall of 2004 with help from the machine shop and other graduate students.

Figure C.1 shows a picture of the RIR-PLD laboratory labeling both the FEL beam delivery system and the deposition chamber. The FEL travels in the evacuated blue pipe until it reaches the exit window of the delivery system, where it then travels approximately 3 meters through air to the deposition chamber.

C.1 Vacuum chamber

Figure C.2 shows a detailed picture of the vacuum chamber with its major components labeled. Not visible in the photograph is the turbomolecular (turbo) pump which keeps the chamber pumped down to a pressure of $\sim$1x10^{-5} Torr. The turbopump sits directly below the turbo valve labeled in figure C.2 and continuously pumps on the chamber to ensure it stays clean and free of airborne contaminants.

Light from FEL enters the chamber *via* a BaF_2 window indicated in figure C.2 and is focused onto a target which is located at the center of the chamber. The vaporized

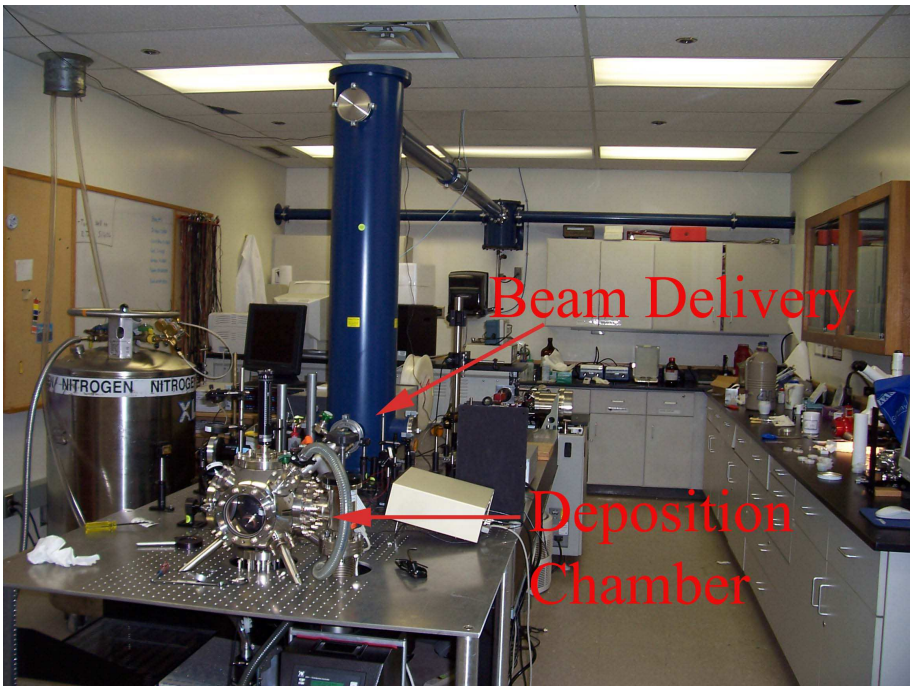

Figure C.1: Photograph of the RIR-PLD laboratory

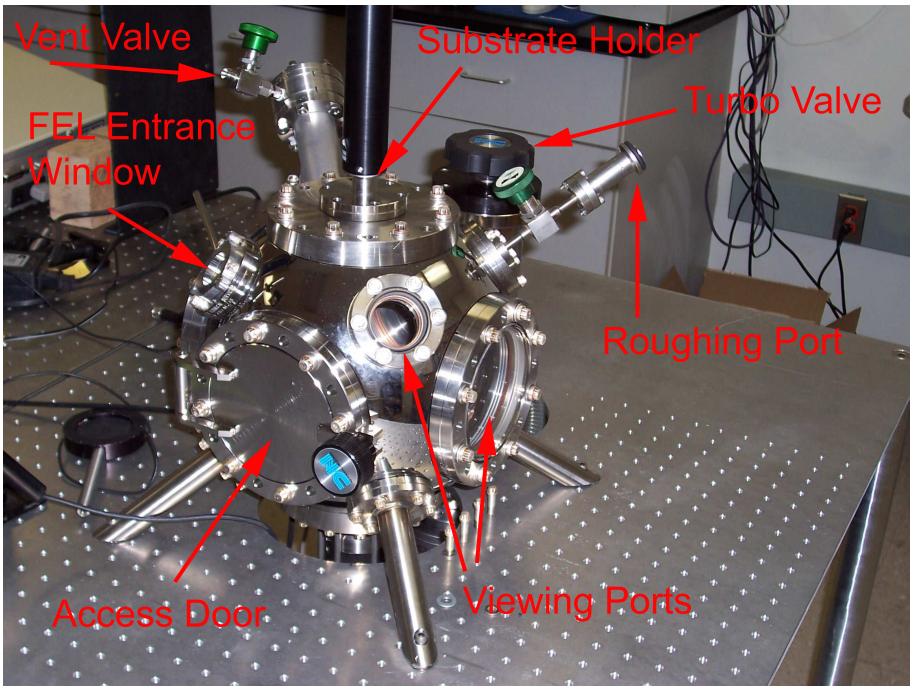

Figure C.2: Photograph of the RIR-PLD vacuum chamber

plume is then collected onto a growth substrate attached to the substrate holder for film growth. The laser beam is continuously scanned across the surface of the target in order to achieve uniform film deposition and a consistent target surface (the scanning system is described below in section C.2.1). To keep the system as contaminant-free as possible, the vent valve is connected to a dry nitrogen purge line which prevents water vapor in the ambient atmosphere from condensing onto the chamber walls. As another measure in keeping the deposition chamber clean, periodic cleaning with a series of organic solvents followed by a 6 hour bake-out at 200° C was employed. With this type of routine maintenance, film depositions could be done at a pressure of $\sim$5x10^{-5} Torr, which was achieved in $\sim$6 minutes after being at ambient pressure. The chamber in the pressure was monitored by a Pirani gauge for 2x10$^{-3} < p <$760 Torr, and a standard ion-gauge for $p <$2x10^{-3} Torr; these are on the backside of the chamber and not visible in figure C.2).

C.2 Hardware and software

Other than the turbo-pump mentioned above, the only other hardware component of the deposition system was the laser scanning assembly. The first generation scanning system involved pivoting a mirror that scanned the laser in one dimension, while the target itself was rotated in the chamber *via* a motor and a vacuum feedthrough. In this setup, both motors were stepper motors. The most current generation scanning assembly, however, has been upgraded to include two galvometric motors which pivot two mirrors so that the laser beam is scanned in two dimensions rather than in one, and the target is stationary inside of the chamber. As a consequence, the motion

control software likewise had to be upgraded, so both hardware and software aspects of the scanning assembly are described below.

C.2.1 Galvanometric Mirrors

As mentioned above, stepper motors originally operated the motion of the target and the lasers. The problem with the stepper motors was that they did not move at high enough speeds in order to ensure that two subsequent FEL pulses (spaced 33 ms apart) did not overlap spatially. As a result, we had to consider the effect of one laser pulse melting an area on the target, and another pulse being incident on the liquid layer before it could resolidify, causing a "splashing" effect. It was clear that a faster scanning system was needed. Moreover, there were disadvantages that came from rotating the target - namely that the implementation of any kind of coldfinger assembly to keep frozen targets at liquid Nitrogen temperature was impractical.

The solution to the problem was the use of two galvanometric (galvo) motors that pivoted mirrors about an axis in order to steer the laser beam. Galvo motors are common in any application involving scanning lasers; in fact, galvo mirrors find their most common use in optical barcode scanners that one encounters in any grocery or retail store. Galvo motors are dc servo motors that have a position-sensing detector located in the shaft and feedback electronics so that the motor and controller always know the motor's position. Application of an analog voltage causes the motor shaft to rotate with an angular displacement proportional to the applied voltage. Thus, applying a time-varying voltage in the form of a sine wave causes the motor to rock back and forth. A picture of the scanning motors along with the control boards (both

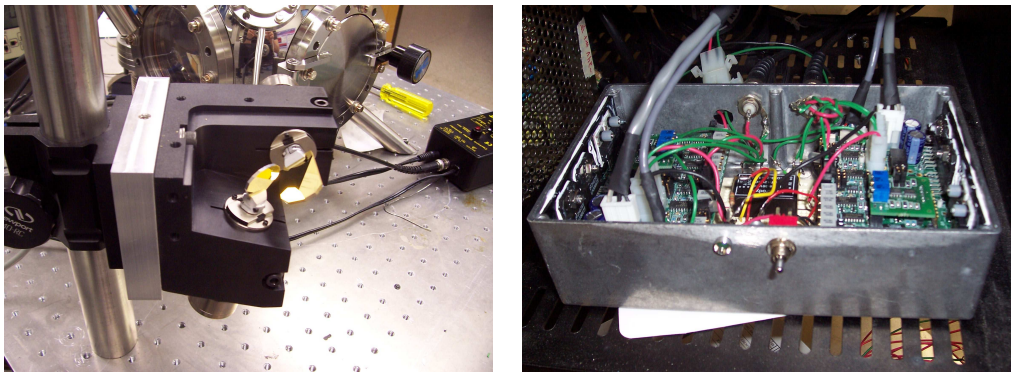

Figure C.3: Photograph of the galvometric scanning motors used to steer the laser beam. Also shown are the control boards in an enclosure.

purchased from Cambridge Technologies) is shown in figure C.3.

C.2.2 Motion Control Software

LabVIEW was used to write the motion control software for the RIR-PLD system. After the control boards for each motor was mounted into an appropriate enclosure (see figure C.3) the application of an analog voltage was all that was needed in order to move the motors. The challenge then was deciding the optimum way to move the motors such that laser pulses did not overlap while the target was uniformly irradiated.

Given the circular geometry of our ablation targets, the most efficient way to meet these criteria was to have the laser beam scan in a spiral pattern. If it continuously spiraled in and out at a sufficient speed, it would uniformly cover the target area and avoid overlapping subsequent laser pulses. This is critical because it is not possible to always irradiate a fresh surface with each shot, but provided that there is sufficient time for the target to cool between laser shots then splashing is avoided. There are

two orthogonal axes to the scanning system, we denote their position as a function of time as $x(t)$ and $y(t)$, where the actual directions of x and y (parallel or perpendicular to the laser propagation direction) are arbitrary and are determined empirically. If we parameterize their motion by time, t, then the equations

$$x(t) = A \sin \omega_\phi t \tag{C.1}$$

$$y(t) = A \cos \omega_\phi t \tag{C.2}$$

define a circle of radius A that is traced out at a constant angular frequency, ω_ϕ. To achieve a spiraling motion, we modulate the amplitude as well:

$$A = A(t) = A_0 \sin \omega_r t \tag{C.3}$$

where ω_r is the radial frequency since it describes the rate at which the beam spirals toward and away from the center. So the current equations trace out a spiral pattern (provided that $\omega_r < \omega_\phi$), but unfortunately not at the right rate. In order for the physical spacing between pulses to remain constant as the beam spirals inward, the angular frequency must increase as the radius decreases. That is, the time-dependent amplitude needs to modulate the angular component of motion. This is a common exercise in radio-frequency (RF) wave transmission, and can be done by treating the angular motion as a "carrier wave" of frequency ω_f that is modulated by a wave with modulation frequency, ω_m. The standard equation for this type of phase modulation

is

$$F(t) = \sin\left(\omega_f t + \beta \sin \omega_m t\right) \tag{C.4}$$

where β is defined as

$$\beta = \frac{\omega_f - \omega_m}{\omega_m} = \frac{\Delta\omega}{\omega_m} \tag{C.5}$$

Applying this formalism to our scanning equations, the position of each mirror as a function of time goes as

$$x(t) = A(t) \sin\left(\omega_\phi t + \beta \sin \omega_r t\right) \tag{C.6}$$

$$y(t) = A(t) \cos\left(\omega_\phi t + \beta \sin \omega_r t\right) \tag{C.7}$$

$$\beta = \frac{\omega_\phi - \omega_r}{\omega_r} = \frac{\Delta\omega}{\omega_r} \tag{C.8}$$

where $A(t)$ is defined in equation C.3. Now the radial amplitude modulates the angular frequency such that the beam speeds up in the middle and slows down at the edge of the target. By adjusting β, the difference in angular frequency at the edge of the target and the center of the target can be changed. For the actual film deposition process, it was empirically determined that the best ratio of ω_r to ω_ϕ was 0.01, with angular frequency of $\omega_\phi = 4.1$ Hz.

The essence of the software code that controlled the galvo motors is summed up in equations C.6 and C.7, with other minor details also incorporated that allowed for optimal user control and a smooth spiral pattern. In order to further automate the RIR-PLD deposition process, the program was also designed to operate a shutter

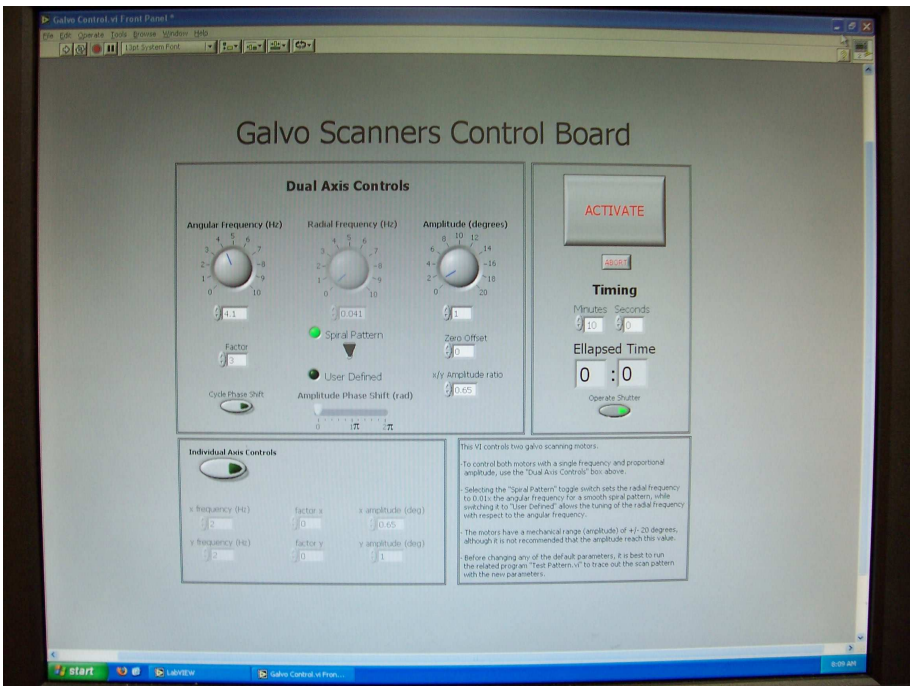

Figure C.4: Screenshot of the Galvo Scanners Control Board front panel.

that controlled the laser beam and stop the deposition after a user-defined time. A picture of the front panel of the LabVIEW program used for this is shown in figure C.4.

REFERENCES

[1] T.H. Maiman. Stimulated optical radiation in ruby. *Nature*, 187(4736):493–494, 1960.

[2] J.C. Miller. A brief history of laser ablation. *AIP Conference Proceedings*, 288(1):619–622, 1993.

[3] B.C. Smith. *Infrared Spectral Interpretation: A Systematic Approach.* CRC Press, 1999.

[4] D. Dijkkamp, T. Venkatesan, X.D. Wu, S.A. Shaheen, N. Jisrawi, Y.H. Min-Lee, W.L. McLean, and M. Croft. Preparation of Y-Ba-Cu oxide superconductor thin films using pulsed laser evaporation from high-T bulk material. *Applied Physics Letters*, 51:619, 1987.

[5] D.B. Chrisey, A. Pique, R.A. McGill, J.S. Horwitz, B.R. Ringeisen, D.M. Bubb, and P.K. Wu. Laser deposition of polymer and biomaterial films. *Chemical Reviews*, 103(2):553–576, 2003.

[6] D.B. Chrisey (Editor) and G.K. Hubler (Editor). *Pulsed Laser Deposition of Thin Films.* Wiley-Interscience, 2003.

[7] R. Srinivasan and V. Maynebanton. Self-developing photoetching of poly(ethylene-terephthalate) films by far ultraviolet excimer Laser-radiation. *Applied Physics Letters*, 41(6):576–578, 1982.

[8] Y. Kawamura, K. Toyoda, and S. Namba. Effective deep ultraviolet photoetching of poly(methyl methacrylate) by an excimer laser. *Applied Physics Letters*, 40(5):374–375, 1982.

[9] D.S. Shin, J.H. Lee, J. Suh, and T.H. Kim. Determination of the debris produced from poly(ethylene terephthalate) during KrF excimer laser ablation. *Applied Surface Science*, 252(6):2319–2327, 2006.

[10] B.J. Garrison and R. Srinivasan. Microscopic model for the ablative photodecomposition of polymers by far-ultraviolet radiation (193 nm). *Applied Physics Letters*, 44:849, 1984.

[11] R. Srinivasan and B. Braren. Ultraviolet-laser ablation of organic polymers. *Chemical Reviews*, 89(6):1303–1316, 1989.

[12] A. Pique, R. A. McGill, D. B. Chrisey, D. Leonhardt, T. E. Mslna, B. J. Spargo, J. H. Callahan, R. W. Vachet, R. Chung, and M. A. Bucaro. Growth of organic thin films by the matrix assisted pulsed laser evaporation (MAPLE) technique. *Thin Solid Films*, 356:536–541, 1999.

[13] D.M. Bubb, P.K. Wu, J.S. Horwitz, J.H. Callahan, M. Galicia, A. Vertes, R.A. McGill, E.J. Houser, B.R. Ringeisen, and D.B. Chrisey. The effect of the matrix on film properties in matrix-assisted pulsed laser evaporation. *Journal of Applied Physics*, 91:2055, 2002.

[14] A. L. Mercado, C. E. Allmond, J. G. Hoekstra, and J. M. Fitz-Gerald. Pulsed laser deposition vs. matrix assisted pulsed laser evaporation for growth of biodegradable polymer thin films. *Applied Physics A*, 81(3):591–599, 2005.

[15] D. M. Bubb, J. S. Horwitz, J. H. Callahan, R. A. McGill, E. J. Houser, D. B. Chrisey, M. R. Papantonakis, R. F. Haglund, Jr., M. C. Galicia, and A. Vertes. Resonant infrared pulsed-laser deposition of polymer films using a free-electron laser. *Journal of Vacuum Science & Technology A*, 19(5):2698–2702, 2001.

[16] T. Lippert and J. T. Dickinson. Chemical and spectroscopic aspects of polymer ablation: Special features and novel directions. *Chemical Reviews*, 103(2):453–485, 2003.

[17] A. Vogel and V. Venugopalan. Mechanisms of pulsed laser ablation of biological tissues. *Chemical Reviews*, 103(2):577–644, 2003.

[18] R. Kelly and A. Miotello. Does normal boiling exist due to laser-pulse or ion bombardment? *Journal of Applied Physics*, 87:3177, 2000.

[19] K. P. Gritsenko and A. M. Krasovsky. Thin-film deposition of polymers by vacuum degradation. *Chemical Review*, 103:3607–3649, 2003.

[20] P.A. Pavlov and P. V. Skripov. Bubble nucleation in polymeric liquids under shock processes. *International Journal of Thermophysics*, 20(6):1779–1790, 1999.

[21] S. E. Puchinskis and P. V. Puchinskis. The attainable superheat: From simple to polymeric liquids. *International Journal of Thermophysics*, 22(6):1755–1768, 2001.

[22] I. Apitz and A. Vogel. Material ejection in nanosecond Er:YAG laser ablation of water, liver, and skin. *Applied Physics A*, 81(2):329–338, 2005.

[23] A. Vogel, B. Kersten, and I. Apitz. Material ejection in free-running Er:YAG laser ablation of water, liver, and skin. *Proc. SPIE*, 4961:40–47, 2003.

[24] M. Frenz, V. Romano, A.D. Zweig, H.P. Weber, N.I. Chapliev, and A.V. Silenok. Instabilities in laser cutting of soft media. *Journal of Applied Physics*, 66:4496, 1989.

[25] J.A. Izatt, N.D. Sankey, F Partovi, M. Fitzmaurice, R.P. Rava, I. Itzkan, and M.S. Feld. Ablation of calcified biological tissue using pulsed hydrogen-fluoride laser-radiation. *IEEE Journal of Quantum Electronics*, 26(12):2261–2270, 1990.

[26] B. Majaron, D. Šušterčič, M. Lukač, U. Skalerič, and N. Funduk. Heat diffusion and debris screening in Er: YAG laser ablation of hard biological tissues. *Applied Physics B: Lasers and Optics*, 66(4):479–487, 1998.

[27] G. Paltauf and P.E. Dyer. Photomechanical processes and effects in ablation. *Chemical Review*, 103(2):487–518, 2003.

[28] C.A. Brau. *Free-electron lasers*. Academic Press, 1990.

[29] C.A. Brau. Free-Electron Lasers. *Science*, 239(4844):1115–1121, 1988.

[30] D.A.G. Deacon, L.R. Elias, J.M.J. Madey, G.J. Ramian, H.A. Schwettman, and T.I. Smith. First Operation of a Free-Electron Laser. *Physical Review Letters*, 38(16):892–894, 1977.

[31] G. S. Edwards, D. Evertson, W. Gabella, R. Grant, T. L. King, J. Kozub, M. Mendenhall, J. Shen, R. Shores, S. Storms, and R. H. Traeger. Free-electron lasers: Reliability, performance, and beam delivery. *IEEE Journal of Selected Topics in Quantum Electronics*, 2(4):810–817, 1996.

[32] M.A. Mackanos, J.A. Kozub, D.L. Hachey, K.M. Joos, D.L. Ellis, and ED Jansen. The effect of free-electron laser pulse structure on mid-infrared soft-tissue ablation: biological effects. *Physics in Medicine and Biology*, 50(8):1885–1899, 2005.

[33] M.A. Mackanos, J.A. Kozub, and E.D. Jansen. The effect of free-electron laser pulse structure on mid-infrared soft-tissue ablation: ablation metrics. *Physics in Medicine and Biology*, 50(8):1871–1883, 2005.

[34] E.G. Gamaly, A.V. Rode, and B. Luther-Davies. Ultrafast ablation with high-pulse-rate lasers. Part I: Theoretical considerations. *Journal of Applied Physics*, 85:4213, 1999.

[35] M. R. Papantonakis and R. F. Haglund, Jr. Picosecond pulsed laser deposition at high vibrational excitation density: the case of poly(tetrafluoroethylene). *Applied Physics A*, 79(7):1687–1694, 2004.

[36] D. M. Bubb, M. R. Papantonakis, J. S. Horwitz, R. F. Haglund, Jr., B. Toftmann, R. A. McGill, and D. B. Chrisey. Vapor deposition of polystyrene thin films by intense laser vibrational excitation. *Chemical Physics Letters*, 352(3-4):135–139, 2002.

[37] S. L. Johnson, H. K. Park, and R. F. Haglund, Jr. Properties of conductive polymer films deposited by infrared laser ablation. *Applied Surface Science*, 253(15):6430–6434, 2007.

[38] S. L. Johnson, H. K. Park, and R. F. Haglund, Jr. Properties of conductive PEDOT:PSS films deposited by infrared laser ablation. *Proceedings of SPIE*, 6458, 2007.

[39] S. L. Johnson, C. T. Bowie, B. Ivanov, H. K. Park, and R. F. Haglund, Jr. Fabrication of polymer LEDs by infrared laser ablation. *Proceedings of SPIE*, 6486, 2007.

[40] C.M. Guttman, S.J. Wetzel, W.R. Blair, B.M. Fanconi, J.E. Girard, R.J. Goldschmidt, W.E. Wallace, and D.L. VanderHart. NIST-Sponsored Interlaboratory Comparison of Polystyrene Molecular Mass Distribution Obtained by Matrix-Assisted Laser Desorption/Ionization Time-of-Flight Mass Spectrometry: Statistical Analysis. *Analytical Chemistry*, 73(6):1252–1262, 2001.

[41] D. Bäuerle. *Laser Processing and Chemistry*. 2nd edition, 1996.

[42] R. Betti, VN Goncharov, RL McCrory, and CP Verdon. Growth rates of the ablative Rayleigh–Taylor instability in inertial confinement fusion. *Physics of Plasmas*, 5:1446, 1998.

[43] S.S. Harilal, C.V. Bindhu, M.S. Tillack, F. Najmabadi, and A.C. Gaeris. Internal structure and expansion dynamics of laser ablation plumes into ambient gases. *Journal of Applied Physics*, 93:2380, 2003.

[44] F.E. Karasz, H.E. Bair, and J.M. O'Reilly. Thermal Properties of Atactic and Isotactic Polystyrene. *The Journal of Physical Chemistry*, 69(8):2657–2667, 1965.

[45] P. Kamasa, P. Myśliński, and M. Pyda. Thermal expansivity of polystyrene determined by multi-frequency dilatometry. *Thermochimica Acta*, 433(1-2):93–97, 2005.

[46] D. M. Bubb, A. O. Sezer, D. Harris, F. Rezae, and S. P. Kelty. Steady-state mechanism for polymer ablation by a free-running Er:YAG laser. *Applied Surface Science*, 253(5):2386–2392, 2006.

[47] K.L. Vodopyanov. Saturation studies of H_2O and HDO near 3400 cm^{-1} using intense picosecond laser pulses. *Journal of Chemical Physics*, 94:5389, 1991.

[48] J. P. Cummings and J. T. Walsh. Erbium laser ablation - the effect of dynamic optical-properties. *Applied Physics Letters*, 62(16):1988–1990, 1993.

[49] J. Breguet and W. Luthy. Transmission of water under erbium laser irradiation. *IEEE Journal of Quantum Electronics*, 26(2):207–209, 1990.

[50] C. Branca, A. Faraone, S. Magazu, G. Maisano, P. Migliardo, and V. Villari. Polyethylene oxide: a review of experimental findings by spectroscopic techniques. *Journal of Molecular Liquids*, 87(1):21–68, 2000.

[51] V. Magnasco and M. Rossi. A simple determination of low molecular weights by infrared absorption. *Journal of Polymer Science*, 62(174), 1962.

[52] G. Taylor. The Formation of a Blast Wave by a Very Intense Explosion. I. Theoretical Discussion. *Proceedings of the Royal Society of London. Series A*, 201:159–174, 1950.

[53] M.P. Brenner and H.A. Stone. Modern classical physics through the work of G.I. Taylor. *Physics Today*, 53(5):30–35, 2000.

[54] D. A. Freiwald. Approximate blast wave theory and experimental data for shock trajectories in linear explosive-driven shock tubes. *Journal of Applied Physics*, 43(5):2224–2226, 1972.

[55] G. Langbein. Das molekulargewicht von polymeren aus ihrem ultrarotspektrum. *Colloid & Polymer Science*, 200(1), 1964.

[56] R. H. Beaumont, B. Clegg, G. Gee, J. B. M. Herbert, D. J. Marks, R. C. Roberts, and D. Sims. Heat capacities of propylene oxide and of some polymers of ethylene and propylene oxides. *Polymer*, 7(8):401–417, 1966.

[57] D.A. Willis and X. Xu. Transport Phenomena and Droplet Formation During Pulsed Laser Interaction With Thin Films. *Journal of Heat Transfer*, 122:763, 2000.

[58] X. Wen, D. E. Hare, and D. D. Dlott. Laser polymer ablation threshold lowered by nanometer hot spots. *Applied Physics Letters*, 64(2):184–186, 1994.

[59] T. Okano, editor. *Biorelated polymers and gels: controlled release and applications in biomedical engineering.* Academic Press, Boston, 1998.

[60] S. Dumitriu (Ed.). *Polymeric Biomaterials.* Marcel Dekker Inc, 2nd edition, 2002.

[61] S. L. Johnson, H. K. Park, and R. F. Haglund, Jr. Effects of laser wavelength, fluence, and pulse duration on infrared pulsed laser deposition of a conducting polymer. *Proceedings of SPIE*, 6879, 2008.

[62] A. J. Heeger. Nobel lecture: Semiconducting and metallic polymers: The fourth generation of polymeric materials. *Reviews of Modern Physics*, 73(3):681–700, 2001.

[63] G. Malliaras and R. Friend. An organic electronics primer. *Physics Today*, 58(5):53, 2005.

[64] B. L. Groenendaal, F. Jonas, D. Freitag, H. Pielartzik, and J. R. Reynolds. Poly(3,4-ethylenedioxythiophene) and its derivatives: Past, present, and future. *Advanced Materials*, 12(7):481–494, 2000.

[65] J. Simpson, S. Kirchmeyer, and K. Reuter. Advances and applications of inherently conductive polymer technologies based on poly(3, 4-ethylenedioxythiophene).

[66] M.P. de Jong, L.J. van IJzendoorn, and M.J.A. de Voigt. Stability of the interface between indium-tin-oxide and poly(3,4-ethylenedioxythiophene)/poly(styrenesulfonate) in polymer light-emitting diodes. *Applied Physics Letters*, 77(14):2255–2257, 2000.

[67] S. A. Carter, M. Angelopoulos, S. Karg, P. J. Brock, and J. C. Scott. Polymeric anodes for improved polymer light-emitting diode performance. *Applied Physics Letters*, 70(16):2067–2069, 1997.

[68] A. Berntsen, Y. Croonen, C. Liedenbaum, H. Schoo, R. J. Visser, J. Vleggaar, and P. van de Weijer. Stability of polymer LEDs. *Optical Materials*, 9(1-4):125–133, 1998.

[69] S. Kirchmeyer and K. Reuter. Scientific importance, properties and growing applications of poly(3,4-ethylenedioxythiophene). *Journal of Materials Chemistry*, 15(21):2077–2088, 2005.

[70] S. Ghosh and O. Inganas. Self-assembly of a conducting polymer nanostructure by physical crosslinking: applications to conducting blends and modified electrodes. *Synthetic Metals*, 101(1-3).

[71] X. Crispin, S. Marciniak, W. Osikowicz, G. Zotti, A. W. D. Van der Gon, F. Louwet, M. Fahlman, L. Groenendaal, F. De Schryver, and W. R. Salaneck. Conductivity, morphology, interfacial chemistry, and stability of poly(3,4-ethylene dioxythiophene)-poly(styrene sulfonate): A photoelectron spectroscopy study. *Journal of Polymer Science Part B*, 41(21):2561–2583, 2003.

[72] G. Greczynski, T. Kugler, M. Keil, W. Osikowicz, M. Fahlman, and W. R. Salaneck. Photoelectron spectroscopy of thin films of PEDOT-PSS conjugated polymer blend: a mini-review and some new results. *Journal of Electron Spectroscopy and Related Phenomena*, 121(1-3):1–17, 2001.

[73] S. Timpanaro, M. Kemerink, F.J. Touwslager, M.M. De Kok, and S. Schrader. Morphology and conductivity of PEDOT/PSS films studied by scanning–tunneling microscopy. *Chemical Physics Letters*, 394(4-6):339–343, 2004.

[74] C. D. Muller, A. Falcou, N. Reckefuss, M. Rojahn, V. Wiederhirn, P. Rudati, H. Frohne, O. Nuyken, H. Becker, and K. Meerholz. Multi-colour organic light-emitting displays by solution processing. *Nature*, 421(6925):829–833, 2003.

[75] B. J. de Gans, P. C. Duineveld, and U. S. Schubert. Inkjet printing of polymers: State of the art and future developments. *Advanced Materials*, 16(3):203–213, 2004.

[76] B. Ballarin, A. Fraleoni-Morgera, D. Frascaro, S. Marazzita, C. Piana, and L. Setti. Thermal inkjet microdeposition of PEDOT:PSS on ITO-coated glass and characterization of the obtained film. *Synthetic Metals*, 146(2):201–205, 2004.

[77] G. M. Hale and M. R. Querry. Optical constants of water in the 200 nm to 200 μm wavelength region. *Applied Optics*, (12):555–563, 1973.

[78] V. M. Zolotarev, B. A. Mikhilov, L. L. Alperovich, and S. I. Popov. Dispersion and absorption of liquid water in the infrared and radio regions of the spectrum. *Optics and Spectroscopy*, (27):430–432, 1969.

[79] F. Louwet, L. Groenendaal, J. Dhaen, J. Manca, J. Van Luppen, E. Verdonck, and L. Leenders. PEDOT/PSS: synthesis, characterization, properties and applications. *Synthetic Metals*, 135(1-3):115–117, 2003.

[80] L.J. van der Pauw. A method of measuring specific resistivity and hall effect of disks or arbitrary shapes. *Journal of Chemical Physics*, 94(8):5389–5393, 1991.

[81] S. K. M. Jonsson, J. Birgerson, X. Crispin, G. Greczynski, W. Osikowicz, A. W. D. van der Gon, W. R. Salaneck, and M. Fahlman. The effects of solvents on the morphology and sheet resistance in poly (3,4-ethylenedioxythiophene)-polystyrenesulfonic acid (PEDOT-PSS) films. *Synthetic Metals*, 139(1):1–10, 2003.

[82] V. F. Petrenko and R. W. Whitworth. *Physics of Ice*. Oxford University Press, 1999.

[83] E. Leveugle, A. Sellinger, J.M. Fitz-Gerald, and L.V. Zhigilei. Making Molecular Balloons in Laser-Induced Explosive Boiling of Polymer Solutions. *Physical Review Letters*, 98(21):216101, 2007.

[84] E. Leveugle and L.V. Zhigilei. Molecular dynamics simulation study of the ejection and transport of polymer molecules in matrix-assisted pulsed laser evaporation. *Journal of Applied Physics*, 102(7):74914, 2007.

[85] Z. Chen, A. Bogaerts, and A. Vertes. Phase explosion in atmospheric pressure infrared laser ablation from water-rich targets. *Applied Physics Letters*, 89:041503, 2006.

[86] N. L. Dygert, K. E. Schriver, and R. F. Haglund, Jr. Resonant infrared pulsed laser deposition of a polyimide precursor. *Journal of Physics: Conference Series*, 59:651–656, 2007.

[87] B. Toftmann, M. R. Papantonakis, R. C. Y. Auyeung, W. Kim, S. M. O'Malley, D. M. Bubb, J. S. Horwitz, J. Schou, P. M. Johansen, and R. F. Haglund, Jr. UV and RIR matrix assisted pulsed laser deposition of organic MEH-PPV films. *Thin Solid Films*, 453-54:177–181, 2004.

[88] Jr. Haglund, S.L. Johnson, and H.K. Park. Electronic and optical properties of polymer thin films deposited by resonant infrared laser ablation. *Journal of Laser Micro/Nanoengineering*, 2:234–240.

[89] S. L. Johnson, H. K. Park, and R. F. Haglund, Jr. Fabrication of multi-layered polymer leds by resonant infrared pulsed-laser deposition. *Proceedings of SPIE*, 6655, 2008.

[90] C.W. Tang and S.A. VanSlyke. Organic electroluminescent diodes. *Applied Physics Letters*, 51:913, 1987.

[91] J. H. Burroughes, D. D. C. Bradley, A. R. Brown, R. N. Marks, K. Mackay, R. H. Friend, P. L. Burns, and A. B. Holmes. Light-emitting-diodes based on conjugated polymers. *Nature*, 347(6293):539–541, 1990.

[92] R. H. Friend, R. W. Gymer, A. B. Holmes, J. H. Burroughes, R. N. Marks, C. Taliani, D. D. C. Bradley, D. A. Dos Santos, J. L. Bredas, M. Logdlund, and W. R. Salaneck. Electroluminescence in conjugated polymers. *Nature*, 397(6715):121–128, 1999.

[93] Y. Wu, C.H.M. Marée, R.F. Haglund, Jr, J.D. Hamilton, M.A.M. Paliza, M.B. Huang, L.C. Feldman, and R.A. Weller. Resistivity and oxygen content of indium tin oxide films deposited at room temperature by pulsed-laser ablation. *Journal of Applied Physics*, 86:991, 1999.

[94] M.A. Morales-Paliza, M.B. Huang, and L.C. Feldman. Nitrogen as background gas in pulsed-laser deposition growth of indium tin oxide films at room temperature. *Thin Solid Films*, 429(1-2):220–224, 2003.

[95] Y. Park, V. Choong, Y. Gao, B.R. Hsieh, and C.W. Tang. Work function of indium tin oxide transparent conductor measured by photoelectron spectroscopy. *Applied Physics Letters*, 68:2699, 1996.

[96] G. D. Scholes and G. Rumbles. Excitons in nanoscale systems. *Nature Materials*, 5(9):683–696, 2006.

[97] Y. Shi, J. Liu, and Y. Yang. Device performance and polymer morphology in polymer light emitting diodes: The control of thin film morphology and device quantum efficiency. *Journal of Applied Physics*, 87:4254, 2000.

[98] J. Liu, Y. Shi, L. Ma, and Y. Yang. Device performance and polymer morphology in polymer light emitting diodes: The control of device electrical properties and metal/polymer contact. *Journal of Applied Physics*, 88:605, 2000.

[99] I. D. Parker. Carrier tunneling and device characteristics in polymer light-emitting diodes. *Journal of Applied Physics*, 75(3):1656–1666, 1994.

[100] D. M. Bubb, S. L. Johnson, R. Belmont, K. E. Schriver, R. F. Haglund, Jr., C. Antonacci, and L. S. Yeung. Mode-specific effects in resonant infrared ablation and deposition of polystyrene. *Applied Physics A*, 83(1):147–151, 2006.

[101] K. Rodrigo, P. Czuba, B. Toftmann, J. Schou, and R. Pedrys. Surface morphology of polyethylene glycol films produced by matrix-assisted pulsed laser evaporation (MAPLE): Dependence on substrate temperature. *Applied Surface Science*, 252(13):4824–4828, 2006.

[102] MR Silverstein and XF Webster. *Spectrometric identification of organic compounds, 6th edition*. 1998.